METAL-ORGANIC FRAMEWORK NANOPROBES: NEW APPROACHES TO CHEMICAL SENSING AND PHOTOTHERAPY OF ALZHEIMER'S DISEASE

JIUHAI WANG

PhD

The Hong Kong Polytechnic University

2020

THE HONG KONG POLYTECHNIC UNIVERSITY

DEPARTMENT OF BIOMEDICAL ENGINEERING

METAL-ORGANIC FRAMEWORK NANOPROBES: NEW APPROACHES TO CHEMICAL SENSING AND PHOTOTHERAPY OF ALZHEIMER'S DISEASE

Jiuhai Wang

A thesis submitted in partial fulfillment of the requirements for the degree of Doctor of Philosophy

December 2019

Certificate of Originality

I hereby declare that this thesis is my own work and that, to the best of my knowledge and belief, it reproduces no material previously published or written, nor material that has been accepted for the award of any other degree or diploma, except where due acknowledgement has been made in the text.

_____ (Signed)

WANG Jiuhai (Name of Student)

Abstract

Metal−organic framework (MOF) is a class of hybrid materials synthesized from metal cluster nodes and organic linkers that connect these nodes. This rapidly expanding class of structures presents advantages in various applications such as gas storage and separation, catalysis, sensing, cancer theranostics, and others. However, the applications of MOFs have not been extended in the fields including chemo-sensing and phototherapy of neurodegenerative diseases.

The first part of this thesis is about Fe^{3+} colorimetric sensing based on Zn-MOF-74 nanodots. Zn-MOF-74 nanodots were successfully synthesized through a mild chemical reaction under room temperature and used as a chemo-sensor for highly sensitive and selective detection of Fe^{3+} in aqueous solution *via* a colorimetric approach. Conventional MOF-based chemo-sensors can act as a host and antenna to provide a rigid scaffold that protects fluorescent molecules inside the framework from self-quenching and also sensitize them to form tunable fluorescence. This often requires sophisticated apparatus and longer time. Our colorimetric approach is more convenient to observe the visual color change of the solution by naked eyes.

The multiple functionalities of MOFs can also be used as nanomedicines not only for the phototherapy of tumors but also for neurological disorders such as Alzheimer's disease (AD). The second part of this thesis is regarding the photodynamic inhibition of Alzheimer's amyloid-β (Aβ) using porphyrin MOF PCN-224 nanoparticles. Porphyrin MOF PCN-224 nanoparticle of sub-100 nm size was synthesized and used to photo-catalyze the oxygen into $^1O_2$ which can attenuate the neurotoxicity of Aβ by oxidizing the Aβ monomer and preventing it from aggregating into high-order oligomers and fibrils in the early stage. The porphyrin-based MOF showed strong light-to-oxygen generation capability due to the high percentage of

exposed TCPP ligands in the framework and easy diffusion of molecular oxygen through the porous structure. The Aβ oxidized by photo-activated PCN-224 has low neurotoxicity when co-incubated with PC12 cells.

In the third part of this thesis, A hybrid nanosystem composed of PCN-222 nanosheet and Indocyanine green – PCN-222@ICG was developed to realize the combinational phototherapy of AD. PCN-222 nanosheet inhibited the Aβ aggregation through the oxidization of the peptide by producing $^1O_2$, whereas ICG prevent the Aβ aggregation by photothermal effect. Because of the high surface area of ultrathin PCN-222 nanosheet, the loading capacity of ICG on the PCN-222 was very high, thus the low concentration of nanoprobes exhibited a high inhibitory effect against Aβ aggregation. A BBB Transwell model consisted of hCMEC cells and human primary astrocytes and pericytes was built to examine the BBB permeability of this nanoprobe.

Finally, with the newly emerging organ-on-a-chip technology, a brain-on-a-chip model was successfully built up through soft lithography. Human umbilical vein endothelial cells (HUVEC), human primary astrocytes, and pericytes were co-cultured in the chips that recapitulated human-relevant physiological BBB properties. Nanoprobes including MOF PCN-222@ICG and carbon dots modified with rabies virus glycoprotein (RVG) peptide had improved BBB permeability when assessed on the brain-on-a-chip model. Overall, this thesis described three MOF nanoprobes for chemo-sensing and AD phototherapy and reported a brain-on-a-chip platform for the assessment of BBB permeability for the PCN-222@ICG and carbon dots nanoprobes.

Acknowledgement

I would like to express my sincere gratitude to my supervisor Prof. Mo Yang for providing me the opportunity to work in his lab and for taking the effort to guide me throughout my graduate study. The work I have done will not be where it is now without his guidance and vision. His support and guidance throughout my graduate study is immeasurably valuable.

I would also like to extend my gratitude to the member of Prof. Yang's laboratory for their continuous supports. They have made the entire experience much more enjoyable. Dr. Cheng Changming, Dr. Jiang Ding, Dr. Shi Jingyu, Dr. Lyu Jing, Mr. Tian Feng, Ms. Oudeng Gerile, Ms. Fan Yadi, and Ms. Zhang Ruolin have provided invaluable advices which made my work progress smoother. I would also like to thank our collaborator Dr. Nur Mustafaoglu at Harvard University for her help and advice on the establishment of BBB chip.

This work is funded by Research Grant Council of Hong Kong (Grant number: 15210818), Hong Kong Research Grants Council General Research Fund (Grant number: PolyU 15216917), and National Natural Science Foundation of China (Grant number: 81471747).

Publications

Peer-reviewed Articles

J. Wang, M. Yang, et al. Porphyrin Metal-organic Framework PCN-224 for Near-IR Induced Attenuation of Aggregation and Neurotoxicity of Alzheimer's Amyloid-β Peptide. *ACS Applied Materials & Interfaces*. 2018, 10, 43, 36615.

J. Wang, Y. Fan, M. Yang, et al. Ultrasmall metal-organic framework Zn-MOF-74 nanodots: size-controlled synthesis and application for highly selective colorimetric sensing of iron (III) in aqueous solution. *ACS Applied Nano Materials*. 2018. 1, 3747

Invited Book Chapter

J. Wang, M. Yang. Functionalized nanomaterials for photothermal therapy. *Theranostic Bionanomaterials*, Elsevier. 1st Edition, May 2019

Conference Proceedings

J. Wang, M. Yang. Porphyrin Metal-organic Framework: A New Approach to Phototherapy of Alzheimer's Disease. 2018 IEEE International Conference on Nano/Molecular Medicine and Engineering, Hawaii, U.S.A.

J. Wang, D. Jiang, M. Yang. Oxygen Vacancy Engineered Tungsten Oxide Hydrate Nanosheets Coupling with Nitrogen Doped Graphene Quantum Dots for Ultrasensitive Photoelectrochemical Detection of *E. Coli*. Transducers 2019 - EUROSENSORS XXXIII Conference, Berlin, Germany.

J. Wang, M. Yang. Blood-Brain Barrier Chip Recapitulates Human Alzheimer's Brain for Drug Testing. DOCTORAL FORUM OF CHINA - Biomedical Engineering Doctoral Innovation Forum. Hangzhou, China, 2019.

List of Figures

List of Abbreviations

5-FU	5-Fluorouracil
ALD	Atomic layer deposition
AZT-TP	Azidothymidine triphosphate
Aβ	Amyloid-β
BBB	Blood-brain barrier
BP	Black phosphorus
CD	Circular Dichroism
CDV	Cidofovir
CL	Chemiluminescence
CNS	Central nervous system
CRET	Cerenkov resonance energy transfer
CT	X-ray computed tomography
DA	Dopamine
DCFH-DA	2’,7’-dichlorodihydrofluorescein diacetate
DOX	Doxorubicin
DPBF	Diphenylisobenzofuran
ECM	Extracellular matrix
ESR	Electron spin resonance
FRET	Fluorescence resonance energy transfer
GO	Graphene oxide
HFIP	Hexafluoro-2-propanol
HUVEC	Human primary umbilical vein endothelial cell
ICG	Indocyanine green
ICG-MS	Inductively coupled plasma mass spectrometry
ICP-OES	Inductively coupled plasma-optical emission spectroscopy

MOF	Metal–organic frameworks
MoS_2	Molybdenum disulfide
MRI	Magnetic resonance imaging
NIR	Near-infrared
NVU	Neurovascular unit
PCP	Porous coordination polymers
PDT	Photodynamic therapy
PET	Polyethylene terephthalate
PL	Photoluminescent
PS	Photosensitizer
PTT	Photothermal therapy
PVA	Polyvinyl alcohol
QDs	Quantum dots
RhB	Rhodamine B
ROS	Reactive oxygen species
RVG	Rabies virus glycoprotein
TCH	*4-tert*-butylcyclohexanone
TCPP	Tetrakis(4-carboxyphenyl)-porphyrin
TGA	Thermogravimetric analysis
ThT	Thioflavin T
UCNP	Upconversion nanoparticles
WS_2	Tungsten disulfide

Table of Contents

1 Introduction

1.1 Metal-organic Framework

1.1.1 General Background

Metal-organic frameworks (MOFs), also known as porous coordination polymers (PCPs) or coordination networks are an extensive class of inorganic and organic hybrid materials that consist of metal clusters and organic linkers with numerous types of structural motifs due to multitudinous possible combinations of metal and bridging ligands[1-2]. With the growing library of organic ligands and large number of experimentally synthesized MOF structures, researchers now have been close to computationally predict the potential affinity of one guest ligand to a host metal "node" to form a framework structure with high accuracy. MOFs are fundamentally important and technically relevant and have been extensively studied because of their rich structural chemistry, intrinsic ultrahigh porosity, enormous and adjustable internal surface areas, tunable pore size, and other unique optical and catalytical properties. These unique physiochemical properties make MOF a crucially important compound in many applications including gas storage and purification, catalysis, template for materials synthesis, drug delivery, *etc*. In recent years, emerging applications in thin films and membranes, electronic devices, chemical/biological sensing, biomedical imaging are attracting more and more research interests among scientists. The above functions and properties can derive from either metal components (*e.g.* catalysis), organic ligands (*e.g.* biomedical imaging) or both. Thus, the combination of such diverse metals and organic ligands may create infinite opportunities for new applications.

Since the group of O. M. Yaghi published the structure of MOF-5 in *Nature* in 1999[3], the development of MOFs has experienced a tremendous leap in the past two

decades with hundreds of different new MOF structures have been identified and synthesized. Interestingly, unlike other conventional solid matter like zeolites, carbons and oxides, a great number of MOF compounds are known to exhibit high level of structural flexibility and shrinkage/expansion through the control of the architecture and the selection of nodes.[4]. These properties such as drastically increased velocity of molecular traffic through these open structures are, to a large extent, attributed to the regularity of pores in nanometer size. With such unbelievable levels of porosity, high surface area, tunable pore size and numerous chemical inorganic-organic compositions, MOFs have attracted attention of enormous numbers of researchers in both academia and industry in recent years with the number of publications on "metal-organic frameworks" and "coordination polymers" over 1200 per annum[4].

Scientists have been realizing that organic ligands need not be only inert structural elements but could yield tremendous benefits if their functional and reactive nature were to be exploited. Although the functions of small organic molecules are easy to investigate, it is challenging to translate these properties to solid state materials as they have unpredictable structures of molecular crystals. MOF structures are more advantageous in this respect because they are covalently connected by individual ligands with predictable positions. Moreover, the components of MOFs are not close-packed. Instead, ligands are spatially separated by metal clusters, thus they are more likely to retain the properties of uncoordinated monomers[5].

1.1.2 Chemical and Structural Diversity

The term metal-organic framework or coordination polymers can be defined as extended arrays composed of isolated metal atoms or clusters that are linked by polyfunctional organic ligands, based on M–L–M connectivity. Metal-organic frameworks consist of a wide range of metals and a diverse range of organic ligands,

forming a network in numerous ways. Transition metals including zinc are the most commonly used metals for construct MOFs. However, there are growing number of publications report rare-earth based MOF structures due to their unique optical properties. More recently, driven by the search for lightweight materials and hydrogen storage, a great amount of efforts has been made in studying p-block elements, especially Aluminum-, Gallium-, Tin-, and Magnesium-based MOFs.

The study of organic ligands focuses on connectivity through oxygen atoms of carboxylic acid groups. Therefore, the vast majority of known materials in this area are based upon oxygen bridges. Dicarboxylic acids such as oxalic acid and benzene-1,4-dicarboxylic acid, as have flexible aliphatic system, have been extensively employed to make MOF structures. Monocarboxylic acids including formic and acetic acids are also good candidates for constructing hybrid frameworks, especially two-dimensional ultrathin MOFs[6]. In addition to forming M–O linkages, there are also other types of connection, *e.g.* M–Cl, M–N, M–S or even with inorganic groups such as phosphate to be explored in more diverse and complex structures[7]. The hybrid structures are strongly influenced by the coordination preferences of metals with organic ligands. The coordination framework structures can be constructed in different dimensionalities – 1-, 2-, or 3-D, depending on the preference of connection between metals and ligands as well as the presence of auxiliary or guest molecules in the building units. Figure 1.1 shows the examples of 0-D, 1-D, 2-D, and 3-D structures of Tin MOFs.

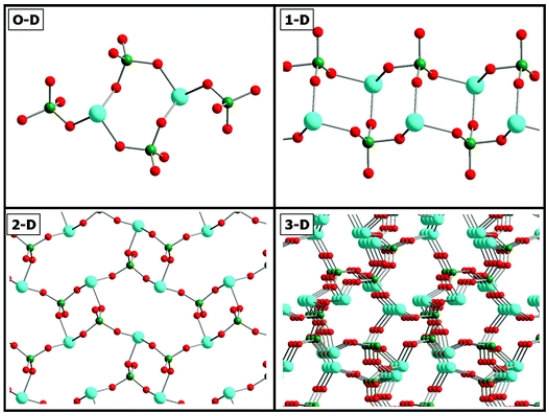

Figure 1.1 Examples of 0-D, 1-D, 2-D, and 3-D structures of Sn2P2O4 MOFs. Blue spheres denote tin, green phosphorus, and red oxygen. Adapted from Ref [7].

1.1.3 Synthesis of Metal-organic Framework

Conventional synthesis of MOFs is *via* one-pot self-assembly reaction between organic molecules and inorganic ions. MOFs can be synthesized under a wide range of temperatures from room temperature to over 250 °C in a variety of solutions including water or organic solvents such as *N*,*N*-dimethylformamide (DMF) or ethanol. To obtain single MOF crystalline, low temperature is usually adopted to provide a relatively slow evaporation and diffusion of organic solvents of a reaction solution. This process usually takes long reaction time ranging from days to weeks. Higher temperature and pressure can induce more complicated and diverse products with better single crystalline as compared to the products synthesized under lower temperature[8]. The vast majority of reported MOF structures are synthesized by solvothermal approaches which significantly reduce reaction time but require bulky heating equipment and high energy supply. MOFs synthesized by conventional approaches are thermally unstable and more likely to react with the solvent used in the reaction system.

Microwave synthetic approaches has been employed in organic chemistry for several decades, but only been applied to the preparation of MOFs since a few years ago. Microwaves are usually generated by a generator called magnetron which can convert high-voltage direct current into high frequency radiation. Microwave heating

is almost instantaneous, allowing the reaction temperatures to rise above the boiling point of a solvent in pressurized vessels within several minutes[9]. This synthetic method takes much shorter time and usually produces MOFs with high mono-dispersity. A Sonnauer et al. reported a high-throughput approach which allowed fast investigation of a large part of the parameter space for the isolation of lanthanide coordination polymers. They also reached to a conclusion that stirring the mixture during the reaction could result in lower yields of product but can be improved by increasing reaction time[10]. Since power of irradiation and other instrumental parameters of microwave are crucial to the microwave-assisted synthesis, J. S. Choi et al. discussed the influence of the power level, irradiation time, temperature, solvent concentration and substrate composition on the crystallinity and morphology of MOF-5[11]. They claimed that 15 minutes of reaction time is enough to obtain MOF-5 products, while 30 mins for high quality crystals. However, over 30 mins of microwave heating could result in crystal degradation and surface defects.

There are also other synthesis methods for MOF synthesis including spray-drying, microfluidic synthesis, microemulsion synthesis, electrospinning synthesis, *etc*. Spray-drying is a versatile methodology to assemble MOFs *via* aerosol casting. MOFs produced by this method showed a highly crystalline appearance with desired shapes and architectures[12]. Microemulsion approach is suitable for particle synthesis because it allows control over shape, size, and polydispersity of the MOFs products[13]. M. Faustini and co-workers reported a continuous and ultrafast synthesis of MOF crystals and MOF heterostructures based on a microfluidic strategy. This method allows continuous fabrication of high-quality MOF crystals and composites, which exhibits distinct morphological characteristics in a time-efficient manner and represents a viable alternative to the time-consuming and multi-step MOFs synthesis processes[14]. M.

Bechelany and co-workers were able to grow highly crystalline MOF materials (ZIF-8 & MIL-53-NH_2) on a mat of electrospun nanofibers, allowing the production of MOFs with controlled sizes, morphology, orientation and high accessibility[15].

1.2 Metal-organic Framework in Chemical and Electronical Applications

The past decade has seen explosive growth in the synthesis, characterization, and investigation of various MOFs. Due to the enormous chemical and structural diversity as well as novel physiochemical properties of these materials, great among of efforts have been focused on their applications, among which the earliest and most extensive applications were in chemistry and chemical technology. The exceptional porosity of MOFs provides possibilities for a wide range of potential uses including gas storage, separations, and catalysis. In particular, applications in energy technologies such as fuel cells, supercapacitors, and catalytic conversions have made them objects of extensive study, industrial-scale production, and others. In addition, MOFs are excellent candidates for detecting the chemicals because they provide large number of reactive sites for reaction with targets molecules. More recent applications of MOFs include fabrication of light-emitting devices due to the discovery of lanthanide MOFs with exciting optical properties. Those chemical applications will be discussed in detail in the following context.

1.2.1 Chemical Sensors

Among numerous MOF applications, MOF-based chemical sensor has been regarded as a promising one because MOFs can exhibit different degrees of luminescent enhancement or quenching effect in response to interactions between inserted guest molecules and the construction units of framework itself, which are beneficial for detecting the targets of interest. Special features of MOFs include: 1) high surface areas would absorb analytes in a high capacity, which enhances detective sensitivity; 2)

specific functional sites (open metal sites, Lewis acidic/basic sites, and tunable pore sizes) that can specifically recognize the targeting molecules, realizing unprecedented high selectivity and sensitivity through host-guest interactions or size exclusion; and 3) flexible porosity or and structure enables the reversible uptake and release of substrates to increase regeneration and recycling.

1.2.1.1 Ion sensing

Chemosensors targeting heavy and transition metal cations are very important and technically relevant due to the environmental and biological relevance of such metal ions. MOFs can act as a host and antenna to provide a rigid scaffold that can protect fluorescent molecules inside the frameworks from solvent quenching and also sensitize them to form tunable fluorescence. In addition to fluorescence-based sensing, colorimetric signaling is another preferable approach of detecting ions, as it is more convenient to observe the visual color change of the solution by naked eyes. Organic ligands, particularly the fluorescent ligands whose optical properties are sensitive to the surrounding media are ideal for the ion sensing purpose.

Based on the above facts and demands, many MOFs are designed and harnessed as ion sensors. H. Zhang and co-workers synthesized two lanthanide MOFs Eu(FBPT)(H_2O)(DMF) and Tb(FBPT)(H_2O)(DMF) (FBPT = 2′-fluoro-biphenyl-3,4′,5-tricarboxylate by means of solvothermal methods using fluorinated tricarboxylic acid as an organic ligand[16]. These two MOFs can be used as a chemosensor as they show a remarkable quenching effect in the luminescence emission of lanthanides upon the introduction of the small organic molecules for small organic molecules (*e.g.* (acetone, 1-phenylethanone and benzaldehyde) and metal ion (Cu^{2+})). They proposed that the mechanism of this quenching effect was due to the interaction between the Cu^{2+}

ions and the fluorine, carboxylate and/or terminal water Lewis basic sites on the Eu-MOF. The interaction between the Cu^{2+} ions and the FBPT ligands inhibit the energy transfer efficiency from FBPT to the Eu^{3+} ions within the MOF structure, result in a decreased luminescent intensity. Another nanoscale MOF structure MIL-53-COOH (Al) encapsulating Eu^{3+} in the pores was fabricated by B. Yan and co-workers[17]. The Eu^{3+} incorporated MOF shows excellent luminescence and good fluorescence stability in aqueous solution. However, its luminescence was quenched when in contact with Fe^{3+} ion. It was found that other metal cations such as K^{+}, Na^{+} , Ag^{+}, Ca^{2+}, Mg^{2+}, Cu^{2+}, Zn^{2+}, Co^{2+}, Ni^{2+}, Hg^{2+}, Cd^{2+}, Pb^{2+}, Fe^{2+}, and Cr^{3+} cannot significantly influence the luminescence intensity of Eu^{3+}– incorporated MOFs. The sensing mechanism can be attributed to the cation exchange behavior between the framework element Al^{3+} in the MOF and Fe^{3+} ion, causing effective suppression of the energy transfer from the ligand to Eu^{3+}, thus quenching the luminescence of MOF. The limit of detection (LOD) of this Eu-MOF for Fe^{3+} ion sensing can reach 0.5 µM with a broad linear range (0.5 – 500 µM). D. Sun and co-workers proposed a luminescent MOF based on Eu^{3+} and H_4BTMIPA ligand (H_4BTMIPA = 5,50-methylenebis-(2,4,6-trimethylisophthalic acid))[18]. The $[H_2N(CH_3)_2]^{+}$ ions as counterions are located in the channels, which can be cation exchanged by Al^{3+} and Fe^{3+}, resulting in fluorescence enhancement and quenching, respectively (Figure 1.2).

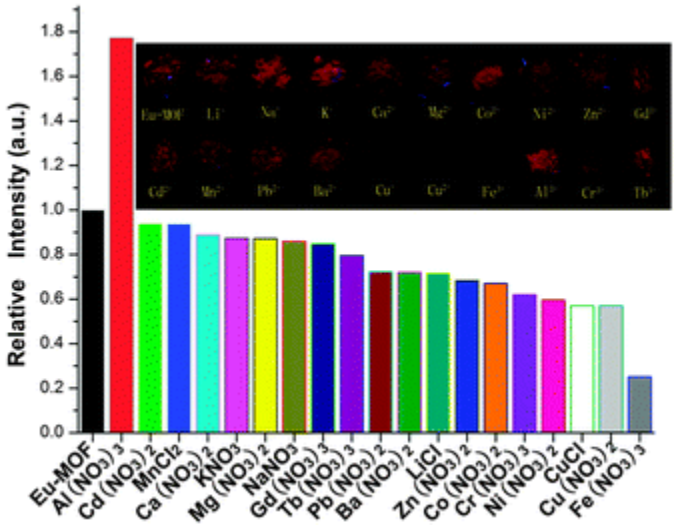

Figure 1.2 Photoluminescence intensity of the 5D0 → 7F2 transition (617 nm) of MOF treated with different metal ions (10^{-3} M) in DMF solution for 72 hours. Inset: the colors of the treated samples with different metal ions under the irradiation of UV light of 365 nm. Adapted from Ref18.

1.2.1.2 Sensing of organic compounds and small molecules

M. Dincă and co-workers reported two MOFs – Zn_2(TCPE) (TCPE = tetrakis(4-carboxyphenyl)ethylene) function as sensor for ammonia at 100 °C. The fluorescence spectrum of Zn_2(TCPE) MOF experiences red shift at different levels in the presence of a series of analytes including NH_3, Et_3N, ethylenediamine, N_2, *N*,*N*-diethylformamide (DEF), and H_2O at room temperature. Interestingly, at higher temperature 100 °C, the Zn_2(TCPE) selectively show red shift only in the presence of ammonia in the fluorescence spectrum, with all other analytes silenced[19]. Another needle-shaped crystals of $[Eu_2L_3(H_2O)_4]\cdot 3$ DMF (L=2′,5′-bis(methoxymethyl)-[1,1′:4′,1″-terphenyl]-4,4″-dicarboxylate)) was synthesized by D. Song and co-workers[20]. Its fluorescence can be “turned on” in the presence of DMF vapor. This sensor is of great importance since DMF is evidenced by many studies that it causes liver damage and skin problem in human body (Figure 1.3).

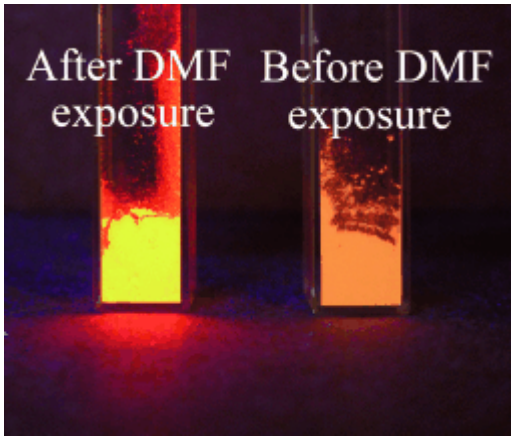

Figure 1.3 $[Eu_2L_3(H_2O)_4]$ MOF before and after exposure of DMF vapor. Adapted from Ref.[20].

1.2.2 Light-emitting Devices

MOFs, particularly lanthanide MOFs are excellent candidates and have shown tremendous promise for optoelectronic device fabrication due to their structural diversity and unique optical properties. So far, a variety of luminescent MOFs with tunable fluorescent emission has been designed for Light-emitting devices (LED) including lighting and displays. One limitation is that emission from organic or inorganic luminescent materials cannot cover the entire visible region of the solar spectrum. To overcome this problem, various architectures of devices combining monochromatic emission from different compounds have been suggested. White-light emitting devices may be obtained by tuning the emission color and controlling the precise control of the relative amount of different Ln^{3+} ions in a single host framework.

H. Zhang and co-workers reported a strategy for reducing the size of lanthanide MOF Eu_{1-x} Tb_x -MOF crystals to diameters of around 100 nm by introducing capping reagents with the same chemical functionality as the linkers[21]. The photoluminescent (PL) spectra of Eu_{1-x} Tb_x -MOF peaked at 540 nm which corresponds to the $^5D_4 \rightarrow {}^7F_5$ transition of the Tb^{3+} ions in the green region. Two other main peaks at around 589 nm and 615 nm are assigned to the $^5D_0 \rightarrow {}^7F_1$ and $^5D_0 \rightarrow {}^7F_2$ transitions of the Eu^{3+} ions, respectively. The intensity of the peak at 540 nm changes with Tb^{3+} /Eu^{3+} ratio,

suggesting the existence of Tb^{3+} /Eu^{3+} energy transfer and the typical emission peaks of Tb^{3+} disappear completely at Tb^{3+} /Eu^{3+} = 1.

S. Júnior and co-workers reported polymeric Lanthanide MOF nanofibers by using electrospinning methods and present a detailed study on the spectroscopic properties[22]. Polyvinyl alcohol (PVA) incorporated Ln-MOFs ([Ln(DPA)(HDPA)], where H2DPA is pyridine 2,6-dicarboxylic acid and Ln = Tb^{3+} and Eu^{3+} ions designated as Eu-MOF@PVA and Tb-MOF@PVA, respectively. They found that the emission spectrum of Eu-MOF@PVA presents typical narrow bands of the Eu^{3+} 5D0 → 7FJ transitions centered in a non-centrosymmetric site. The 5D4 → 7F5 transition centered at ca. 543 nm is the strongest in the emission spectrum of Tb-MOF@PVA, corresponding to ca. 52% of the integrated emission spectrum. The colors emitted by $Tb_{0.95}Eu_{0.05}$MOF@PVA, $Tb_{0.8}Eu_{0.2}$MOF@PVA and $Tb_{0.5}Eu_{0.5}$MOF@PVA are in the green – yellow (0.4083, 0.4803), yellow (0.4364, 0.4616) and orange (0.5042, 0.4212) portions of the chromaticity chart, respectively.

1.2.3 Gas Separation, Purification and Storage

Adsorptive gas separation is very important in industry. Research interests regarding gas adsorption keep growing unprecedentedly fast over the last few decades. With fast development of synthesis of new sorbent materials with high porosity and surface area, adsorptive separation become an increasingly more important application for these porous materials in energy and environmental technologies. As a result, a great deal of research efforts has been put in the synthesis of MOFs with the largest possible surface areas in order to obtain exceptionally high gas storage abilities. MOFs have been employed in various gas adsorption applications such as H_2 and CH_4 purifications, CO_2 capture, industrial gas drying, CO removal, desulfurization of transportation fuels, and other separations for meeting the higher environmental standards. In gas separation

processes, the gas mixtures usually consist of components having concentrations in the same order of magnitude. Recently, the separation of Kr–Xe by pressure swing adsorption, as well as the purification of methane in natural gas were piloted on MOF-adsorbents.

J. R. Long and co-workers synthesized a magnesium- incorporated porous MOF solid structure − $Mg_3(NDC)_3(DEF)_4$ (NDC = 2,6-naphthalenedicarboxylate) consists of linear Mg_3 units linked via NDC bridges to form a three-dimensional framework, featuring one-dimensional channels filled with DEF molecules (Figure 1.4). The results of hydrogen storage characteristics of $Mg_3(NDC)_3$ obtained from volumetric gas sorption apparatus shows the H_2 adsorption isothermal at 77 K of just 2.3 mmol g^{-1} (1.7 mol mol^{-1}, 0.46 wt %) at 880 Torr, a rather low storage capacity compared to other reported MOF solids[23]. However, the $Mg_3(NDC)_3$ has a remarkable O_2 adsorption capacity, showing an estimated BET surface area of 190 m^2 g^{-1}. This selective gas adsorption property demonstrates the capability of $Mg_3(NDC)_3$ solids for sustainable O_2 storage.

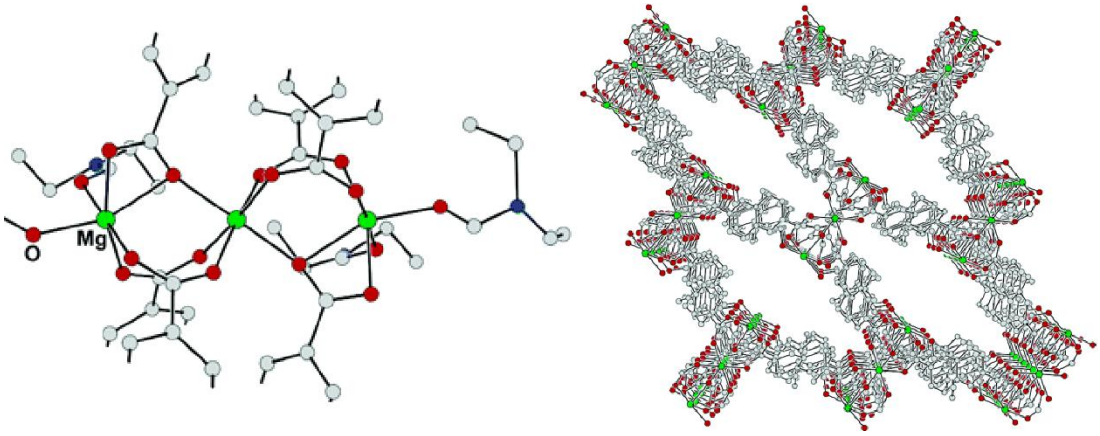

Figure 1.4 Portions of the crystal structure of − $Mg_3(NDC)_3(DEF)_4$ and showing the linear Mg_3 unit (left) and, upon removing the DEF molecules, the arrangement of channels along the (101) direction (right). Hydrogen atoms are omitted for clarity. Adapted from Ref.[23].

CO_2 separation is another important application since the growing awareness of global warming in recent years. As the CO_2 is physically adsorbed in MOFs in the low

temperature region and the lower energy of adsorption for the physisorption process, MOF adsorbents such as MIL-53 (Cr) show sufficient adsorption capability only under a higher CO_2 partial pressure. Studies also show that the hydrated form of MIL-53 (Cr) has a better selectively binding and adsorption of CO_2 over methane[24]. However, in general, MOFs solids still do not perform as well as an amine scrubber even under these high-pressure conditions. S. Deng and co-workers demonstrated a series of newly discovered MOF adsorbents including MOF-5, MO-177 that being used for CO_2, CH_4, N_2O, and N_2 adsorption[25]. Zeolite 5A as a traditional industrial-use adsorbent was used to assess the MOF adsorbents' efficacy for CO_2, CH_4, and N_2O removal from air and separation of CO_2 from CH_4. The results of selectivity and adsorbent selection investigation indicated that zeolite 5A perform better in the CO_2 and N_2O removal from air and separation of CO_2 from CH_4, while MOF-177 is a better adsorbent for removing CH_4 from air. Both MOFs were found with larger adsorption capacities for CO_2 and CH_4 than zeolite 5A at higher pressures, which suggested that MOF structures are better adsorbents for CO_2 and CH_4 storage.

1.2.4 Catalysis

Heterogeneous catalysis was one of the earliest proposed and demonstrated applications for crystalline MOF materials, which has a crucial impact on global economy. The global catalyst market is estimated to be between 15 – 20 billion USD annually. Zeolites, as pure inorganic materials, are among the most commercially important and widely used catalysts in industry[26]. Unavoidably, MOFs used as catalysts have to be compared with zeolites. Although MOFs share some of the catalytically relevant features of zeolites (large internal surface areas and uniform pore and cavity sizes), they also differ in many ways. As MOF structures are consist of organic ligands, they can be synthesized through more various approaches than zeolites[27]. MOF catalysts are not

likely to be competitive with zeolites in certain conditions such as high temperatures due to the lower thermal stability. Moreover, while many MOFs exhibit zeolite-like permanent microporosity, others collapse when solvent is removed. The persistence of microporosity after solvent evacuation is essential for gas-phase catalysis, as well as for applications such as gas separations and gas storage.

Zirconium MOFs (Zr-MOFs) bring attention among researchers due to the rich structure types, outstanding stability, intriguing properties and catalytical potentials. UiO-66 is one member of Zr-MOF family. De Vos and co-workers reported that the catalytic activity of the zirconium terephthalate UiO-66 (Zr) can be drastically increased by using specific modulators trifluoroacetic acid (TFA) and HCl in the synthesis[28]. Meerwein reduction of *4-tert*-butylcyclohexanone (TCH) with isopropanol (IPA) was performed to assess the catalytical activity of UiO-66. The results indicated that the non-modulated UiO-66 shows almost no catalytical activities, whereas the UiO-66 with TFA modulators in the synthesis exhibited high catalytical activities with around 93% conversion of *tert*-butylcyclohexanone been achieved. J. Hupp and co-workers introduced a new synthetic strategy capable of metalating NU-1000 MOFs from the gas phase using a novel vapor-phase synthetic technique – atomic layer deposition (ALD) showing in the Figure 1.5[29]. The results showed that the Zr sites in NU-1000 were inactive towards the Knoevenagel condensation which is used to indicate the catalytic behavior. However, Zn-AIM and Al-AIM were active in the catalytic assessment. This is due to the presence of Lewis acidic Zn (II) and Al (III) sites in the framework.

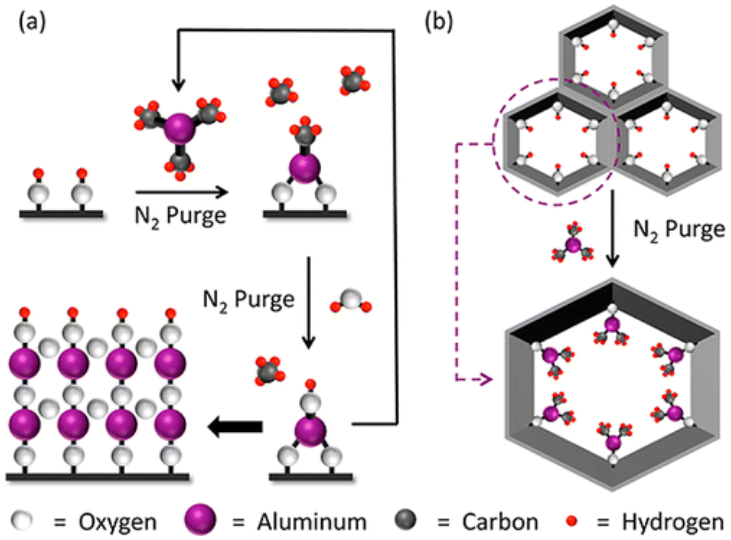

Figure 1.5 Illustration of (a) Thin film ALD deposition on a surface and (b) metalation by ALD in a MOF (AIM). Adapted from Ref.[29].

1.3 Metal-organic Framework in Biomedical Applications

With the enormous achievements of MOFs been made in chemical applications such as gas storage, separation, catalysis, *etc*., scientists start to seek opportunities for applications across biology and medicine. The study of MOFs in bio-related applications encompasses not only the structural diversity and inner porosity of MOF materials but also size, dimensionality, shape, chirality, biocompatibility, stability, molecular recognition and biomolecular function. MOFs that designed for bio-applications usually use some biomolecules as multifunctional ligands including nucleobases, amino acids, peptides, proteins, cyclodextrins and porphyrins/metalloporphyrins. Increasing studies have focused on using MOFs as platforms in biomedical applications including biosensing, biomedical imaging, drug delivery, phototherapy, *etc*.

1.3.1 MOF in Biosensing

The increasing demands for accurate biosensing have significantly promoted the design and discovery of functional nanomaterials. Similar to many other organic and inorganic materials such as metallic nanoparticles, graphene oxide (GO), molybdenum disulfide (MoS_2), silica nanoparticles, and quantum dots (QDs), MOFs have been considered as

promising tools for biomolecules detection. Because MOF structures are constructed with nearly infinite organic ligands with numerous possible functional sites that would enable specific molecular recognition. The MOF-based biosensing can be mainly classified as two categories: (1) MOFs as fluorescence quenchers toward the fluorophores of analytes based on fluorescence resonance energy transfer (FRET)[30] or photoinduced electron-transfer (PET) or charge transfer. (2) MOF themselves as fluorophores which can selectively respond to analytes[31]. W. Chen and co-workers used a water-stable three-dimensional Cu-based MOF – $[Cu_3(Cmdcp)_2(dps)_4\ (H_2O)_4(SO_4)]_n$ (1, H3CmdcpBr = N-carboxymethyl-3,5-dicarboxylpyridinium bromide; dps =4,4′-dipyridyl sulfide to selectively detect HIV-1 double-stranded DNA (HIV ds-DNA) and Sudan virus RNA (one type of ebolaviruses, SUDV RNA) sequences[32]. Specifically, probe DNA was bound to MOF and its fluorescence was efficiently quenched due to PET effect. However, in the presence of HIV ds-DNA or SUDV RNA sequences, probe DNA is released from MOF and hybridizes with target sequences, leading to the fluorescence recovery of probe DNA (Figure 1.6). Similarly, Li and co-workers used MIL-101 ($Cr_3F(H_2O)_2O[(O_2C)–C_6H_4–(CO_2)]_3\cdot nH_2O$) as a fluorescence quencher to decrease the high background fluorescence of SYBR Green I (SG)-probe DNA complex for the detection of target DNA. Several other functional MOFs, including MIL-101, MIL-88A, UiO-66-NH_2, and Gd-based coordination polymer have also been employed as fluorescent sensing platforms for nucleic acid detection with excellent sensitivity and selectivity. Xia and co-workers synthesized a 2D ultrathin lanthanide-based MOF $[La_2(TDA)_3]_2H_2O$ using 2,2′-thiodiacetic acid ($S(CH_2COO)_2^{2-}$, TDA) as the bridging ligand and used this Ln-MOF as a fluorescent DNA sensor for the detection of target DNA[33]. Unlike other traditional 2D materials (*e.g.*, GO and MoS_2), such MOF nanosheets show different fluorescence quenching properties as the fluorescence

quenching or recovery is based on the charge properties (positive or negative) of the labeled dyes. The sensing mechanism is that the negatively charged dye experiences a fluorescence turn-down "followed by turn-down" process, whereas the positively charged fluorophores resulted in a fluorescence "turn-down" followed by "turn-up" process.

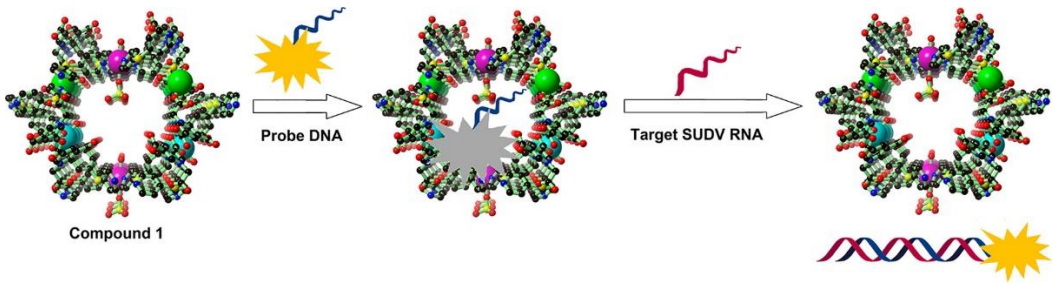

Figure 1.6 Detection of target SUDV RNA sequences based on a fluorescent biosensor based on Cu-MOF and fluorophore-labeled probe DNA. Adapted from Ref.[32].

Dopamine (DA) is a representative catecholamine neurotransmitter existing in the central nervous system, and is important in the functioning of central nervous, cardiovascular, and hormonal systems. Several MOFs have recently been developed for tracing DA in biologic fluids. Chen and co-workers reported that Cu-BTC (HKUST-1) can catalyze the chemiluminescence (CL) reaction of luminol – H_2O_2 system and enhance the CL intensity by 90-fold in an alkaline medium[34]. The luminol–H_2O_2–HKUST-1 CL system can be effectively inhibited by the introduction of DA. This MOF-based CL sensor presented a wide detection range of 0.01 – 0.7 µM with a LOD of 2.3 nM. A nanocomposite that consists of QDs and MOFs was designed by Lin and co-workers for gelatinase A – a crucial member of matrix metalloproteinases enzyme activity sensing based on FRET between semiconducting polymer dots (P-dots) and $[Cu(H_2DTOA)]_n$ MOF[35]. The fluorescence of P-dots was quenched by the $[Cu(H_2DTOA)]_n$ with the assistance of the polypeptide chain linker (COOH-GHHYYGPLGVRGC-NH_2) through the FRET process. The fluorescence can be recovered as the P-dots will release from the MOF in the presence of gelatinase A.

Other MOFs-based sensing methods have been developed for reactive oxygen species (ROS) (such as O_2^-, OH•, RO•, $^1O_2$, *etc*.) as well as H_2O_2 detection in biological samples via colorimetry or electrochemical methods[36-39].

1.3.2 MOF in Biomedical Imaging

1.3.2.1 Fluorescent imaging

A fluorescent probe is always demanded for the successful detection of intracellular species since it can report intracellular signals noninvasively. Several fluorescent MOFs at nanoscale have been recently developed for bioimaging, particularly intracellular imaging. Zhang and co-workers reported the design and synthesis of the first NMOF-based sensor for the detection of the physiologically relevant thiol species Cys and GSH in living cells[40]. The maleimide group which is known to be highly selective thiol-reactive fluorescence probe quenches fluorescence in its conjugated form, but not as the thiol adduct. The maleimide-attached ligands of H2L1 and H2L2 were incorporated in the Mi-UiO-66 and Mi-UiO-67 structure which could sense the Cys and GSH at an ultralow concentration of 10^{-11} M. Liu and co-workers synthesized a fluorescent hierarchical-pore MOF (H-MOF) via a one-pot approach incorporated with rhodamine B (RhB) as a modulator and a fluorescent imaging reagent[41]. The results demonstrated that instead of interfering with auto-fluorescence *in vivo* imaging, the red fluorescence of RhB remains in the H-MOF and realize a high quantum yield and low-background imaging. Meanwhile, this H-MOF was capable of encapsulating 5-Fluorouracil (5-FU) – one of the major clinically applied anticancer agents and deliver it to the tumor site for cancer therapy.

1.3.2.2 X-ray computed tomography (CT)

CT is a medical imaging technique based on X-ray attenuation that can provide 3D images with excellent spatial resolution. Elements with high atomic numbers (high-Z

elements), including iodine, barium and bismuth, generally show high X-ray attenuation, thus are typically used as CT contrast agents. However, these elements are always demanded in large doses (tens of grams) to achieve adequate contrast. Nanomaterials particularly nanoscale MOFs can provide high quality contrast yet using lower dosage of nanomaterials. Lin and co-workers used iodixanol-modified ligands terephthalic acid (BDC) I_4-BDC and Cu^{2+} or Zn^{2+} to construct nanoscale MOFs for CT contrast agents. The nanoscale MOF carried high payloads of iodine (ca. 63 wt %) and showed that both MOFs possessed slightly higher X-ray attenuation factors than the commercially used contrast agent iodixanol in phantom studies[42]. Zhang and co-workers synthesized ultrasmall poly(vinylpyrrolidone) (PVP)-protected bismuth nanodots – PVP-Bi nanodots via an ultrafacile and organic solvent free strategy[43]. The ultrasmall PVP-Bi nanodots with good biocompatibility have prominent performance on X-ray CT imaging due to the high X-ray attenuation ability of Bi element. PVP-Bi nanodots could be efficiently internalized by cancer cells and displayed a concentration-dependent internalization behavior (Figure 1.7).

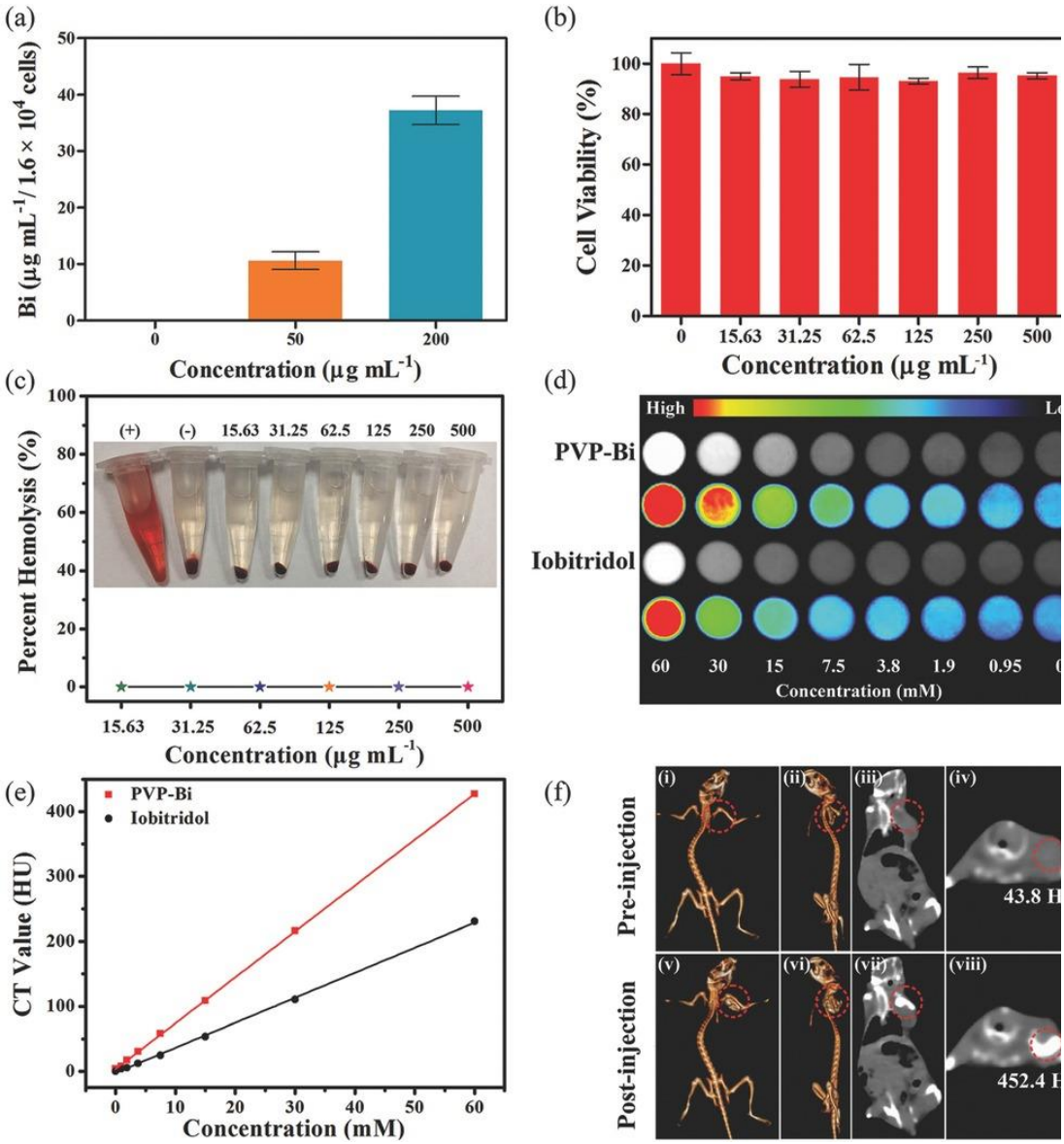

Figure 1.7 Concentration-dependent cellular internalization measured by ICP-MS. b) cytotoxicity of PVP-Bi nanodots to U14 cells. c) Hemolytic percent of red blood cells incubated with PVP-Bi nanodots at various concentrations for 4 h. d) *In vitro* CT images of solutions of PVP-Bi nanodots and iobitridol with different concentrations. e) The HU value of PVP-Bi nanodots and iobitridol as a function of the concentrations of Bi and iobitridol, respectively. f) CT images of a tumor-bearing Balb/c mouse: pre-injection (i–iv) and after injection (v–viii) in situ. Adapted from Ref.[43].

Lin and co-workers synthesized two MOFs containing two different high-Z elements zirconium (Zr) and hafnium (Hf) – Zr-UiO-66 and Hf-UiO-66 by a solvothermal method. Instead of incorporating the high-Z element into the bridging ligand of the structure, they incorporated the high-Z elements (Hf and Zr) into the secondary building units in the framework. The metal-carboxylate clusters $M_6(\mu_3\text{-}O_4)(\mu_3\text{-}OH)_4(RCO_2)_{12}$ (M = Zr or Hf) as secondary building units were bridged by benzenedicarboxylate ligands. The results of *in vitro* CT measurement showed that the

slopes of the lines produced by plotting CT values against Hf/Zr/I concentrations for Hf-UiO, Zr-UiO, and iodixanol are 10740 ± 390, 5600 ± 180, and 5390 ± 230 HU M^{-1}, respectively, indicating that Hf-MOF and Zr-MOF were more suitable for CT imaging as compared to iodixanol[44].

1.3.2.3 Magnetic resonance imaging (MRI)

Magnetic resonance imaging (MRI), a noninvasive imaging technique in radiology based on the detection of nuclear spin reorientations in a magnetic field, provides 3D detailed anatomical images with high spatial resolution, and a large penetration depth. Gd^{3+} – and Mn^{2+} – based MOFs have been well studied for T_1-weighted MR imaging in the recent years. Yin and co-workers developed a uniform nanoscale coordination polymers (NCPs) spheres with Gd^{3+} and Ru[4,4′-$(COOH)_2$ bipyridyl(bpy)]$_3^{2+}$ (LRu) as precursors[45]. This Gd–Ru MOFs were synthesized via a hydrothermal treatment of Gd^{3+} and LRu, with average diameter of 138 nm according to the TEM characterization. The red fluorescence of L_{Ru} and high longitudinal relaxivity of Gd^{3+} in the MOF enabled the fluorescence-magnetic resonance (MR) dual-modality imaging. Moreover, this Gd-Ru-MOF had a better performance as MR contrast agent compared to the commercial MR contrast Gd-DTPA (diethylenetriamine pentaacetic acid). Another multifunctional nanoscale MOF carrying exceptionally high loadings of the anticancer drug – zoledronate and T_1-weighted MRI contrast agent – Mn^{2+} ion was reported by Lin and co-workers. This MOF integrated imaging and therapy into one single platform for cancer specific diagnosis and chemotherapy[46]. The group also reported $Gd(BDC)_{1.5}(H_2O)_2$ (1) nanorods (where BDC is 1,4-benzenedicarboxylate) prepared by a reverse microemulsion method. This Gd-MOF exhibited extraordinarily large R_1 and R_2 relaxivities because of the presence of up to tens of millions of Gd^{3+} clusters in each nanoparticle, thus provided efficient T_1 and T_2 contrast agents for MRI. Furthermore,

by doping with Eu^{3+} or Tb^{3+} metal, this MOF had excellent fluorescence emission, which allowed for multimodal imaging[47].

1.3.2.4 Positron emission tomography (PET)

Positron emission tomography (PET) is another highly sensitive non-invasive imaging technique that is ideally suited for pre-clinical and clinical imaging of cancer biology. Today, PET is developed as powerful tool for monitoring cell/molecular events early in the course of a disease, as well as during pharmacological or radiation therapy. Natural biomolecules can be labeled with an isotope capable of producing two gamma-rays while emitting a positron. This positron eventually collides with a nearby electron and produces 511,000 eV gamma-rays. Common isotopes include ^{15}O, ^{13}N, ^{11}C and ^{18}F with some other less commonly used isotopes such as ^{14}O, ^{64}Cu, ^{62}Cu, ^{124}I, ^{76}Br, ^{82}Rb (rubidium) and ^{68}Ga (gallium). Nanomaterials have been used as imaging probes for PET for decades. Examples of which include ^{69}germanium-labeled iron oxide nanoparticles, ^{125}I-labeled gold nanorods, ^{64}Cu labeled CuInS/ZnS quantum dots, *etc*. More recently, there are also growing research interests in developing a single hybrid nanoprobe for multi-modality imaging, which provides high sensitivity, real-time and detailed 3D anatomical information. Cheng and co-workers developed a single nanoplatform composed of two different functional nanomaterials gold and iron oxide particles (Au-IONPs) as affibody based triple-modality imaging probe (PET, MRI, OI) for targeting the epidermal growth factor receptor (EGFR) positive tumors. The IO component functioned as T_2 MRI contrast agent whereas gold component with targeting molecules and radiometal ^{64}Cu chelators served as both optical and PET reporters for tumor imaging[48]. Chen and co-workers described an approach to synthesize an intrinsically radioactive nanoprobe ^{64}CuInS/ZnS QDs by directly incorporating ^{64}Cu into CuInS/ZnS nanostructure with $^{64}CuCl_2$ as synthesis precursor.

This hybrid nanoprobe has improved radioactive stability for PET and Cerenkov resonance energy transfer (CRET) luminescence dual modal imaging of U87MG glioblastoma models[49]. Yoo and co-workers reported a triple-modality, optical/nuclear/magnetic imaging probe based on radiolabeled superparamagnetic nanoparticles. ^{124}I was selected to incorporation in the nanopore because of its sufficiently long half-life (4.2 days). The thermally cross-linked SPION with higher T_2 relaxivity coefficient (R_2) than conventional SPIONs served as excellent T_2 MR imaging contrast agent[50]. This triple-modality imaging agent has a superior performance in *in vivo* imaging studies using small animals such as mice and rats.

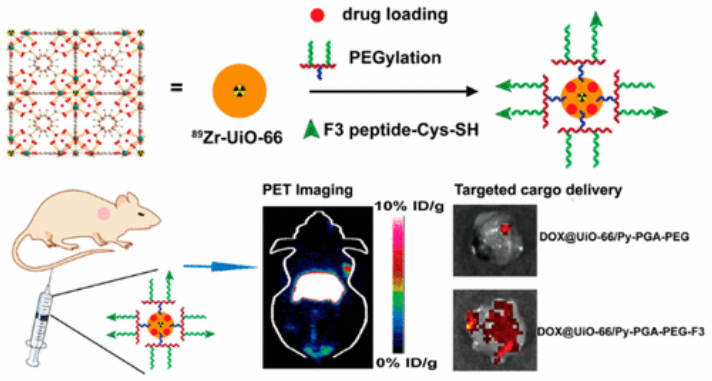

Figure 1.8 Schematic synthesis route of ^{89}Zr-UiO-66/Py–PGA-PEG-F3 conjugates. Adapted from Ref.[51].

An intrinsically radioactive UiO-66 MOF was reported with incorporation of PET isotope ^{89}Zr by Hong and co-workers[51]. The ^{89}Zr-UiO-66 was functionalized with pyrene-derived polyethylene glycol and a targeting peptide to recognize the breast tumors. DOX was also incorporated in the MOF with a relatively high loading capacity for tumor chemotherapy (Figure 1.8). Py-PGA-PEG improved the toxicity of the nanoprobe and did not impose acute or chronic toxicity to Balb/c mice according to histological staining and serum biochemical assays. The nanoprobe allowed PET imaging-guided tumor chemotherapy.

1.3.3 MOF in Targeted Drug delivery

The delivery of chemodrugs to tumor tissue is the dominant treatment method for cancer therapy. Traditional direct administration of therapeutic drugs to patients have intrinsic limitations. For example, traditional drug administration usually causes undesirable side effects, and the poor pharmacokinetics and uncontrollable biodistribution are likely to influence the therapeutic efficacy of the drugs. An ideal drug-loading system should meet the following basic requirements to achieve effective drug delivery: carriers should have a large drug loading capacity; carriers should be nanoscale in order to facilitate the release of drugs by intravenous administration; carriers should have low toxicity to the normal tissues; carriers should reach the desired sites after administration, with minimal loss of the dose and activity in blood circulation[52]. Among various drug vehicles that have been developed for the controllable drug release in the recent years, MOF-based nanocarriers received extensive attention in the development of drug delivery and cancer theranostic platforms due to the versatile structures, tunable pore size, high loading capacity, controllable size, excellent biodegradability, diversity of surface functionalization, *etc*.

Férey and co-workers developed a synthesize two new cubic (Fd3m) zeotypic metal carboxylates – MIL-100 (Cr) and MIL-101 (Cr) composed of trimers of metal octahedra and di- or tricarboxylic acids via targeted chemistry and structural computer predictions[53]. These structures were proved to be initially hydrated and exhibit giant pores (pore size: ~ 25 – 34 Å) and unprecedented surface areas (3100 – 5900 $m^2 g^{-1}$) without any loss of crystallinity after water evacuation. They also studied the adsorption and delivery of a model analgesic and anti-inflammatory drug – Ibuprofen, by the two synthetic MIL MOFs. However, this study has its limitation because it is chromium-based materials which is well known for their toxicity. The same group also reported

flexible nanoporous chromium or iron terephtalates (BDC) MIL-53 (Cr, Fe) for the adsorption and *in vitro* drug delivery of Ibuprofen[54]. Wang and co-workers developed a chiral nanoporous MOF with high porosity based on nontoxic zinc and achiral hexadentate ligand 5,5′,5″-(1,3,5-triazine-2,4,6-triyl)tris(azanediyl)triisophthalate (TATAT). The chiral MOF can be used as drug carrier for the adsorption and delivery of anticancer drug 5-fluorouracil (5-Fu). The experimental results indicated that the material had a high loading capacity of 50 wt% of the transported drug and a slow release of loaded drug about one week[55]. Gref and co-workers developed a specific non-toxic porous iron (III) carboxylate MOF with engineered cores and surfaces, as well as imaging properties (Figure 1.9)[56]. They tested the drug loading efficiency of the iron MOFs with four challenging anticancer or antiviral drugs busulfan (Bu), azidothymidine triphosphate (AZT-TP), cidofovir (CDV) and doxorubicin (DOX)) and obtained exceptionally higher Bu entrapment in the microporous structures MIL-100 (25 wt%) than that of in the MIL-88A, MIL-53, and MIL-89. Moreover, the study demonstrated that MIL-100 can load up to 25, 21, 16 and 29 wt% of Bu, AZT-TP, CDV and DOX, respectively. An unprecedented capacity of 42 wt% can be achieved for AZT-TP and CDV with MIL-101-NH_2 MOFs solids.

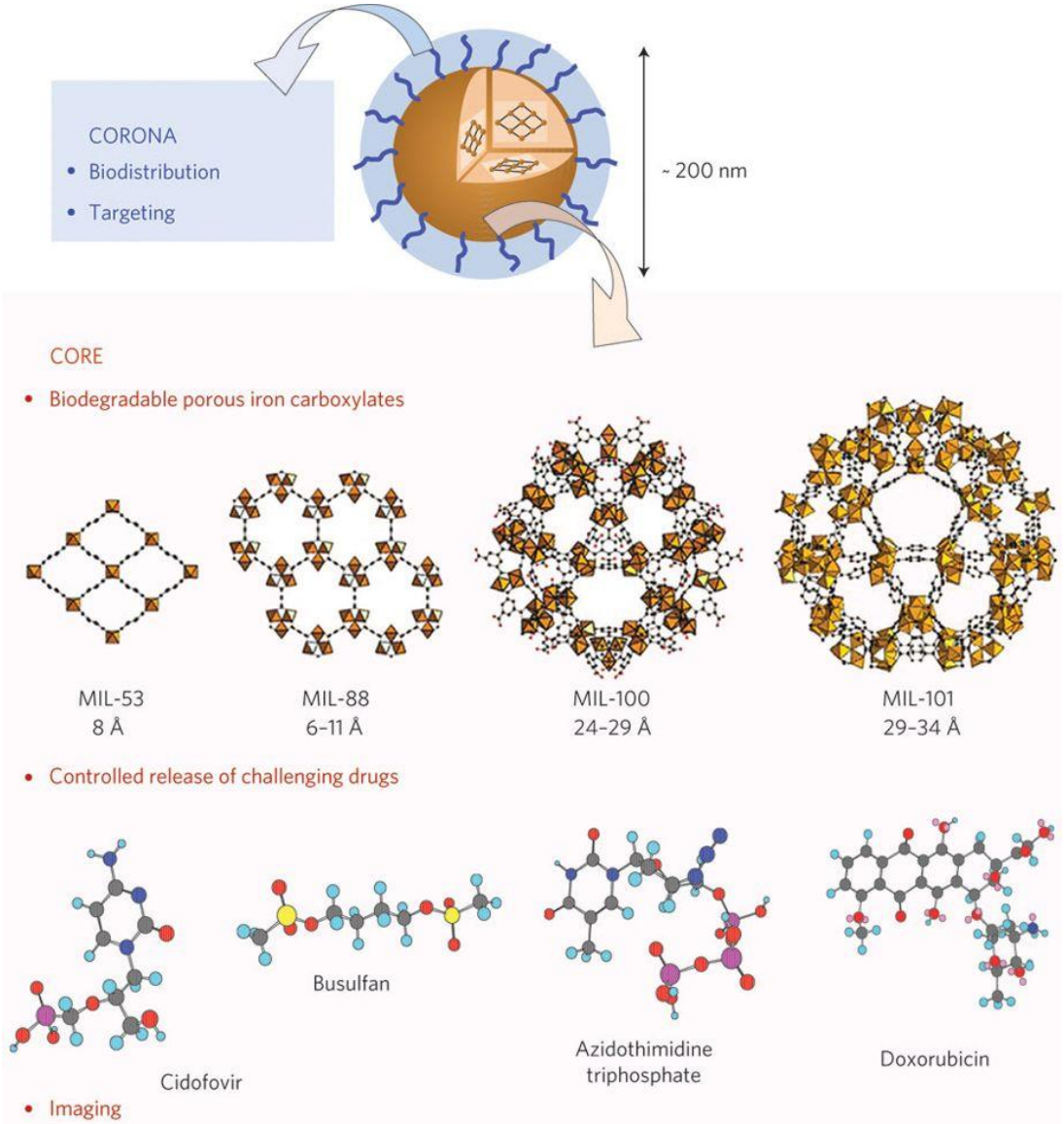

Figure 1.9 Scheme of engineered core–corona porous iron carboxylates for drug delivery and imaging. Adapted from Ref.[56].

1.3.4 MOF in Phototherapy

Phototherapy begins in 1903 when Niels Ryberg Finsen was awarded the Nobel Prize in Physiology or Medicine for using short wavelength light to treat lupus vulgaris. Today, phototherapy has expended its applications to the treatment of many other diseases such as atopic dermatitis, psoriasis, vitiligo, acne vulgaris, and cancer. Phototherapy uses photosensitizer or photothermal agents to absorb and transfer energy from light to molecular oxygen, to generate ROS in photodynamic therapy (PDT) and photothermal responses in photothermal therapy (PTT)[57].

1.3.4.1 Photodynamic therapy (PDT)

PDT involves three intrinsically non-toxic components that are combined to induce cellular and tissue effects in an oxygen-dependent manner. The first component is the photosensitizer (PS) – a photosensitive molecule that can be promoted to excited state and react with nearby oxygen to generate singlet oxygen ($^1O_2$), a particular form of ROS. The second component is the administration of light of a specific wavelength that activates the sensitizer. By localizing the PS and light to the tumor region, the generated $^1O_2$ can selectively kill the tumor cells without affecting the surrounding normal tissues. Therefore, PDT has been employed to treat many different kinds of cancers, including esophageal cancer, non-small cell lung cancer, and head and neck cancer[58-60]. Nanoparticles due to their unique physiochemical properties, have been used in PDT for the past decades, of which nanoscale MOFs received extra attention[61]. Compared to other pure organic or inorganic PSs, MOFs possess several advantages: 1) high porosity of nanoscale MOFs permits a high payload of photosensitizers; 2) porous nature of MOF structure facilitates the easy diffusion of molecular oxygen; 3) biodegradability of nanoscale MOFs alleviates the concern of long-term toxicity[62-63].

However, not until the year of 2014 did scientists reported the first MOF as a PS for photodynamic therapy of resistant head and neck cancer[64]. The study demonstrated a new approach to synthesize Hf-porphyrin nano MOF by a solvothermal reaction between $HfCl_4$ and 5,15-di(p-benzoato)porphyrin (H_2DBP) in *N*,*N*-dimethylformamide at 80 °C (Figure 1.10). The DPB ligands periodically separated by the metal clusters allowed efficient absorption of light and facile $^1O_2$ diffusion out of the porous MOF. Both *in vitro* and *in vivo* PDT efficacy studies demonstrated significant cancer cell death and tumor volume reduction in mice group treated with

light-activated DPB-UiO MOF. The study also found no therapeutic effect observed in the mice treated with H_2DPB alone.

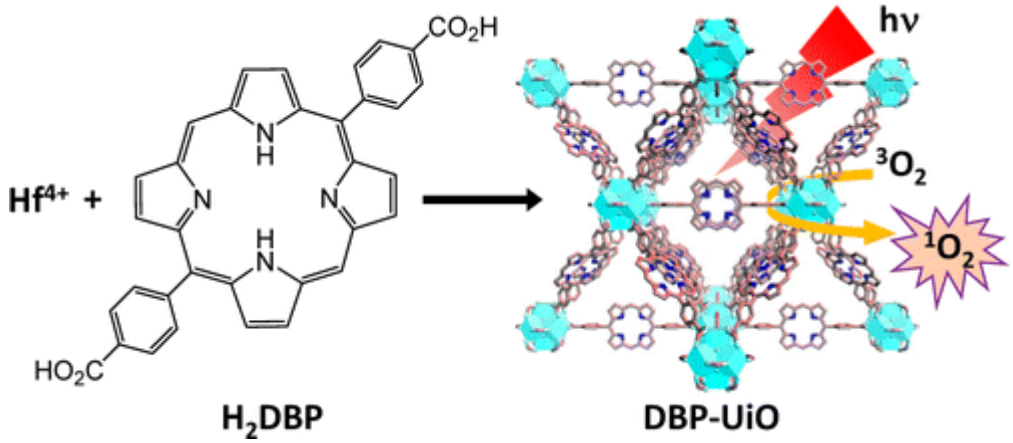

Figure 1.10 Synthesis of Hf–DBP nano MOF and the schematic description of singlet oxygen generation process. Adapted from Ref.[64].

The same group also reported a chlorin-based nanoscale MOF, DBC-UiO, with much improved photophysical properties over the previously reported porphyrin-based NMOF, DBP-UiO. They slightly modify the organic ligand by reducing the 5,15-di(p-methylbenzoato)porphyrin DBP ligands in DBP-UiO to the 5,15-di(p-methylbenzoato)chlorin (DBC) ligands in DBC-UiO resulted in a 13 nm red shift and an 11-fold increase in the extinction coefficient of the lowest-energy Q band. The chlorin DBC-UiO MOF with exceptionally high PS loading exhibited a three times higher 1O2 generation ability and improved PDT cytotoxicity in two colon cancer cell line CT26 and HT29 cells[65]. Another Hf-TBC-MOF formed by chlorin derivative, 5,10,15,20-tetra(p-benzoato)chlorin (H4TBC) and $Hf_6(\mu3\text{-}O)4(\mu3\text{-}OH)_4$ units. The IDO inhibitor (IDOi) was encapsulated in the framework to enable a novel cancer treatment strategy by integrating MOF-based PDT and IDOi-based immunotherapy[66]. Zhou and co-workers present a functional MOF, namely SO-PCN (singlet oxygen-generating porous coordination network) that constructed with porphyrin derivatives tetrakis(4-carboxyphenyl)-porphyrin (TCPP) and zinc[67]. As a solid-state material which inherently incorporated photosensitizer porphyrin, Zn-TCPP has demonstrated

reversible control of $^1O_2$ generation ability. In addition to the $^1O_2$ generation, Zn-TCPP also showed its catalytical activity and was able to catalyze the oxidation of DHN which is mediated by $^1O_2$ and resulted in the corresponding oxidized product juglone.

1.3.4.2 Photothermal therapy (PTT)

Thermal therapy, often known as hypothermia and thermal ablation, is an emerging cancer treatment that uses localized heat generated by radiofrequency pulse, microwave radiation, and ultrasound wave to damage the tumor tissue. PTT is one of those therapeutic approaches induced by near-infrared (NIR) light to generate elevated temperature to suppress the tumor growth. Light absorption and photothermal conversion efficiency together determine the performance of a PTT agent. Many inorganic nanostructures have been developed for as PTT agents for treating cancer in the past decades, for example, gold nanoparticles[68], carbon nanotubes[69], carbon nanodots[70], iron oxide nanoparticles[71], palladium (Pd) nanosheets[72], *etc*. Organic polymers, such as polypyrrole[73] and polydopamine[74] with surface coatings to increase blood circulation time and to reduce toxicity also have been employed as PTT agent for many disease treatments. PTT attracts tremendous research attention because it shows remarkably reduced side effects and improved selectivity since only the lesion exposed to the light is treated, while other tissues in the dark are not affected[75].

Multifunctional nanoscale MOFs have been demonstrated for enhanced PTT in many studies in the past several years. Both metal-cluster SBUs and bridging linkers can be utilized to convert light to thermal energy or functionalized to enhance photothermal conversion efficiency. Furthermore, encapsulation of external photothermal agents in MOF cavities can further enhance the efficacy of PTT and PTT-based combinatory therapies. Chen and co-workers synthesized a novel core-shell PB@MIL-100(Fe) dual MOFs nanoparticles for multimodal imaging (MRI, FOI), PTT,

and chemotherapy[76]. The hybrid MOF nanoparticles can serve as a T_1/T_2 dual-modal MRI and FOI which can be attributed to MIL-100 (Fe) and Prussian Blue. This theranostic platform also allowed chemotherapy because of the encapsulation of a traditional Chinese anticancer medicine artemisinin, with a high loading capacity of 848.4 mg g^{-1}. The drug release can be triggered by the pH-responsive degradation of outer MOFs in the low pH lysosomes of tumor cells. Moreover, the inner PB particles can serve as a photothermal agent due to the strong absorbance of NIR light. This nanoprobe was able to realize dual-modal imaging-guided photothermal/chemotherapy with assistance of NIR light irradiation. *In vivo* photothermal and chemotherapy experiment was carried out in animal model, the results of which indicated an effective tumor ablation. histological analysis demonstrated that the drug delivery system had no obvious effect on the major organs of mice.

Zhu and co-workers developed a multifunctional MOF-platform composed of zeolitic imidazolate framework-8 (ZIF-8) and graphene quantum dots (GQDs) with anticancer drug- DOX encapsulated in the micropores of MOF for synergistic chemo- and photothermal therapy[77]. Due to the weak coordination between DOX and zinc, DOX molecules were able to in situ encapsulated in the ZIF-8 during the crystal growth. The multiple components have several functions: 1) ZIF-8 served as a carrier to incorporate drug molecules and GQD via hydrogen bonding interaction between the N–H groups of 2-methylimidazole in ZIF-8 and the hydroxyl, epoxy, and carboxyl groups on GQDs; 2) GQDs induced excellent photothermal effect under NIR light irradiation; 3) DOX can be released from the ZIF-8 upon entering the acidic environment in cancer cells. The PTT effect of GQDs not only induced cancer cell death but also enhanced drug release from ZIF-8.

1.4 Future Directions and Prospects

The next major breakthrough will be not only the study of new structures of MOFs, but also the discovery of the novel applications particularly in the biomedical area. MOFs can go beyond gas storage, gas separation and enantioselective separations, through the incorporation of a variety of metal ions/metal clusters, organic linkers and encapsulated species within pores with biological functions. Considering the large number of existing bio-MOFs, most of which still focus on the cancer-related theranostic applications, only very limited amount of studies uses MOFs to address the problems in infectious diseases, neurodegenerative diseases, arthritis, immune disorders, *etc*. Applications of engineered MOFs should expend to other areas to solve more extensive medical problems based on their tremendous advantages.

MOFs are also facing numerous challenges when translated to practical use. The controllable synthesis of small particle size and desired pore size remain an issue for many MOF structures. Preventing the agglomeration of MOF nanoparticles is still waiting to be fully understood. By engineering the surface of MOF nanoparticles with various reactive groups, it may be possible to integrate more theranotic functions in a single nanoprobe. In addition, understanding the mechanism of biodistribution and biodegradation of MOFs in the body is another critical step before practical use in biomedicine. Despite many issues that need to be addressed, the diversity and extraordinary physicochemical properties of MOFs will strengthen the interest in further developing MOF-based biological applications.

1.5 Motivation and Objectives

Developing a controlled approach for synthesizing nanoscale MOFs for chemical sensing and disease treatment is crucial in both chemical and biomedical applications. Although a variety of MOFs have been developed for chemical sensing, particularly

metal ion sensing, many of them suffering from poor dispersity in aqueous solution, thus those MOFs only detect ions in organic solutions such as DMF. In addition, most of the reported MOFs that are synthesized for chemical sensing are in micro scale and have less surface area compared to nanoscale MOFs. As a result, these types of MOFs cannot react with the analytes and display the signal immediately as the reactions usually take a certain period of time. Some MOF-based sensors can react with the analytes in short time, allowing the detection process to be completed within a few seconds, but have a limited practical use because of the requirement of costly apparatus[78]. Current, most of MOFs used in biomedical applications mainly focus on the cancer diagnosis and therapy as reviewed above, yet none of them have extended their applications to the treatment of neurodegenerative diseases including Alzheimer's disease (AD), Parkinson's disease (PD), *etc*. Engineered nanoscale MOFs with ultrahigh stability are suitable for many brain diseases in terms of controlling protein self-aggregation.

Specific objectives of chapter 2 include:

1. To synthesize Zn-MOF-74 nanodots with ultrasmall size under 5 nm that can quickly react with the substrate Fe^{3+} and change its color in aqueous solution.
2. To characterize the Zn-MOF-74 nanodots using various techniques.
3. To develop a Fe^{3+} ion sensor with high selectivity and sensitivity based on nanoscale Zn-MOF-74.
4. To investigate the mechanism of the Fe^{3+} ion sensing based on the Zn-MOF-74.

Specific objectives of chapter 3 include:

1. To synthesize porphyrin PCN-224 nanoparticles (~ 70 nm in diameter) through a solvothermal method.

2. To investigate the physical and chemical properties of PCN-224 nanoparticles using various techniques.
3. To investigate the inhibitory effect of PCN-224 nanoparticles on the Aβ aggregation under 650 nm light irradiation.

Specific objectives of chapter 4 include:

1. To prepare the hybrid nanosystem – PCN-222@ICG@RVG and characterize its physical and chemical properties.
2. To investigate the photodynamic and photothermal effect of PCN-222@ICG@RVG.
3. To study the capability of PCN-222@ICG@RVG to prevent Aβ monomers from aggregating into high-order oligomers and fibrils under 808 nm light irradiation.
4. To build a Transwell model that mimics the blood-brain barrier *in vitro* for the investigation of BBB translocation of the hybrid nanoprobes.

Specific objectives of chapter 5 include:

1. To fabricate a microdevice through soft lithography and use it as organ-on-a-chip model for drug testing study.
2. To establish the brain chip model by co-culturing human primary endothelial cells (HUVEC), astrocytes, pericytes to mimic the human brain microenvironment.
3. Use the brain chip model to test the BBB permeability of PCN-222@ICG@RVG and carbon nanodots and see whether the brain targeting peptide RVG could improve the BBB transport of nanoprobes.

2 Ultrasmall Zn-MOF-74 Nanodots for Colorimetric Fe^{3+} Sensing

The original work described in this chapter was published (Wang et al. ACS Appl. Nano Mater. 2018).

2.1 Introduction

Fe^{3+} ion is one of the most essential elements in biological systems and plays a crucial role in several biochemical processes such as hemoglobin formation, muscle and brain function, and electron transfer processes in DNA and RNA synthesis[79]. However, excess amounts of Fe^{3+} in living systems can induce various physiological disorders including anemia, skin ailments, insomnia, dysfunction of organs, and even cancers[80]. Therefore, sensitive and selective detection of Fe^{3+} is highly demanded for the surveillance of human health. Traditional techniques for Fe^{3+} ion detection include chromatography, inductively coupled plasma mass spectrometry (ICP-MS), and atomic absorption spectroscopy. However, these techniques suffer from the complex operation, requirement of bulky apparatus, and high cost. Therefore, it is of high importance to develop a rapid, simple and low-cost approach for sensitive detection of Fe^{3+} ion. Numerous MOFs have been used for ion sensing for many years, of which fluorescent-based sensing approaches are more common. Several lanthanide-based MOFs (Ln-MOF) such as Tb- and Eu-MOF, owing to their unique optical properties, are widely used as fluorescent sensors for Fe^{3+} based on dynamic or static quenching effects. These fluorescent sensors usually are based on bulk MOF materials, thus resulting in relatively low sensitivity and slow signal response due to the relatively small surface area of the interaction between MOFs and metal ions. In addition, many MOFs can only be dispersed in organic solution, thus they are not suitable for ion sensing in aqueous and biological environment. Here, we have successfully synthesized zero-dimensional (0D) nanostructured zinc-based MOF with ultrasmall size under 5 nm and developed a

simple and label-free colorimetric approach based on ultrasmall Zn-MOF-74 nanodot for highly sensitive and selective Fe^{3+} sensing. This platform allowed rapid detection of Fe^{3+} through a colorimetric change to blue within a few seconds. The ultrasmall-size and highly dispersible and stable nature in aqueous solutions make this Zn-MOF-74 nanodot a potential candidate for Fe^{3+} sensing in environmental and biological systems.

2.2 Methodology

2.2.1 Synthesis of Zn-MOF-74 Nanodots

Zn based MOF nanodots were prepared based on a facile method and carried out at room temperature. Briefly, 30 mL solution containing 0.6 mmol of 2,5-dihydroxyterphthalic acid (DOBDC) in DMF was added dropwise over 60 mL DMF solution of Zinc acetate dehydrate (0.1 mM) under stirring. The above mixture was incubated at room temperature for 48 h and followed by rinsed three times with 40 mL DMF and 40 mL ethanol via centrifugation (13500 rpm, 30 min). After ultrasonic treatment for 30 mins in ice water, the yellow nanocrystal Zn-MOF-74 [$Zn_2(C_8H_2O_6)$] was then collected by filtration (Millipore, 0.22 μm) and dispersed in milli-Q water for further use.

2.2.2 Characterization of Zn-MOF-74 Nanodots

The transmission electron microscope (TEM) images of Zn-MOF-74 nanodots were collected under JEOL JEM-2100F microscope. Ultraviolet and visible (UV-vis) absorbance were measured by Ultrospec 2100 Pro spectrophotometer (Amersham Biosciences). Sample prepared by dispersing 50 μg Zn-MOF-74 nanodots powder in 1 mL water and UV quartz cuvettes was used for the UV-vis absorbance measurement. Zeta potential analysis of the Zn-MOF-74 nanodots were performed using a Malvern ZEN 3600 Zetasizer Nano System. 12 runs were performed in each measurement. Powder X-ray diffraction (PXRD) patterns were obtained on a Rigaku SmartLab

diffractometer using Cu/Kα radiation. The Fourier transform infrared (FTIR) spectra were measured using KBr pellets on the Bruker Vertex-70 IR Spectroscopy in the wavelength region of 400 – 4000 cm^{-1}. Thermogravimetric analysis (TGA) was performed using a Mettler Toledo TGA/DSC3+ instrument at a heating rate of 10 °C min^{-1} under N_2 flow. The determination of the accurate concentration of Zinc and iron was performed by inductively coupled plasma-optical emission spectroscopy (ICP-OES) on Agilent 710 Series ICP Optical Emission Spectrometer.

2.2.3 Sample Preparation for ICP Analysis.

One milliliter (1 mg mL^{-1}) solution of MOF nanodots was mixed with 0.5 mL of Fe^{3+} at concentrations of 1 mM to 25 mM. After gently shaking for 5 min, the large MOF nanocrystals were removed by centrifugation at 13500 rpm for 30 min. 0.5 mL of the above filtrate was transferred to a new tube and diluted to 5 mL with nitric acid (trace metal grade, 69%) before introduced for ICP measurement. The ICP-OES was calibrated with element standard solution prepared with 1000 ppm Zn standard and 1000 ppm Fe standard by successive dilutions with an HNO_3 5% (w/w) matrix.

2.2.4 Fe^{3+} Sensing Assay

For the colorimetric sensing of Fe^{3+} ion, 400 μL of 0.1 mg mL^{-1} Zn-MOF-74 aqueous solution was mixed with 100 μL of aqueous solution of 13 different metal ions M^{n+} (M= Mg^{2+}, Ca^{2+}, Ni^{2+}, Co^{2+}, Cu^{2+}, Cd^{2+}, Mn^{2+}, Na^{+}, K^{+}, Cr^{3+}, Fe^{2+}, Al^{3+}, Fe^{3+}). After pipetting for several times, the mixture was subjected to the UV-vis spectrometer to obtain the UV-vis absorption spectrum. The characteristic peak at 600 nm is measured and calibrated for Fe^{3+} quantitative measurement.

2.3 Results

2.3.1 Characterization of As-synthesized Zn-MOF-74 Nanodots

The controlled synthesis of stable MOF nanocrystals is always challenging, especially the synthesis of sub-100 nm nanocrystals. Many of the reported Zn-MOF-74 nanocrystals obtained via a precipitation approach are between 20 - 30 nm. We attempted to improve the synthesis conditions of this precipitation method to downsize the crystals to sub-10 nm. TEM images showed the morphology of the as-synthesized Zn-MOF-74 nanodots in the Figure 2.1. The synthesized MOF nanodots under room temperature showed good water dispersity. The typical Tyndall effect in the Figure 2.1b inset demonstrated the colloidal suspension of Zn-MOF-74 nanodots. The particle size distribution of Zn-MOF-74 ranged from 2 nm to 5 nm measured *via* the TEM images was shown in the Figure 2.1c, smaller than any previously reported Zn-MOF-74 nanoparticles whose size are usually around 30-50 nm. High resolution TEM (HRTEM) image indicated the high crystallinity of synthesized MOF nanodots with the lattice fringe around 0.207 nm, which could be assigned to [110] plane of Zn-MOF-74.

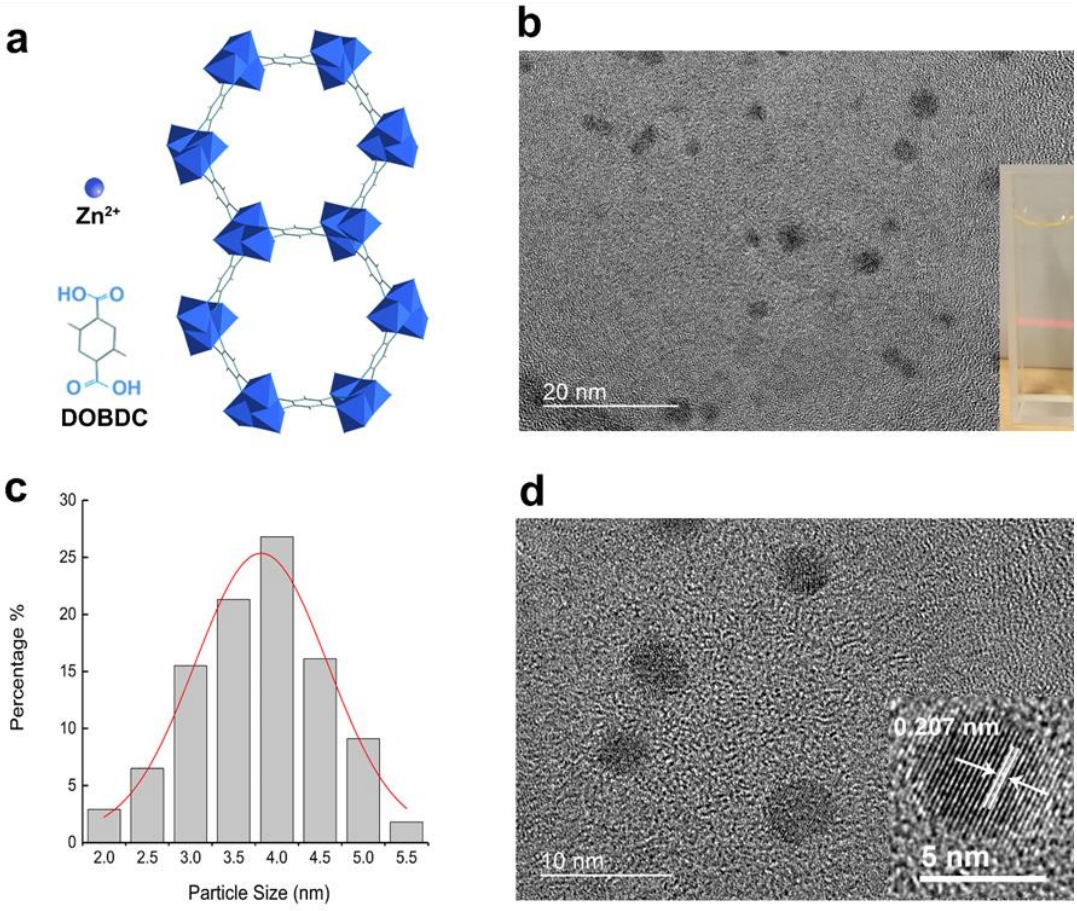

Figure 2.1 (a) Schematic architecture of the Zn-MOF-74. (b) Transmission electron microscopy (TEM) image of Zn-MOF-74 nanodot. (c) Size distribution of Zn-MOF-74 nanodots. (d) High resolution Transmission electron microscopy (HRTEM) image of Zn-MOF-74 nanodots.

The crystallinity of the Zn-MOF-74 nanodots was further determined by powder X-ray diffraction (XRD). The XRD pattern of as-synthesized MOF nanodots registered with 2θ steps of 0.01° was agreed well with the standard curve (Figure 2.2a). The peaks of the XRD patterns at ~6.8° and ~11.6° indicated the [110] and [300] reflection of Zn-MOF-74 crystals, respectively. We also analyzed the prepared MOF nanodots by thermogravimetric analysis (TGA). The TGA diagram showed that the Zn-MOF-74 nanodots exhibited high thermal stability even under the temperature of 400 °C (Figure 2.2b).

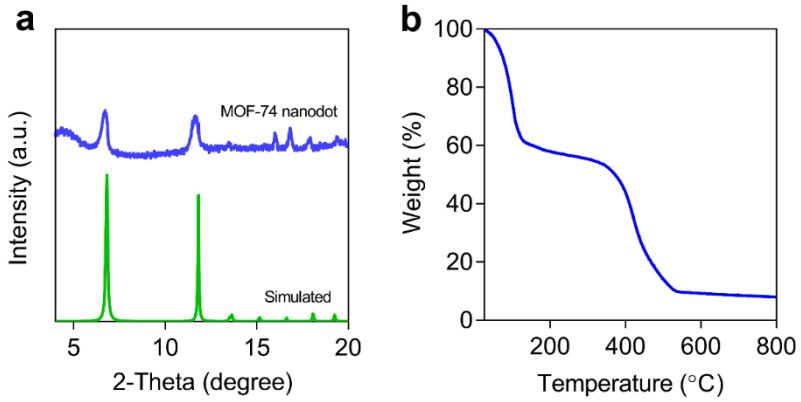

Figure 2.2 (a) Powder XRD pattern of simulated Zn-MOF-74 and as-synthesized MOF nanodots. (b) Thermogravimetric analysis (TGA) for the MOF nanodots.

Zeta potential analysis was performed to determine the surface charge of the Zn-MOF-74 nanodots. Figure 2.3a demonstrated the negative charge of Zn-MOF-74 in water with an average zeta potential value of -18 mV, indicating that Zn-MOF-74 was physically stable and well dispersed in aqueous solutions for a variety of biological applications. The Zn-MOF-74 nanodots are highly stable in aqueous solution; the transparency did not change even after 7 days standing at room temperature (Figure 2.3b). FTIR was also employed to study the surface chemistry of Zn-MOF-74 nanodots. The characteristic stretching vibrations of the coordinating carboxylate groups were observed at 1558 cm^{-1}, 1450 cm^{-1}, 1409 cm^{-1}. The transmittance at around 920 cm^{-1} could be ascribed to the -OH group. The outstanding transmittance peak at 480 cm^{-1} represented the Zn-O bond in MOF nanodot compared to that of DOBDC ligand, indicating the formation of Zn-MOF-74 framework. A weight loss of about 39% occurred in the range of 50 – 120 °C was due to the evaporation of water and organic molecules in the pores of the MOF. Around half of the weight of Zn-MOF-74 was lost in the second step when heated to 400 °C, demonstrating the decomposition of the MOF structure. The porosity of Zn-MOF-74 and Brunauer-Emmett-Teller (BET) surface area were determined and measured by nitrogen adsorption-desorption isotherm. The obtained BET surface area of Zn-MOF-74 was 314.6 m^2 g^{-1} (Figure 2.3d).

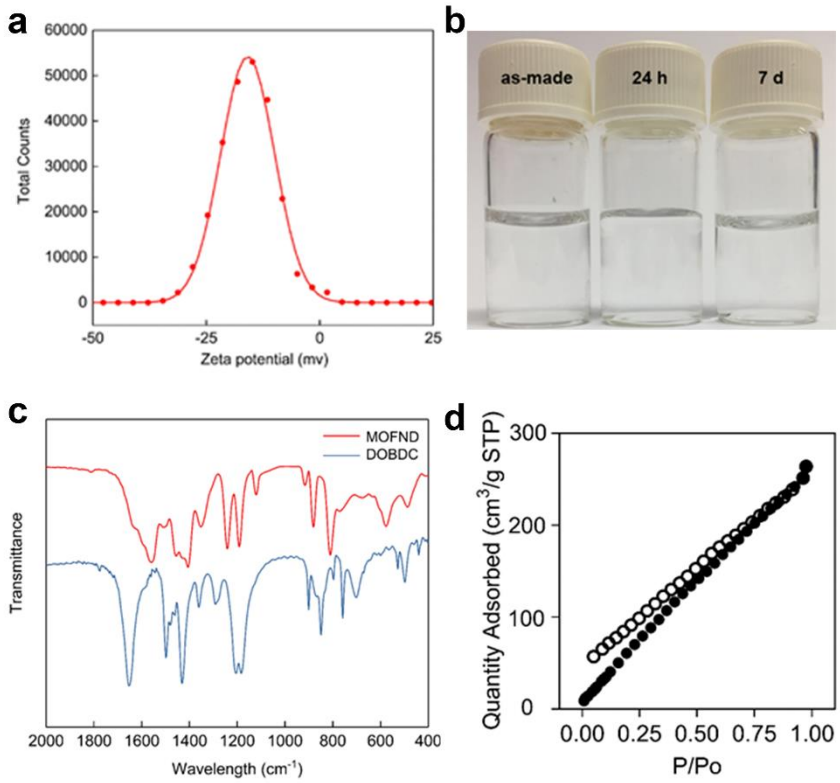

Figure 2.3 (a) Zeta potential curve of Zn-MOF-74 nanodots when pH=7.4. (b) As-synthesized MOF nanodots dispersed in aqueous solution for 24 h and 7d at room temperature. (c) FTIR spectra of MOF nanodots and DOBDC ligands. (d) Nitrogen adsorption and desorption isotherms of Zn-MOF-74.

2.3.2 Zn-MOF-74 Nanodots Based Colorimetric Fe^{3+} Sensing

The ultra-small Zn-MOF-74 nanodots can be used as a good candidate for metal ion sensing in aqueous environments due to their high dispersion in water, ultra-small size, and high surface area nature. We successfully synthesized Zn-MOF-74 nanodots for Fe^{3+} ion detection in aqueous solution. Figure 2.4a showed the UV-vis absorption spectrum of Zn-MOF-74 nanodots before and after addition of Fe^{3+} ion in aqueous solution. The UV-Vis spectrum of Zn-MOF-74 nanodots displayed an absorption peak at 352 nm, but a new absorption peak at 600 nm appeared immediately upon the addition of Fe^{3+} (Figure 2.4a). With the absorption peak shifted to red, the color of the solution also changed from transparency to blue (Figure 2.4b). Upon the addition of Fe^{3+} to the Zn-MOF-74 nanodots solution in an aqueous environment, the color and UV-visible absorption spectra of the solution rapidly and selectively changed,

indicating the potential application for colorimetric sensing of Fe^{3+} ions in aqueous solution.

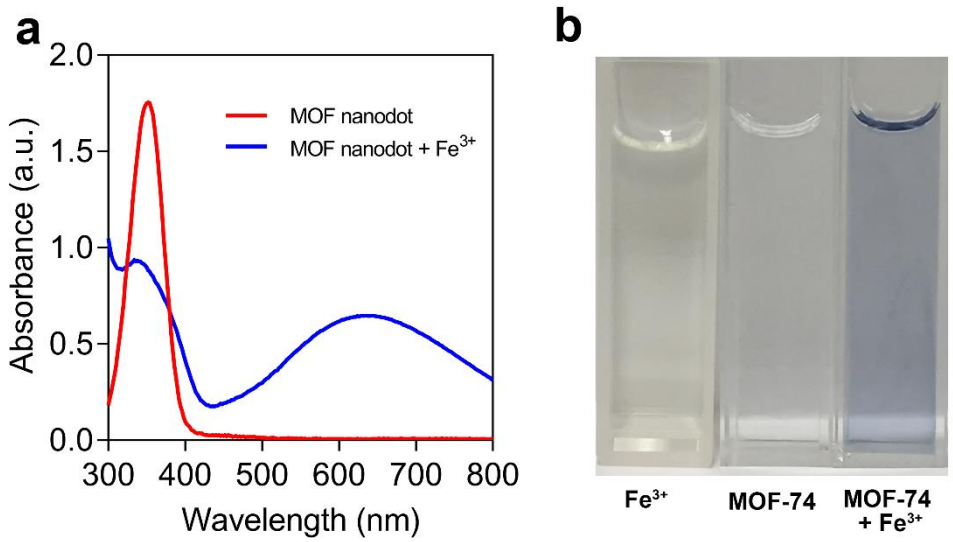

Figure 2.4 (a) UV-vis absorbance spectra of MOF nanodots and MOF nanodots with Fe^{3+}. (b) The color change of the MOF nanodots after the addition of Fe^{3+}.

The amplitude of UV-Vis spectra at 600 nm of Zn-MOF-74 nanodot solution exhibited a Fe^{3+} concentration-dependent increase shown in the Figure 2.5a. Moreover, the amplitude of the 600 nm absorption peak of Zn-MOF-74 nanodot solution mixed with Fe^{3+} showed a broad liner relationship with the Fe^{3+} concentration as high as 1750 μM (Figure 2.5b), higher than the previously reported sensors which are typically less than 500 μM of Fe^{3+}[81]. In addition, the limit of detection (LOD) of this Zn-MOF-74 nanodot based Fe^{3+} sensor which was calculated based on the control signal plus 3 times of standard deviation, reached 1.04 μM of Fe^{3+}, comparable with those of fluorescent-based sensing methods ranging from 0.45 μM to hundreds of micromoles (Table 1). This colorimetric detection can be realized with much simpler instrumentation and naked-eye recognition. Many sensors can only detect ions in a solution with a small range of pH. This Zn-MOF-74 sensing platform was also examined in aqueous solution with a broad range of pH. It was found that the Zn-MOF-74 nanodots based sensor has

good pH stability and capable of sensing the Fe^{3+} ion in both weak and base solution (Figure 2.5c).

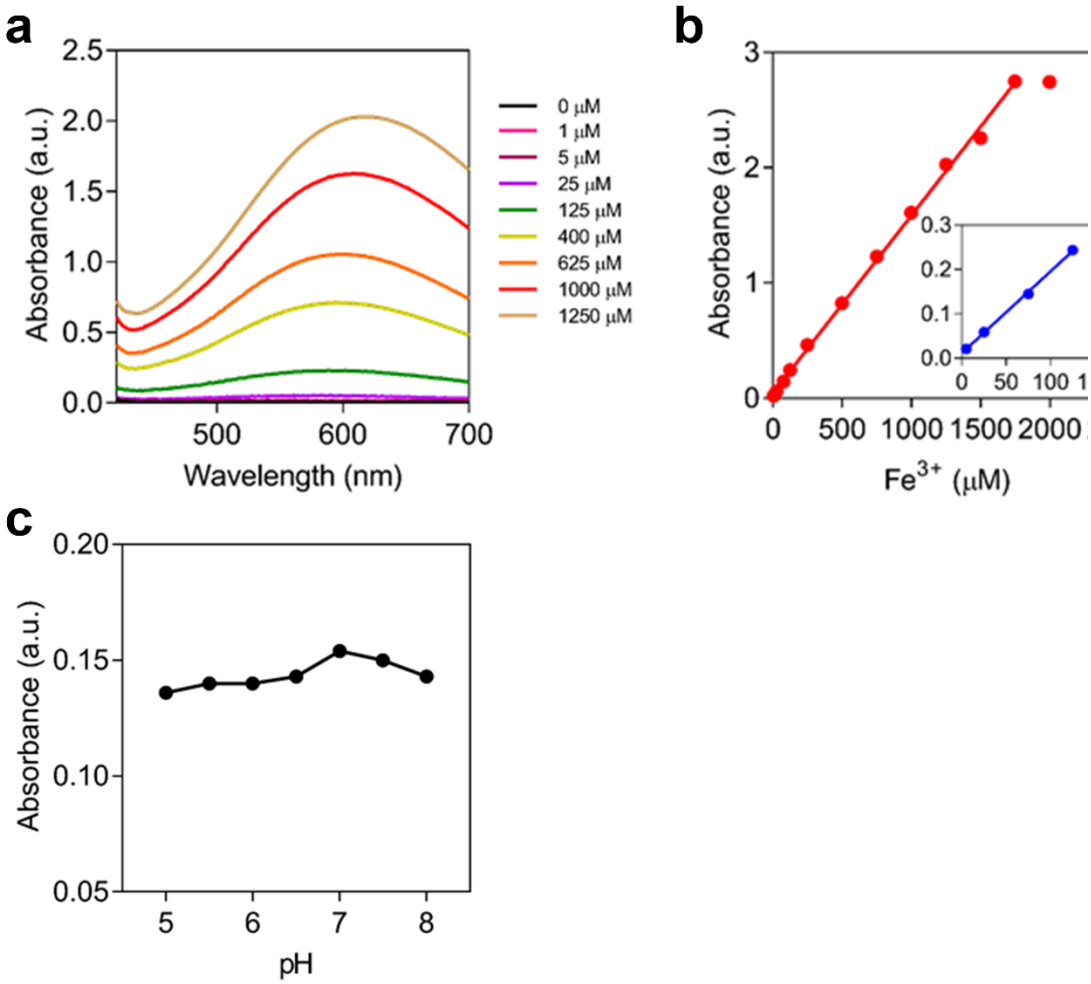

Figure 2.5 (a) UV-vis absorbance spectra of MOF nanodots with different amount of Fe^{3+} ions. (b) The fitting curve of the UV-vis absorbance of MOF nanodots versus Fe^{3+} concentration (linear range 1~1750 μM.

Table 1. Comparison of Fe^{3+} sensors based on various materials

Material	Technique	LOD (μM)	Linear detection range	Ref.
MIL-53 (Al)	Fluorescent	0.9	3~200 μM	15
Bis(rhodamine)	Fluorescent	50	150~237.5 μM	34
Graphene oxide	Fluorescent	0.64	N/A	35
[Tb(BTB)(DMF)]	Fluorescent	10	10~1000 μM	36
$Eu(C_{22}H_{14}O_2)_3$	Fluorescent	100	0.1~5 mM	31
$Eu(C_{33}H_{24}O_{12})(H_2NMe)(H_2O)$	Fluorescent	200	N/A	18
Salicylaldehyde-azine (SA)	Colorimetric	9.5	15.7~23.6 μM	37
Carbon Dots	Colorimetric	0.3	0.3~546 μM	38
Bis-rhodamine Urea	Colorimetric	4.3	30~70 μM	39
Our work	Colorimetric	1.04	1~1750 μM	

To examine the selectivity of the Fe^{3+} sensor, a variety of metal ions including Mg^{2+}, Ca^{2+}, Ni^{2+}, Co^{2+}, Cu^{2+}, Cd^{2+}, Mn^{2+}, Na^{+}, K^{+}, Fe^{2+}, Cr^{3+}, Al^{3+} and Fe^{3+} at concentration of 0.1 mM were added to the Zn-MOF-74 nanodots solution (1 mL, 50 μg mL^{-1}). The UV-vis absorption spectra of the mixed solution did not show obvious changes in the wavelength range between 420 and 800 nm for all the 12 metals ions with exception of Fe^{3+} which resulted in a significant increase in the region of 500 – 700 nm, with a peak at around 600 nm (Figure 2.6a). Figure 2.6b summarizes the amplitudes of characteristic 600 nm for all metal ions mixed with Zn-MOF-74 nanodots in water. Fe^{3+} induced the amplitude of characteristic absorbance at 600 nm was about seven folds higher than those induced by other metals. In addition, the color of Zn-MOF-74 nanodot changed to blue when adding the Fe^{3+}. In contrast, Zn-MOF-74 nanodot solution remained transparent with addition of other 12 metal ions. We further investigated reversibility of this color change process by adding free Zn^{2+} ion to the Fe^{3+}/Zn-MOF-74 solution. As shown in the UV-Vis spectra in Figure 2.6c, the

introduction of Zn^{2+} (0.1 mM) caused a slight shift of absorption peak of Fe-DOBDC but still exhibited a strong absorption peak around 580 – 600 nm. this result demonstrated that the Zn-MOF-74 nanodot based colorimetric sensing of Fe^{3+} was not reversible by adding free Zn^{2+}.

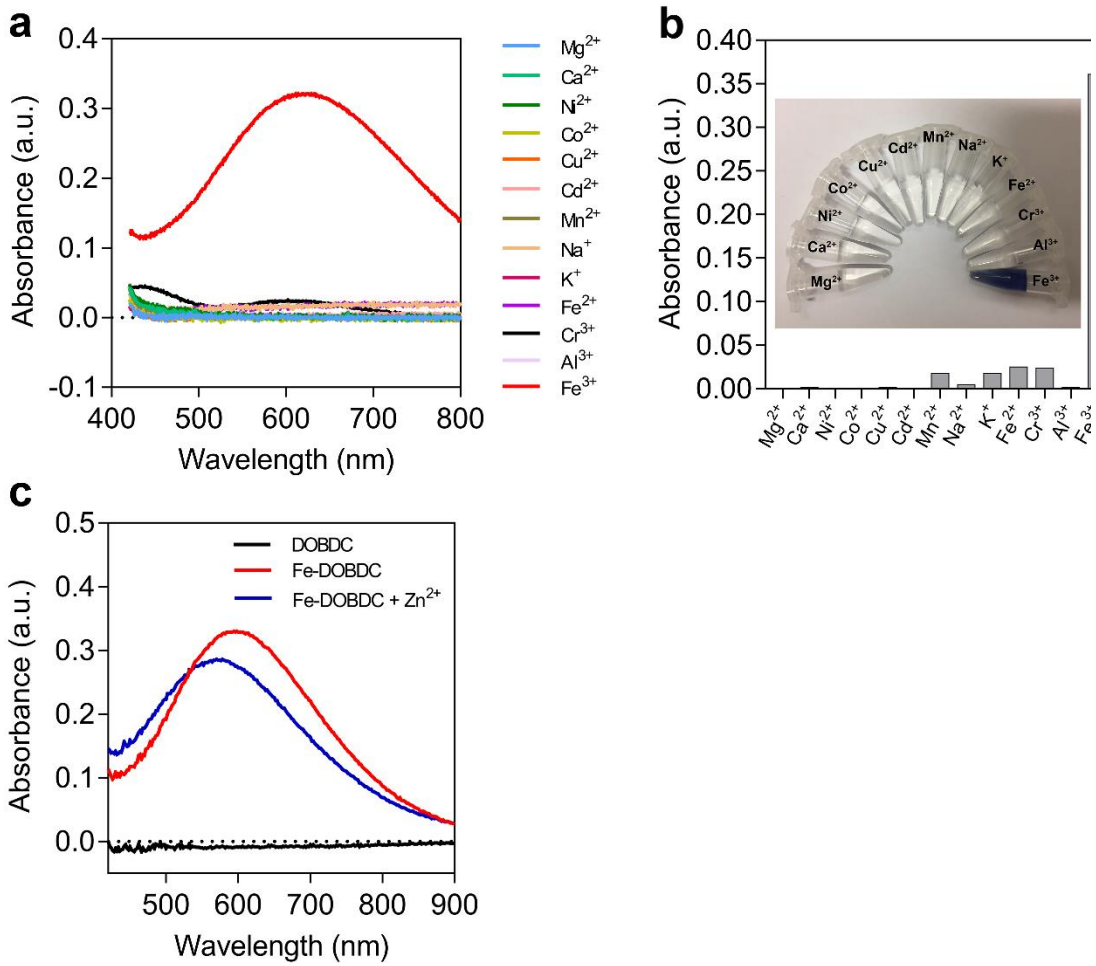

Figure 2.6 (a) UV-vis absorbance spectra of MOF nanodots with 50 μM of different metal ions. (b) Amplitude of characteristic 600 nm peak of MOF nanodots in UV-vis absorbance spectra with different metal ions. The inset shows the color change of MOF nanodots with metal ions in aqueous solution.

2.3.3 Exploration of Colorimetric Sensing Mechanism

As shown in Scheme 1, it is hypothesized that the addition of Fe^{3+} will lead to 1) the collapse of Zn-MOF-74 structure by the formation of Fe-DOBDC complex and release of free Zn^{2+} ions in solution; 2) the solution color changed from transparency to blue due to the generated Fe-DOBDC complex. To demonstrate the first hypothesis, powder XRD was firstly performed with solution of Zn-MOF-74 nanodots before and after

addition of Fe^{3+}. As shown in Figure 2.7a, powder XRD spectrum of addition of Fe^{3+} led to the disappearance of the characteristic peaks of Zn-MOF-74 at ~6.8° and ~11.6° compared with that of original curve, indicating the collapse of the MOF structure upon the addition of Fe^{3+}. Moreover, we also observed that the characteristic peaks in powder XRD pattern gradually disappeared with the increasing amount of Fe^{3+} up to 50 mM, which demonstrated the gradual disruption of the metal-organic framework by Fe^{3+} (Figure 2.8a). Other metal ions did not show any change in XRD patterns, indicating no disruption of MOF structure (Figure 2.8b). FTIR was also employed to investigate the formation of Fe-DOBDC complex. A new FTIR peak at 578 cm^{-1} was observed after the addition of Fe^{3+} to the Zn-MOF-74 nanodots, indicating the formation of Fe-O bond due to the coordination of Fe^{3+} with hydroxyl groups on the DOBDC. As both hydroxyl and carboxyl groups were coordinated with Zn atoms in the framework structure, the high affinity between exotic Fe^{3+} and phenolic hydroxyl groups might cause the detachment of ligands from Zn^{2+} atoms and form an iron (III)-phenol salt complex: Fe-DOBDC[82].

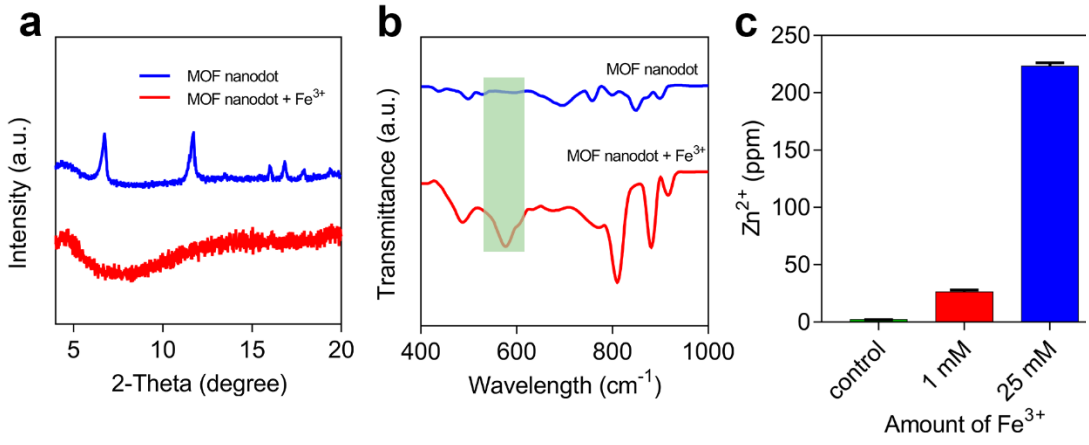

Figure 2.7 Powder XRD pattern (a) and FT-IR spectra (b) of MOF nanodots with/without 25 mM of Fe^{3+}. (c) Free Zn ions in the MOF nanodots solution after the addition of different amount of Fe^{3+} measured by ICP-OES.

XPS was also used to examine the reaction between Fe^{3+} and DOBDC and formation of Fe-DOBDC complex. A shift of Fe2p peak in the XPS spectra from 711.3

eV to 712.1 eV was observed after addition of Fe^{3+} in Zn-MOF-74 nanodots solution (Figure 2.9a). The slight increase of binding energy of Fe2p is due to the formation of Fe-O bond in Fe-DOBDC complex. To verify this hypothesis of release of free Zn^{2+} upon addition of Fe^{3+}, inductively coupled plasma optical emission spectrometry (ICP-OES) was used to analyze the concentration of released Zn element in the supernate of MOF nanodot solution after the addition of Fe^{3+}. The ICP results showed a significant increase of free Zn element from 26.3 to 223.2 ppm when the amount of Fe^{3+} increased from 1 mM to 25 mM (Figure 6c). The above results confirmed our first hypothesis that the structure of metal-organic framework was collapsed with the addition of Fe^{3+} due to the formation of Fe-DOBDC complex and release of free Zn^{2+} ions in solution in aqueous environment.

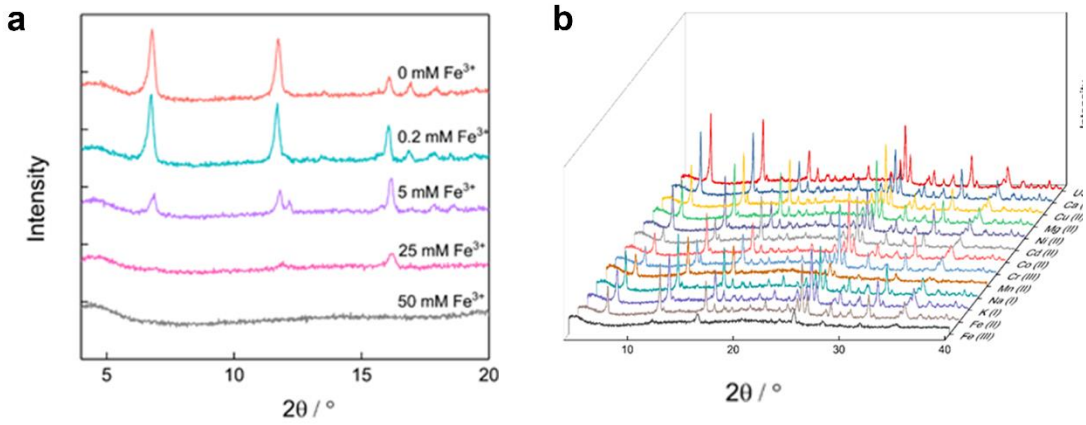

Figure 2.8 (a) Powder XRD pattern of MOF nanodots after treatment with different amount of Fe^{3+} solution for 2 h. (b) Comparison of powder XRD patterns of MOF nanodots with addition of 25 mM of various ions (Mg^{2+}, Ca^{2+}, Ni^{2+}, Co^{2+}, Cu^{2+}, Cd^{2+}, Mn^{2+}, Na^{+}, K^{+}, Fe^{2+}, and Fe^{3+}).

We proposed a hypothesis that the absorbance peak in the region of 500 – 800 nm was due to the newly formed Fe-DOBDC complex. The disruption process of Zn-MOF-74 structure and the formation of Fe-DOBDC complex can be expressed as the following Equation 1.

$$Fe^{3+} + [Zn_2DOBDC]_{MOF} \rightarrow [Fe - DOBDC]_{complex} + Zn^{2+} \qquad (1)$$

When the carboxylate-based linkers such as DOBDC coordinated with nodes that are relatively soft Lewis acidic species such as Zn^{2+}, the weak coordinating bond makes framework less resistant to the attack of reactive chemicals[83]. The strong affinity between Fe^{3+} and DOBDC ligand leads to the disruption of Zn-MOF-74 structure, followed by the formation of Fe-DOBDC complex and the release of free Zn ions. The material components in the Zn-MOF-74 nanodot solution after addition of Fe^{3+} possibly include the residual Zn-MOF-74 nanodot, Fe^{3+} ion, Fe-DOBDC complex and free Zn^{2+}. Figure 2.9b shows the UV-Vis absorption spectra for solutions of Zn-MOF-74 nanodot, Fe^{3+} ion, Fe-DOBDC complex and Zn^{2+} ion. It is clearly observed that only Fe-DOBDC complex showed a significant peak around 600 nm. Other material components such as Fe^{3+} ion, Zn-MOF-74 nanodot and Zn^{2+} ion did not show obvious peaks in the visible color range of 420 – 800 nm. Correspondently, the tube with Fe-DOBDC shows blue color and those with Fe^{3+} ion, Zn-MOF-74 nanodot and Zn^{2+} ion show transparency (Figure 2.9b inset). The above results demonstrated our hypothesis that the solution color change from transparency to blue was due to the generated Fe-DOBDC complex. Based on the above experiments and results, we could conclude that the change of color and absorbance of Zn-MOF-74 nanodot upon the addition of Fe^{3+} is attributed to the ligand dissociation from MOF and phenolic iron complex produced by the interaction between ligand and Fe^{3+}.

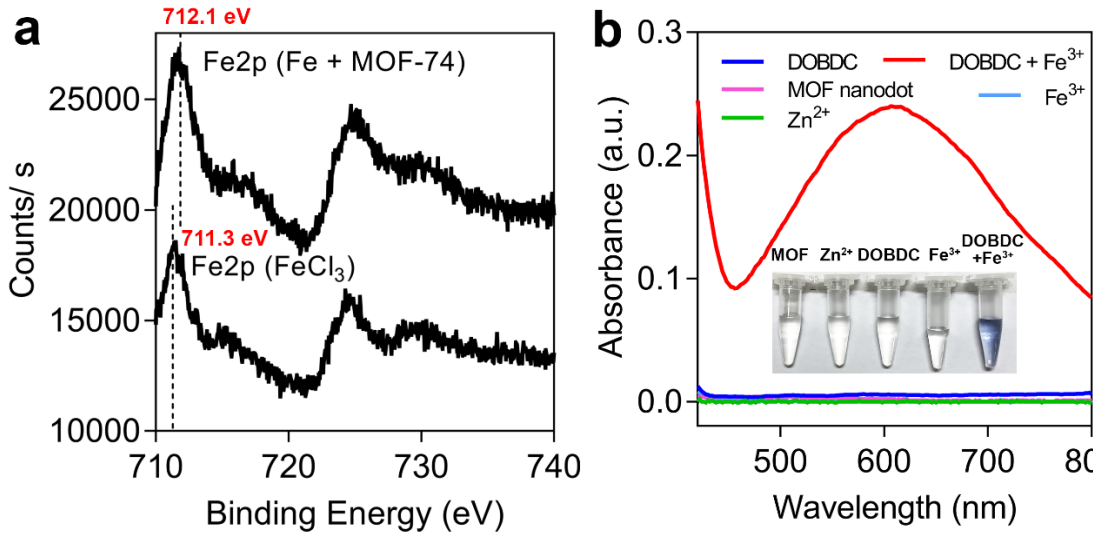

Figure 2.9 (a) XPS spectra of Fe2p peak shift from 711.3 eV to 712.1 eV due to the formation of Fe-O bond of Fe-DOBDC. (b) UV-Vis spectra of possible material components in the solution of disrupted Zn-MOF-74 nanodots with addition of Fe^{3+} (Fe-DOBDC, DOBDC, Zn-MOF-74, Zn^{2+} and Fe^{3+}).

2.4 Discussion

We have synthesized ultrasmall Zn-MOF-74 nanodots with size around 4 nm and demonstrated a novel Zn-MOF-74 nanodots based platform for Fe^{3+} colorimetric sensing. We are able to control the size of Zn-MOF-74 nanocrystals within sub-10 nm through manipulating the initial conditions with a diluted material system under room temperature. The ultrasmall Zn-MOF-74 nanodots used for Fe^{3+} sensor have several advantages compared to other MOF based ion sensors: 1) Zn-MOF-74 nanodots are highly stable in aqueous solution Zn-MOF-74 nanodots while other MOFs usually have poor dispersity in water thus cannot detect ions in aqueous solution. 2) Due to the ultrasmall size nature, the Zn-MOF-74 nanodots have high surface area and enormous reactive sites, leading to a high sensitivity and fast response compared to those of bulk materials. 3) The colorimetric sensing of Fe^{3+} using Zn-MOF-74 nanodots is much simpler than other fluorescence-based sensor as it can simply recognize by naked-eyes. Based on the investigation on mechanism using through several techniques including ICP-MS, FTIR, UV-vis absorbance, we are able to demonstrate that the selective Fe^{3+} sensing mechanism is dependent on selective framework structure collapse and the

formation of Fe-DOBDC complex with blue color. The highly dispersive and ultrasmall size may provide other possibilities for Fe^{3+} sensing in the biological systems. The Zn-MOF-74 nanodots platform greatly simplified the setup for Fe^{3+} sensing as well as accelerating the detecting process within a few seconds. Such a platform may open a new era for ultrasmall nanodots-based ion sensing.

3 MOF PCN-224 Nanoparticle for Photo-inhibition of Amyloid-β Aggregation

The original work described in this chapter was published (Wang et al. ACS Appl. Mater. Interfaces 2018).

3.1 Introduction

Alzheimer's disease, the most common form of dementia, is an unremitting neurodegenerative disorder that causes progressive impairment of the patient's cognitive and memory ability. AD affects more than 30 million people worldwide today and 106 millions of people is estimated to suffer the disease by 2050[84]. It is believed that two biomarkers – amyloid-β (Aβ) and tau in the cerebrospinal fluid (CSF) are two causes of AD. Of which, the abnormal accumulation of Aβ monomers into neurotoxic β-sheet-rich oligomers and fibrils has been considered as the key pathogenic event of AD and thus has attracted the most attention by far. Consistent with this view, Aβ oligomers can: 1) directly induce synaptic dysfunction and neuronal death, both which are responsible for AD initiation and progression; and 2) trigger events such as oxidative damage and inflammation, which contribute to the progression of AD. Numerous studies have supported the idea that Aβ peptides – the seeds of AD – are present in human brain at birth, and these neurotoxic peptides are continuously produced throughout life. Therefore, the most direct target in anti-Aβ therapy is the inhibition of Aβ production and accumulation. Tremendous efforts have been expended on the discovery of inhibitors against Aβ aggregation over the past decades. β- and γ-secretase inhibitors were considered as effective means of treating AD, but few novel chemical compounds based on this strategy have reached clinical trials due to inevitable side effects. Despite the use of small-molecule γ-secretase modulators is receiving increasing attention as a promising therapeutic approach, these modulators have been abandoned as potential targets by many pharmaceutical companies. Recent studies have revealed that the oxygenated form of Aβ has low aggregation potency and attenuated

toxicity under physiological conditions[85]. Several photocatalysts have been identified to inhibit Aβ aggregation under light irradiation. Taniguchi and co-workers designed three photocatalysts by combining the sensing function of an amyloid fluorescent probe and photooxygenation function of flavin-based catalysts. The photooxygenation catalysts can selectively bind to the Aβ peptides and oxygenate the Aβ under light irradiation. The oxygenated Aβ is not likely to form higher-order aggregates thus remain less toxic in physiological environment[86].

With the rapid development of nanomaterials in recent years, numerous nanomaterials have been used in biomedical applications. More recently, many therapeutic strategies based on nanomaterials have been discovered to inhibit the process of monomeric Aβ peptide aggregation and disaggregate the toxic Aβ oligomers and fibrils, thus attenuate the neuron toxicity. For example, Chung et al used carbon nanodot as a photosensitizer to inhibit the self-assembly of Aβ peptide and to disassemble the preformed Aβ aggregates[87]. Lee et al used photoactivated meso-tetra(4-sul-fonatophenyl)porphyrin (TPPS) to inhibit the Aβ aggregation *in vitro*[88]. However, these strategies have inherent limitations. For example, both carbon nanodot and TPPS were photoactivated only by blue light (around 360 nm) which has poor penetration thus is not suitable for *in vivo* studies. Besides, TPPS is a small non-targeting organic molecule, which may have potential risk to many normal tissues in brain and other parts of body. A few other typical photosensitizers such as Methylene blue (MB)[89] and rose bengal (RB)[90] have also been used to prevent Aβ peptide from aggregating but suffer from similar potential problems as above. Upconversion nanoparticles (UCNP) have also been developed to treat Aβ peptide by using a 980 nm NIR laser[91]. This approach enjoys a deep penetration to body but requires complicated and costly NIR laser system, makes it difficult to be extensively applied.

Metal-organic framework (MOF), a term describes a class of hybrid materials formed by self-assembly of metal ions or clusters and organic bridging ligands, has been attracting growing interest among biologists and chemists[92-93]. As a large number of metals and organic molecules can be coordinated to each other to form such kind of framework structures with diverse properties, researchers have developed different families of MOFs and applied them to various applications such as catalysis, sensing, gas storage and separation, optical imaging, drug delivery, *etc*[94]. In this study, we developed a novel approach for near infrared (NIR) light-induced inhibition of the Aβ aggregation based on a porphyrin PCN-224 nanoparticles. Due to the existence of porphyrin ligand tetrakis(4-carboxyphenyl)porphyrin (TCPP) in the framework, PCN-224 not only inherits the advantages of porphyrin molecules such as red fluorescence emission and ability of generating singlet oxygen, but also has an ultra-stable periodic nanostructure which is able to work in acidic and alkaline solutions. Moreover, this PCN-224 integrates photosensitizers in periodic arrays, significantly reducing quenching of excited energy in a minimal volume, while allowing the accessibility of substrates due to their porous features. The delivery of light to the brain tissue is always an obstacle for the phototherapy of neurodegenerative disorders. PCN-224 can solve this issue as it oxygenates the Aβ peptide through absorbing NIR light, which may help facilitate the delivery of light to the target brain area without reducing much power intensity. We expect this study provides new opportunities for the application of functional MOFs and NIR phototherapy to the treatment of neurodegenerative diseases.

3.2 Methodology

3.2.1 Materials and Reagents

Aβ42 peptide was purchased from GL Biochem Ltd. (Shanghai, China). Thioflavin T (ThT) (~75%), Hexafluoro-2-propanol (HFIP) were purchased from Tokyo Chemical

Industry Co., Ltd., dimethyl sulfoxide (DMSO, anhydrous, >99.9%), N, N'-dimethylformamide (DMF, anhydrous, 99.8%) were purchased from J&K (China). Ultrapure water and HEPES buffer (pH 7.4) were purchased from Life Technology (USA). The native gel electrophoresis-related reagents and kits were from Bio-Rad (USA). All other reagents were purchased from Sigma-Aldrich (USA).

3.2.2 Methods

3.2.2.1 Synthesis and characterization of PCN-224 nanoparticles

PCN-224 nanoparticles were prepared according to previous method with slight modifications[95]. Briefly, 10 mg of 5, 10, 15, 20-tetrakis (4-carboxyphenyl)porphyrin (TCPP), 30 mg of zirconyl chloride octahydrate ($ZrOCl_2 \cdot 8H_2O$), 220 mg of benzoic acid (BA) were dissolved in 10 mL of DMF in a 25 mL round-bottom flask and the mixture was heated in oil bath at 90 °C for 5 h under 300 rpm stirring. The PCN-224 nanoparticles were obtained by centrifugation (21120 g, 30 min) and wash for three times with DMF and ethanol. The final particles were freeze dried to powder for storage. The transmission electron microscope (TEM) images were collected in a JEOL JEM-2100 F microscope. Scanning electron microscope (SEM) images were obtained in a JEOL Field Emission SEM microscope. Zeta potential and DLS of the PCN-224 were measured using Malvern ZEN 3600 Zetasizer instrument. Ultraviolet-visible (UV-vis) absorbance were measured by Ultrospec 2100 Pro spectrophotometer (Amersham Biosciences). Powder X-ray diffraction (PXRD) patterns were collected at 293 K on a Rigaku SmartLab diffractometer using Cu/Kα radiation. Thermogravimetric analysis (TGA) was performed at a heating rate of 10 °C min^{-1} under N_2 flow using a Mettler Toledo TGA/DSC3+ instrument. The Fourier transform infrared (FT-IR) spectra were measured in KBr pellets on the Bruker Vertex-70 IR Spectroscopy in the wavelength

region of 400 – 4000 cm^{-1}. BET surface area was measured on a Micromeritics ASAP 2420 Analyzer.

3.2.2.2 Preparation of Aβ42 monomer and study of photo-induced inhibition of Aβ42 aggregation

Human Aβ42 (1 mg) was dissolved in HFIP and was kept at room temperature for 2 h. The HFIP was then removed under a gentle flow of nitrogen gas followed by freeze drying for 3 h. The obtained film-like peptide was dissolved in 30 µL of DMSO and then diluted to 300 µM with ultrapure water (Invitrogen) for further use. The Aβ42 oligomers and fibrils were prepared by diluting the peptide in HEPES buffer (20 µM, pH 7.4, 150 µM NaCl) to a final concentration of 25 µM and incubating at 37 °C for 24 h. For inhibition studies, PCN-224 nanoparticles were added to Aβ42 solution (25 µM) to form a final concentration of 100 µg mL^{-1}. The solution was shone with a 650 nm light (30 mW cm^{-2}) for 30 min and incubated at 37 °C for 24 h.

3.2.2.3 Characterization of Aβ42 after treatment of nanoprobe under light irradiation

ThT stock solution was prepared by dissolving 0.32 mg of ThT in 10 mL of ultrapure water and filtering it through a 0.22 µm PES syringe filter. 100 µL of solution containing 10 µM of ThT, 15 µM of Aβ42 peptide was subjected to fluorescence spectrometer. The fluorescence was recorded using an excitation wavelength of 440 nm and an emission wavelength of 485 nm. All samples were run in triplicate. At least three independent experiments were carried out for each assay.

Far-UV circular dichroism (CD) spectra of Aβ42 peptide solution incubated without or with PCN-224 were recorded in a JASCO J-810 Spectrometer (JASCO Co., Tokyo, Japan), using a quartz cuvette with 1 mm path length. 15 µM of Aβ42 peptide without or with PCN-224 and light treatment were incubated at 37 °C for 24 h before

subjected to the measurement. The CD spectrum was scanned three times in the range of 190 – 250 nm.

Atomic force microscope (AFM) analysis was conducted by dropping 5 μL of each Aβ42 sample on a freshly cleaved silicon wafer (pretreated by Piranha solution). The Aβ42 samples were gently washed by 3 drops of ultrapure water. The wafer surface was blow-dried under a gentle flow of nitrogen gas. AFM images were collected on a Bruker Catalyst microscope using tapping mode. Transmission electron microscope (TEM) analysis was conducted by loading 5 μL of each Aβ42 sample on 300 mesh formvar/carbon coated grid. The grids were washed at least three times and dried at room temperature before measurement. The transmission electron microscope images were collected in a JEOL JEM-2100 F microscope (University Research Facility in Materials Characterization and Device Fabrication, The Hong Kong Polytechnic University).

To do native gel electrophoresis analysis, incubated Aβ42 samples were mixed with sample buffer and loaded to a 10% precast gel (SDS free, Bio-Rad) and run in a Mini-PROTEAN® Tetra Cell (Bio-Rad) using a current of 20 mA for 50 min. Silver staining was performed using a silver staining kit (Bio-Rad) according to the manufacturer's instructions. The gel was then imaged in a ChemiDoc Touch Imaging System (Bio-Rad).

The size distribution of incubated Aβ42 peptide (25 μM) treated with or without PCN-224 was measured using a light scattering spectrometer (Zetasizer Nano ZS instrument; Malvern Instruments, Worcestershire, UK). The Aβ samples were centrifuged at 16000 g for 30 min at 4 °C and the supernatant was measured by DLS at 25°C. Each scan consisted of 11 runs and each sample was measured at least three times.

3.2.2.4 Singlet oxygen detection

Singlet oxygen detection of photo-activated PCN-224 nanoparticles was carried out using two ROS indicators 1,3- diphenylisobenzofuran (DPBF), and 2′,7′-dichlorodihydrofluorescein diacetate (DCF-DA). A DMF solution containing 4 μg mL^{-1} of PCN-224 and 0.04 μM of DPBF was illuminated under a wavelength of 650 nm light at an intensity of 30 mW cm^{-2} for 0 to 30 min. The absorbance intensity was recorded every 5 min. DCF-DA was also used as a capture agent for the ROS detection of PCN-224. DMSO solution containing DCFH-DA (10×10^{-6} M) and PCN-224 nanoparticles (4 μg mL^{-1}) in a quartz cuvette was illuminated by a Xenon lamp (650 nm, 30 mW cm^{-2}) for 30 min. The fluorescence intensity was recorded every 5 min in a fluorescence spectrometer (excitation wavelength, 488 nm; emission range, 520 – 600 nm).

3.2.2.5 DNPH assay

DNPH assay was carried out according to the protocol reported by previous studies. Briefly, 480 μL of Aβ42 solution (40 mM) was mixed with trichloroacetic acid (TCA, final concentration 20%) and kept in an ice bath for 10 min. The solution was then transferred to an Eppendorf tube and centrifuged at 14,000 rpm for 4 min, and the resulting pellet was collected. 500 μL of DNPH (10 mM) in 2 M HCl was added to the solution for 1 h at room temperature. The sample was then precipitated again with a 20% TCA solution and washed at least three times with 1 mL of an ethanol-ethyl acetate (1:1, v/v) solution before treated with a guanidine hydrochloride solution (6 M, pH 2.3) for 15 min at 37 °C. The absorbance of the above sample was measured by a Ultrospec 2100 Pro spectrophotometer in the wavelength range of 300 – 600 nm.

3.2.2.6 Cell viability assay

PC12 cells were used for the cell viability assay. PC12 cells were cultured in medium containing 15% HS, 2.5% FBS, and 1% antibiotics, under 5% of CO_2 atmosphere at

37 °C. For biocompatibility test, 1.6×10^{-5} cells mL^{-1} were seeded into 96 well plates and incubated for 24 h. PCN-224 nanoparticles were then added to the 96 well plate at different concentrations and incubated for 24 h before subjected to the MTT assay. For the photo-inhibition test, non-treated, light-treated, PCN-224-treated, and PCN-224 with light illumination treated Aβ42 peptide were added to the PC12 cells in a 96 well plate and incubated for 24 h.

3.3 Results

PCN-224 nanoparticles were prepared through a solvent thermal method in a diluted material system and characterized using various techniques. PCN-224 is consisted of two major components – Zr and TCPP which are coordinated through covalent bonding, forming a stable crystalline framework structure (Figure 3.1a). Zr is known for its good biocompatibility and high valence to link with bridging ligands to form ultrastable Zr-MOF structure[95]. When photosensitizer molecule TCPP as an organic ligand is embedded into the PCN-224 structure, the generated porphyrin MOF nanoparticle would have high light-to-oxygen conversion efficiency because of the high density of TCPP ligands in the framework and easy diffusion of molecular oxygen through the porous structure. Moreover, the nanosized MOF structures are preferred for potential brain delivery to across blood-brain barrier (BBB). It has been demonstrated that particles within 100 nm had higher BBB permeability than the bigger ones. However, downsizing MOF to nanoscale is always challenging because it is easy to form undesired phases during crystallization. Here, Zr-based MOF PCN-224 was solvent-thermally synthesized in a diluted system aiming at creating more MOF monomers, which would result in smaller nanoparticles. Transmission electronic microscopy (TEM) image in Figure 3.1b showed that the synthesized PCN-224 nanoparticles had round-shaped morphology. Field Emission Scanning Electron Microscopy (FESEM) images

were also taken to analyze the size distribution of PCN-224 nanoparticles (Figure 3.2a), which showed an average size around 70 nm (Figure 3.1c). Dynamic light scattering (DLS) was also used to measure the size of PCN-224 nanoparticles in water which is slightly larger than the results of SEM image (Figure 3.2b). The UV-visible light absorption spectra of PCN-224 nanoparticles showed a major absorption peak at 425 nm (Figure 3.1d) and four other peaks in the Q band between 500 nm and 700 nm (Inset diagram of Figure 3.1d). The absorption peak at 650 nm of PCN-224 nanoparticle allowed the nanoprobe to be used for NIR activated photooxygenation. The photoluminescence (PL) spectra of PCN-224 nanoparticles showed an emission peak at 680 nm under excitation wavelength of 440 nm, which demonstrated the red fluorescence which is possible for the application of cell imaging labels (Figure 3.1e).

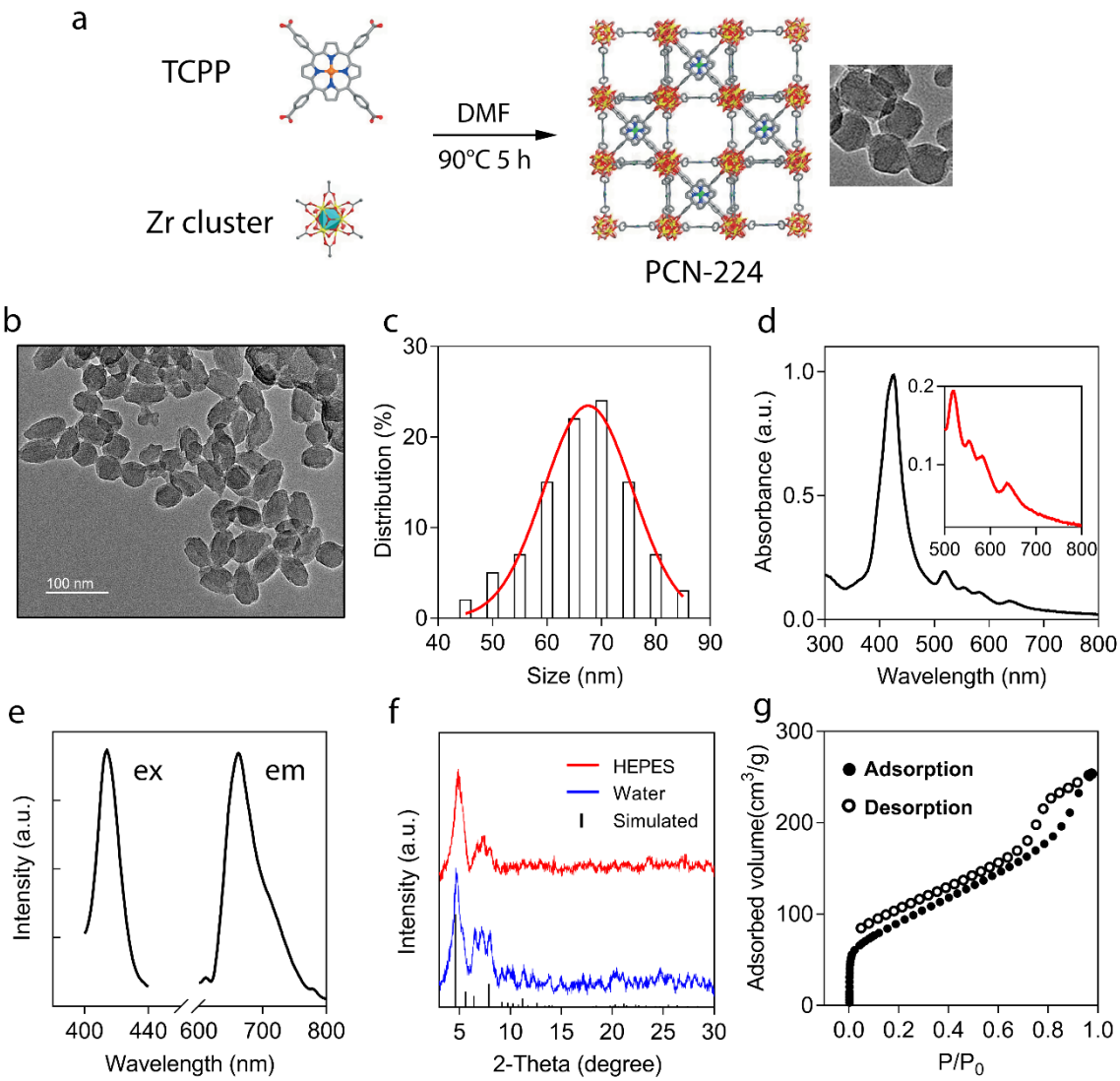

Figure 3.1 Characterizations of PCN-224 nanoparticles. (a) schematic illustration of the synthesis of PCN-224 nanoparticles. (b) TEM image of PCN-224 nanoparticles. (c) Size distribution of PCN-224 nanoparticles by TEM. (d) UV-vis absorbance spectra of PCN-224 nanoparticles and the enlarged region of 500-800 nm in the inset figure. (e) Excitation and emission spectra of PCN-224 nanoparticle. PCN-224 nanoparticle has a highest excitation wavelength at 414 nm (left curve) and an emission peak at wavelength of 650 nm. (f) Powder XRD of PCN-224 nanoparticles. (g) N_2 adsorption/desorption isotherms of the PCN-224 nanoparticles.

PCN-224 nanoparticles we further characterized by zeta potential measurement, powder X-ray diffraction (PXRD), thermogravimetric analysis (TGA), Fourier-transform infrared spectroscopy (FTIR) and Brunauer-Emmett-Teller (BET) analysis. PCN-224 nanoparticles showed good dispersibility in water and HEPES buffer after 7 days standing (Figure 3.2c). Zeta potential of PCN-224 nanoparticle was around 25.8 mV in water and -24.5 mV in HEPES buffer at pH 7, which explained its good dispersibility in water and HEPES buffer (Figure 3.2d). The powder X-ray diffraction

(PXRD) was used to further determine the crystallinity of PCN-224 nanoparticle. PXRD pattern of as-synthesized PCN-224 registered with 2θ steps of 0.02° was well agreed with the simulated curve in Figure 3.1f, suggesting good crystallinity in aqueous solution. Notably, PXRD curve of PCN-224 nanoparticle maintained unchanged in HEPES buffer (20 μM, pH 7.4) comparing to those in water, indicating that PCN-224 retained good stability and crystallinity in HEPES buffer for 24 h. The as-synthesized PCN-224 nanoparticles were also analyzed by TGA (Figure 3.2e). The first step of weight loss of 23% in the region of 50-240 °C was due to the removal of adsorbed water and organic solvent inside the PCN-224 pores. The second step of weight loss occurred between 400 °C and 580 °C, which was attributed to the loss of organic ligands. FTIR spectra in Figure 3.2f indicated the presence of O-H bond at around 1440 cm^{-1} and C=O bond at 1690 cm^{-1}. The peak at 650 cm^{-1} could be assigned to Zr-OH bond. The surface area of PCN-224 nanoparticles was determined by N_2 adsorption/desorption at 77 K using a dynamic BET method. The BET surface area was measured 326.34 m^2g^{-1}, showing good porosity of PCN-224 MOF structure. PCN-224 exhibited an excellent photostability under laser illumination at 650 nm with a power density of 0.5 W cm^{-2} for 30 min, where no obvious change could be observed in UV-vis absorption spectra (Figure 3.3a).

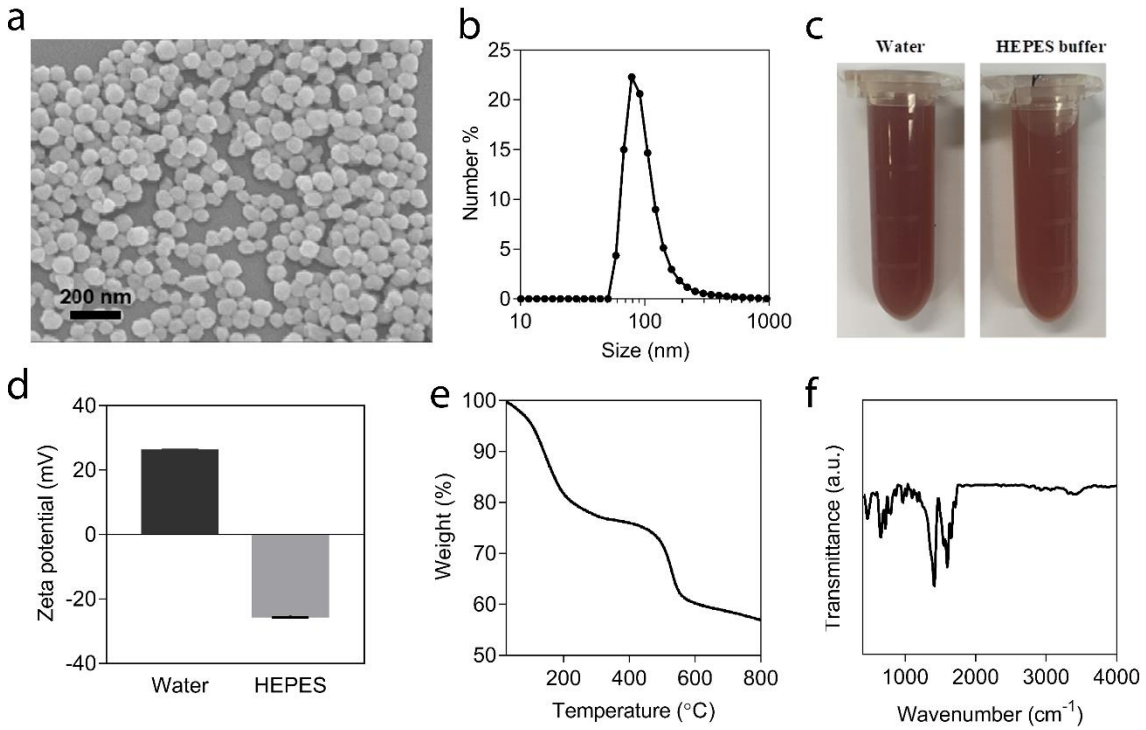

Figure 3.2 (a) FESEM images of PCN-224 nanoparticles. (b) DLS size of PCN-224 nanoparticles. (c) Photographs of PCN-224 nanoparticles dispersed in water and HEPES buffer after 7 days standing. (d) Zeta potential of PCN-224 nanoparticles in different buffer conditions. (e) TGA analysis of PCN-224 nanoparticles. (f) FT-IR of spectrum of PCN-224 nanoparticles.

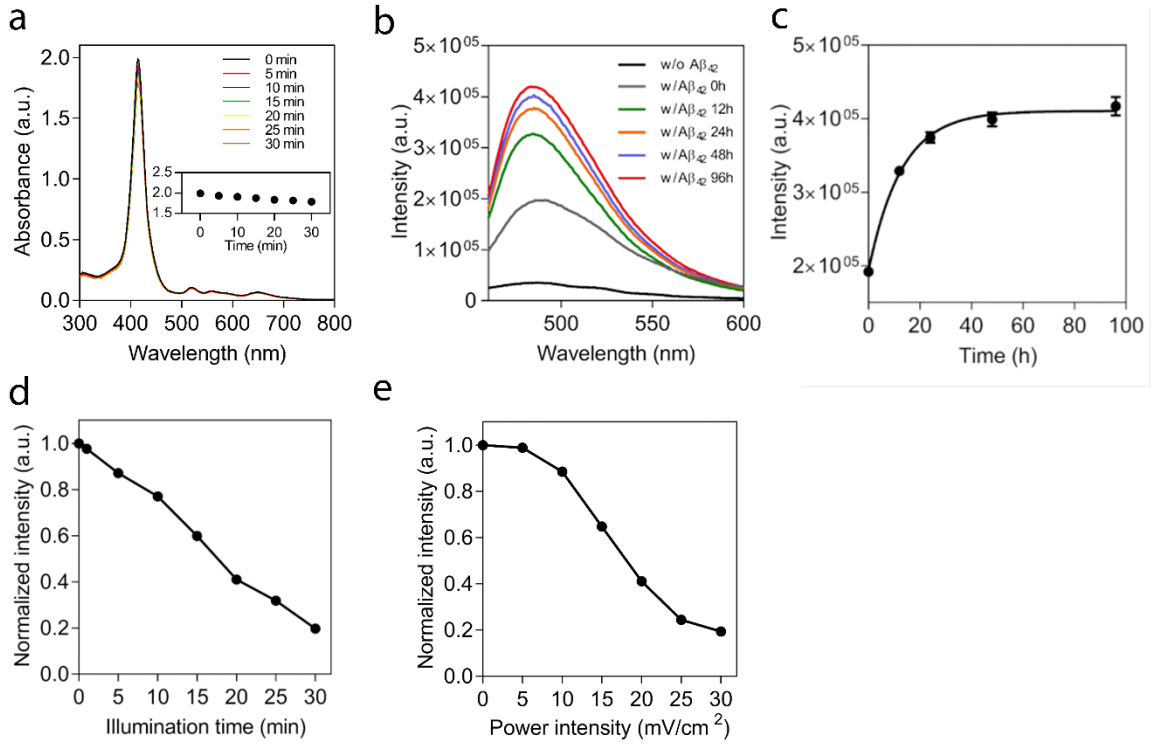

Figure 3.3 (a) Photostability of PCN-224 nanoparticles was examined by illuminating the nanoparticles with a 650 nm light for 0-30 min. The inset figure shows the absorbance value of PCN-224 at wavelength of 414 nm after different time of light illumination. (b, c) Self-assembly kinetics of Aβ42 peptide in ThT assay. Aβ42 monomers tended to self-aggregate at 37°C to form oligomeric and fibrillary structures with rich β-sheets. (d) Effect of illumination time on the inhibition of Aβ aggregation. (e) Effect of Power intensity on the inhibition of Aβ aggregation.

We investigated the photo-induced inhibitory effect of PCN-224 nanoparticles on the aggregation of Aβ42 peptide under a CEL-500 Xenon lamp with a 650 nm filter. ThT assay was used to monitor the aggregation degree of Aβ42 peptide. ThT is an organic dye that specifically binds to the β-sheets in the amyloids showing a significant fluorescence increase at the wavelength of 485 nm. The aggregation process of monomeric Aβ42 peptide was monitored by ThT assay in a variety of conditions at 37 °C up to 96 h. As shown in Figure 3.3b and 3.3c, the ThT fluorescence intensities increased to maximum after 24 h incubation in all conditions. The steady increase of ThT fluorescence intensity at 485 nm in dark environment without nanoparticles indicated the self-assembly aggregation of monomeric Aβ42 peptide. When Aβ42 peptide treated with PCN-224 nanoparticle alone or light irradiation alone, the ThT fluorescence intensity versus time curves were almost identical to that obtained in the dark environment, which indicated that light irradiation on Aβ42 alone or incubation with nanoparticles alone could not affect the aggregation of Aβ42 peptide (Figure 3.4a). There were no significant differences in ThT fluorescence after 96 h incubation in the presence of only nanoparticles, only light or dark environment without nanoparticles (Figure 3.4b). However, the ThT fluorescence intensity remained low when monomeric Aβ42 peptide solution was mixed with PCN-224 nanoparticles and exposed under 650 nm light illumination, indicating that the photoactivated PCN-224 nanoparticles could effectively inhibit the aggregation of Aβ42 into high order β-sheet-rich structures. Moreover, a concentration-dependent photo-inhibition by photo-activated PCN-224 nanoparticles was observed in Figure 3.4c. Considering that illumination is necessary for PCN-224 nanoparticles to inhibit Aβ42 self-assembly, the effect of NIR light illumination time and power density of NIR light on Aβ42 aggregation inhibition were examined. Not surprisingly, ThT fluorescence intensity at 485 nm decreased

accordingly with the increase of illumination time and power density of light (Figure 3.3d and 3.3e). To investigate the photo-inhibitory effect of PCN-224 nanoparticles on Aβ42 aggregation, CD was further employed in the study. As shown in Figure 3.4d, CD spectra of Aβ42 incubated without PCN-224 nanoparticles under dark environment exhibited a characteristic positive peak and a characteristic negative peak at 195 nm and 215 nm, respectively. This result indicated the transition of Aβ42 secondary structure from random coil to β-sheet-rich structure. With PCN-224 nanoparticle alone or light irradiation alone, there was neglectable change in the CD spectra. However, the characteristic CD peaks completely disappeared in the presence of PCN-224 nanoparticles under 650 nm light illumination. The results here demonstrated that photosensitized PCN-224 nanoparticles could efficiently inhibit the formation of Aβ42 oligomers and fibrils. In addition, the morphology of aggregated and non-aggregated Aβ42 peptide was directly observed under AFM. Figure 3.4e showed the formation of dense networks of Aβ fibrils after 24 h incubation of Aβ42 peptide without PCN-224 nanoparticles under dark environment. In the presence of PCN-224 nanoparticles under 650 nm light illumination, no obvious formation of Aβ fibrils was observed according to Figure 3.4f, demonstrating the capability of PCN-224 on the inhibition of Aβ aggregation.

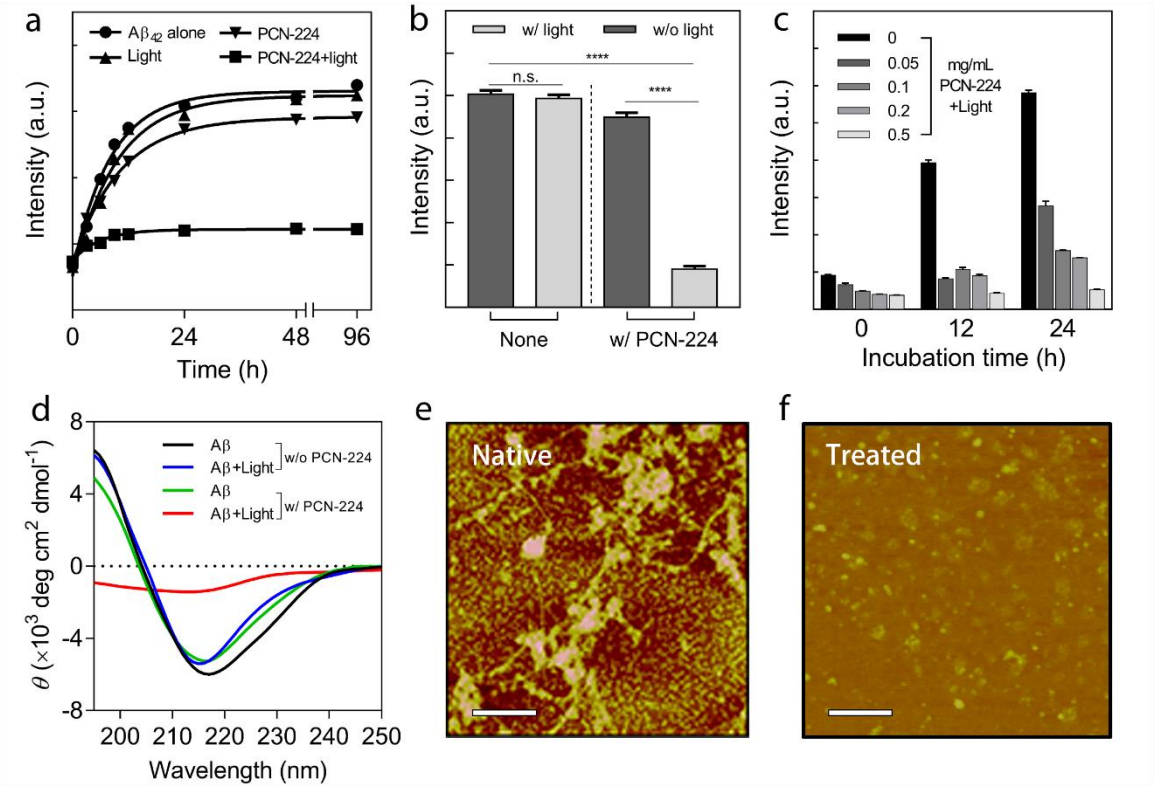

Figure 3.4 The photo-inhibitory effect of PCN-224 nanoparticles on the Aβ42 aggregation. (a) ThT fluorescence intensity versus time curves of Aβ42 incubated in the dark environment without nanoparticle, in the presence of PCN-224 nanoparticle alone, in the presence of light irradiation alone, in the presence of PCN-224 nanoparticles under light irradiation at 650 nm up to 96 h. (b) ThT fluorescence intensities of Aβ42 after incubation of 24 h with different treatments. One-way analysis of variance (ANOVA) was used for data analysis (****$p < 0.0001$, n.s.: not significant). (c) ThT fluorescence intensities of Aβ42 treated with different amount of PCN-224 nanoparticles under 650 nm light irradiation and incubated at 37 °C for 0 h, 12 h, and 24 h. (d) CD spectra of Aβ42 peptide (25 μM) with different treatments. (d) AFM image of the self-assembly of native Aβ42. (e) AFM image of Aβ42 peptide treated with 0.5 mg mL^{-1} of PCN-224 nanoparticles and light irradiation (30 mW cm^{-2}) for 30 min. Scale bars indicate 500 nm. Both samples were incubated at 37 °C for 24 h before AFM measurements.

The effect of photo-activated PCN-224 nanoparticles on the suppression of Aβ aggregation was further studied with TEM microcopy, native gel electrophoresis and dynamic light scattering (DLS). Highly aggregated fibrils were observed for Aβ42 incubated without PCN-224 nanoparticles in the dark environment under TEM microscope (Figure 3.5a). The photo-activated PCN-224 nanoparticle treated Aβ42, however, did not transform to oligomers or fibrils after 24 h incubation (Figure 3.5b). Native gel electrophoresis was used to measure the molecular weight change of Aβ42 peptide under various treatments (Figure 3.5c). It was observed that large oligomers and fibrils (~ 90 – 170 kDa) were formed in Aβ42 without PCN-224 in the dark

environment (lane 1), Aβ42 with light irradiation alone (lane 2), and Aβ42 with PCN-224 alone (lane 3). However, after treated with PCN-224 with light irradiation (lane 4), Aβ42 monomeric band (~ 4.5 kDa) and dimeric band (~ 9 kDa) were observed which demonstrated the inhibition effect of photo-activated PCN-224 nanoparticle. PCN-224 nanoparticle alone did not show any bands in lane 5 due to its positive charge, demonstrating that the PCN-224 nanoparticles did not interfere with the native gel electrophoresis results. The dynamic size change of the Aβ42 peptide after the PCN-224 nanoparticle treatment under light illumination was further determined by DLS analysis (Figure 3.5d). PCN-224 nanoparticles were removed by centrifugation prior to the DLS analysis. Obviously, Aβ42 incubated without PCN-224 nanoparticles under dark environment showed a gradually increased size from around 50 nm to around 700 nm after 24 h incubation due to the formation of Aβ fibrils. In contrast, Aβ42 treated with photo-activated PCN-224 under light irradiation remained sub-100 nm structures after 24 h incubation.

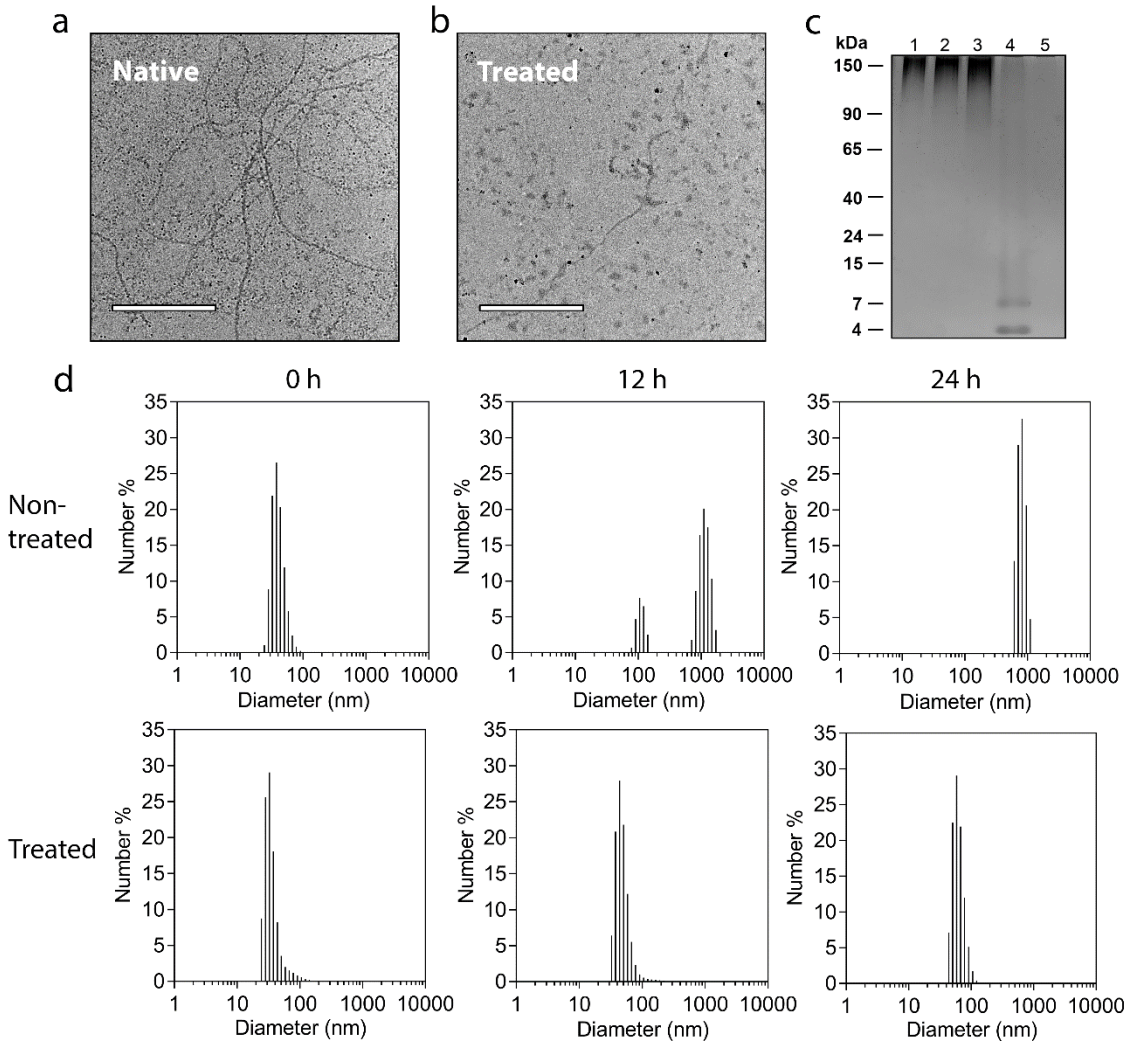

Figure 3.5 (a) TEM image of non-treated Aβ42 incubated at 37 °C for 24 h. (b) TEM image of Aβ42 treated with PCN-224 nanoparticles under light irradiation at 650 nm for 30 min and then incubated at 37 °C for 24 h. Scale bars indicate 0.5 μm. (c) Native gel electrophoresis of Aβ42 with different treatments. Lane 1: Aβ42 without PCN-224 nanoparticle in the dark environment; Lane 2: Aβ42 with light irradiation alone; Lane 3: Aβ42 with PCN-224 nanoparticles alone; Lane 4: Aβ42 with PCN-224 nanoparticles under light irradiation; Lane 5: PCN-224 nanoparticles alone. (d) DLS size distribution of monomeric Aβ42 without treatment and treated with PCN-224 nanoparticles under light irradiation over 24 h incubation at 37 °C.

We proposed that the light-induced inhibition on Aβ42 aggregation was due to the generation of reactive oxygen species (ROS) by PCN-224 nanoparticles under light irradiation. Porphyrin MOFs have been reported as effective photosensitizers for singlet oxygen $^1O_2$ generation. The capability of the ROS generation of PCN-224 under 650 nm light illumination was examined using 1,3- diphenylisobenzofuran (DPBF), a sensitive $^1O_2$ trapping reagent that can react with ROS and show an absorbance peak decrease at 414 nm. The remarkable reduction of DPBF absorbance at 414 nm over the

irradiation time due to the quenching reaction with $^1O_2$ demonstrated the high $^1O_2$ production capability of PCN-224 nanoparticles (Figure 3.6a). PCN-224 nanoparticles showed a higher $^1O_2$ production capability than a commonly used photosensitizer rose bengal (RB) under the same conditions in the DPBF absorbance versus time curves (Figure 3.6b). The generation of ROS by PCN-224 nanoparticles was further assessed by 2',7'-dichlorodihydrofluorescein diacetate (DCFH-DA) fluorescence assay and electron spin resonance (ESR) under light illumination. As shown in Figure 3.7a and 3.7b, the fluorescence intensity of DCFH-DA at wavelength of 541 nm increased significantly in the presence of PCN-224 under 650 nm light irradiation, which was due to the oxidization of non-fluorescent 2',7'-Dichlorofluorescin diacetate and transformed to highly fluorescent oxidized product 2',7'-Dichlorofluorescein. As shown in Figure 3.7c, the ESR signal intensity significantly increased upon light illumination, which demonstrated the generation of $^1O_2$ by PCN-224 nanoparticle under light irradiation. The oxidation of Aβ42 by singlet oxygen was then verified by a 2,4-dinitrophenylhydrazine (DNPH) assay. Generally, protein oxidation by ROS could generate carbonyl group on protein side chains. The DNPH can sensitively react with the carbonyl group on oxidized protein and leads to the formation of a stable 2,4-dinitrophenyl (DNP) hydrazone with a characteristic absorption peak at around 370 nm. As shown in Figure 3.6c, only Aβ42 treated with PCN-224 nanoparticles under light irradiation showed increased amplitude for absorption peak at 370 nm, which indicated the oxidation of Aβ42.

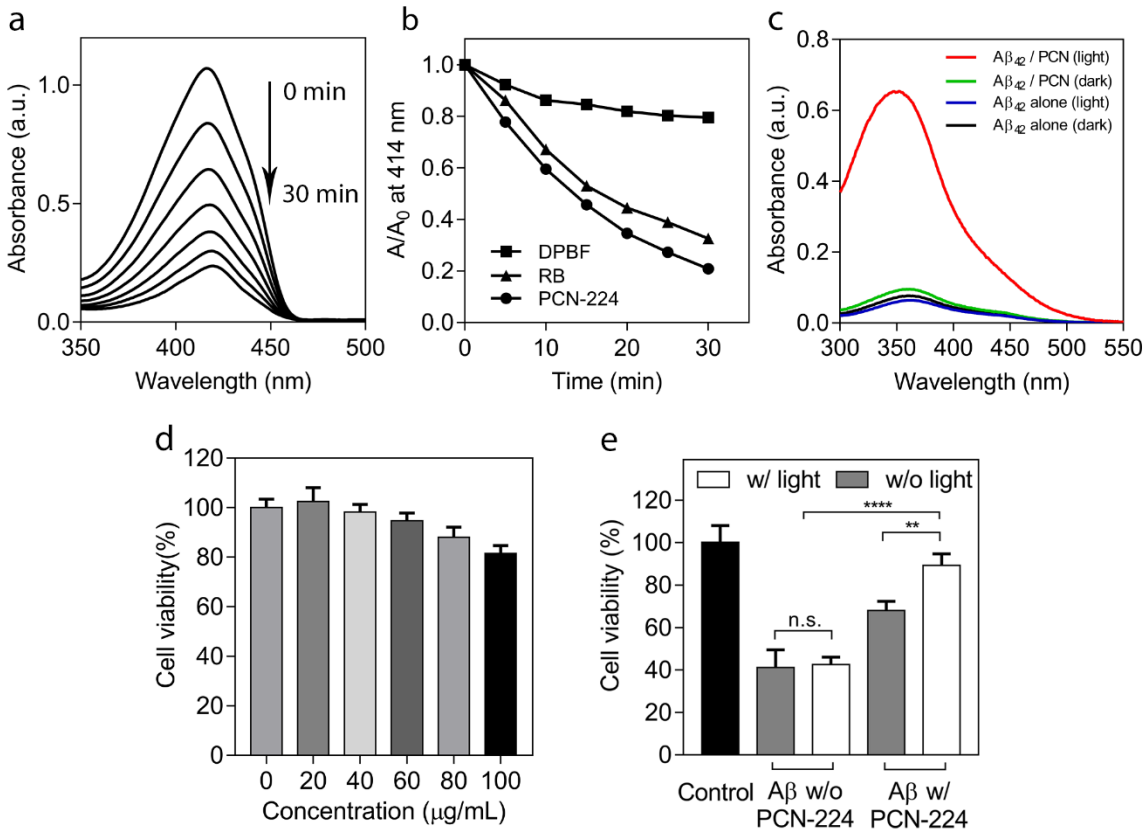

Figure 3.6 Photo-oxygenation capability tests for PCN-224 nanoparticles. (a) UV-vis spectra of DPBF assay was used as singlet oxygen indicator to evaluate the ROS generation ability of PCN-224 nanoparticles. (b) Absorbance of DPBF at 414 nm decreased significantly compared to control group (in the absence of PCN-224). PCN-224 nanoparticles showed even higher photo-oxygenation capability compared with the classic photosensitizer rose bengal (RB) in the same condition. (c) DNPH assay of Aβ42 with different treatments to show the protein oxidation degree. (d) Cytotoxicity of PCN-224 nanoparticles. (e) PC12 cell viability treated under various conditions. One-way analysis of variance (ANOVA) was used for data analysis (**$p < 0.01$, ****$p < 0.0001$, n.s.: not significant).

Next, the ability of photo-activated PCN-224 nanoparticles to reduce Aβ-induced cytotoxicity was investigated in PC12 cell using 3-(4,5-dimethylthiazol-2yl)-2,5-diphenyltetrazolium bromide (MTT) assay. First of all, PCN-224 nanoparticle itself showed good biocompatibility with a high cell viability over 80% even at high concentrations up to 100 μg mL^{-1} (Figure 3.6d). High cytotoxicity of Aβ42 aggregates assembled under dark environment or with light irradiation was observed with a low cell viability around 40% after 24 h incubation (Figure 3.6e). In contrast, cell viability was significantly elevated to 90% when Aβ42 was incubated with PCN-224 nanoparticles under 650 nm light irradiation. The cell viability was around 65% with Aβ42 incubated with PCN-224 nanoparticles alone under dark environment. This

increase of cell viability could be attributed to the physical absorption of Aβ42 onto PCN-224 nanoparticles, which led to a slightly low toxicity to cells. Overall, PCN-224 nanoparticles could markedly attenuate the cytotoxicity of Aβ42 by inhibiting aggregation of monomeric Aβ42 peptide under 650 nm light irradiation.

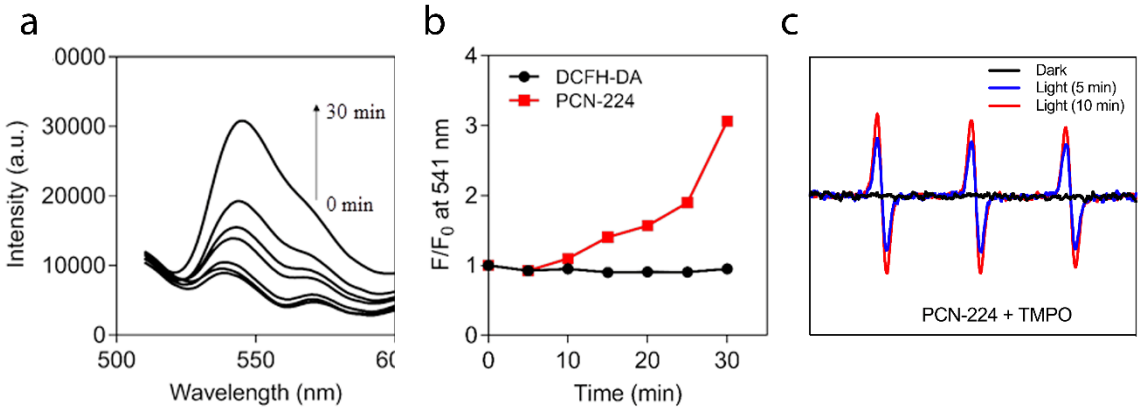

Figure 3.7 (a) DCFH-DA assay for measurement of singlet oxygen generation upon treatment with PCN-224 nanoparticles under light illumination. Irradiation time from bottom to up was from 0 min to 30 min with a 5 min interval. Irradiation light source was 650 nm. λ_{ex} = 480 nm. (c) ESR spectra of $^1O_2$ obtained in the presence of PCN-224 nanoparticles under 650 nm light irradiation for 5 min and 10 min, respectively.

3.4 Discussion

A facile strategy for the inhibition of cross-β-sheet aggregation of Aβ42 peptide using light irradiated PCN-224 nanoparticles has been developed. Inspired by the photodynamic property of porphyrin TCPP ligand in the framework and its capability of photooxygenation with NIR light, we successfully synthesized PCN-224 MOF nanoparticles for the inhibition of Aβ42 aggregation *via* photooxygenation. We found that light irradiated PCN-224 was able to attenuate the aggregative activity of Aβ42 as well as decrease cytotoxicity to PC12 cells. This photooxygenation approach based on PCN-224 nanoparticle provides three main advantages compared with existing photooxygenation methods: (1) porphyrin MOF could deliver NIR light to brain more effectively compared with other materials using visible light; (2) functional porphyrin linkers are spatially separated by Zr clusters in MOF framework, which avoided the self-quenching of the excited state and retained the photooxygenation property of single

porphyrin linker. Overall, such NIR light-triggered therapeutic photooxygenation of Aβ42 based on porphyrin MOF is expected to hold great promise for the non-invasive photo-treatment of neurodegenerative diseases like Alzheimer's disease.

4 PCN-222@Indocyanine Green Nanosheet for Combinatory Inhibition of Amyloid-β Aggregation

4.1 Introduction

Many studies have revealed that oxygenated Aβ monomer has poor aggregation potency compared with native Aβ monomer and a variety of photo-inhibitors including methylene blue (MB)[96] and rose bangel (RB)[90] have been developed for photooxygenation of Aβ monomer. Nevertheless, the above organic inhibitors show moderate inhibition capabilities for suppressing Aβ aggregation *in vivo* and suffer from rapid degradation during circulation. Nanomaterial-mediated photooxygenation strategies have since been extensively explored for inhibition of Aβ aggregation. Examples including carbon nanodots[87], graphitic carbon nitride nanosheets (g-C_3N_4)[97], upconversion nanoparticles (UCNP)[91] have been employed based on the photooxygenation for the inhibition of Aβ aggregation. The major limitation is that these materials only absorb visible light to generate singlet oxygen for Aβ oxygenation, which makes them unsuitable for biological applications because visible light has low tissue penetration depth. Black phosphorus (BP) was developed for the NIR-induced inhibition of Aβ aggregation, but its ambient instability largely limited its diverse applications[98]. We have previously synthesized PCN-224 MOF and used it as an inhibitor against Aβ aggregation under NIR light irradiation. PCN-224 nanoparticles absorb 650 nm light and transfer the light energy to singlet oxygen to oxygenate the Aβ.

In addition to photooxygenation, thermal inhibition of amyloid aggregates has recently become biologists' research interests and been considered as another promising approach for AD therapy. Compared with traditional chemotherapeutic strategies, photothermal treatment shows several advantages such as reduced side effects and high selectivity since only the region exposed to light is treated. Studies

have reported that graphene oxide (GO)[75] and tungsten disulfide (WS_2)[99] nanosheet could be excellent candidates for NIR photothermal treatment of AD. Both GO and WS_2 have strong NIR optical absorption thus can generate local heat to treat the Aβ monomer under low-power NIR laser irradiation. However, moderate heat alone can barely inhibit the Aβ self-assembly whereas strong heat could lead to undesirable inflammation in the human body. Also, whether these nanomaterials can cross the blood-brain barrier (BBB) is still not clear.

In this chapter, for the first time a combinatory strategy – photooxygenation/photothermal inhibition of the Aβ42 aggregation based on a single nanoprobe is described. By using a hybrid nanosystem composed of metal-organic framework (MOF) PCN-222 nanosheet and indocyanine green (ICG), Aβ monomers can not only be photo-oxygenated by the nanoprobe, its aggregation process can also be inhibited by the photothermal effect of ICG under NIR light. The PCN-222 nanosheet with the integration of tetra-kis(4-carboxyphenyl)porphyrin (TCPP) as ligands into the MOF structure showed strong light-to-oxygen generation ability due to the high percentage of exposed ligands in the framework and easy diffusion of molecular oxygen through the porous structure. The conjugation of ICG – an FDA approved photosensitizer and photothermal agent on the surface of PCN-222 improved the biocompatibility and biosafety of the nanosystem. Moreover, both PCN-222 and ICG absorb deep tissue-penetrative NIR light for photooxygenation and photothermal inhibition for Aβ, making this nanosystem a promising candidate for phototherapy of AD and other brain diseases (Figure 4.1). In the meantime, the brain-targeting peptide rabies virus glycoprotein (RVG) coupled with PCN-222@ICG could largely improve BBB permeability of the nanoprobe. In addition, a microfluidic device was then designed and fabricated as an *in vitro* brain model to dissect the BBB permeability of

the nanoprobe. Our results indicated that the PCN-222@ICG@RVG nanosystem could cross the BBB, allowing for a combinatory inhibition of Aβ aggregation and phototherapy of AD.

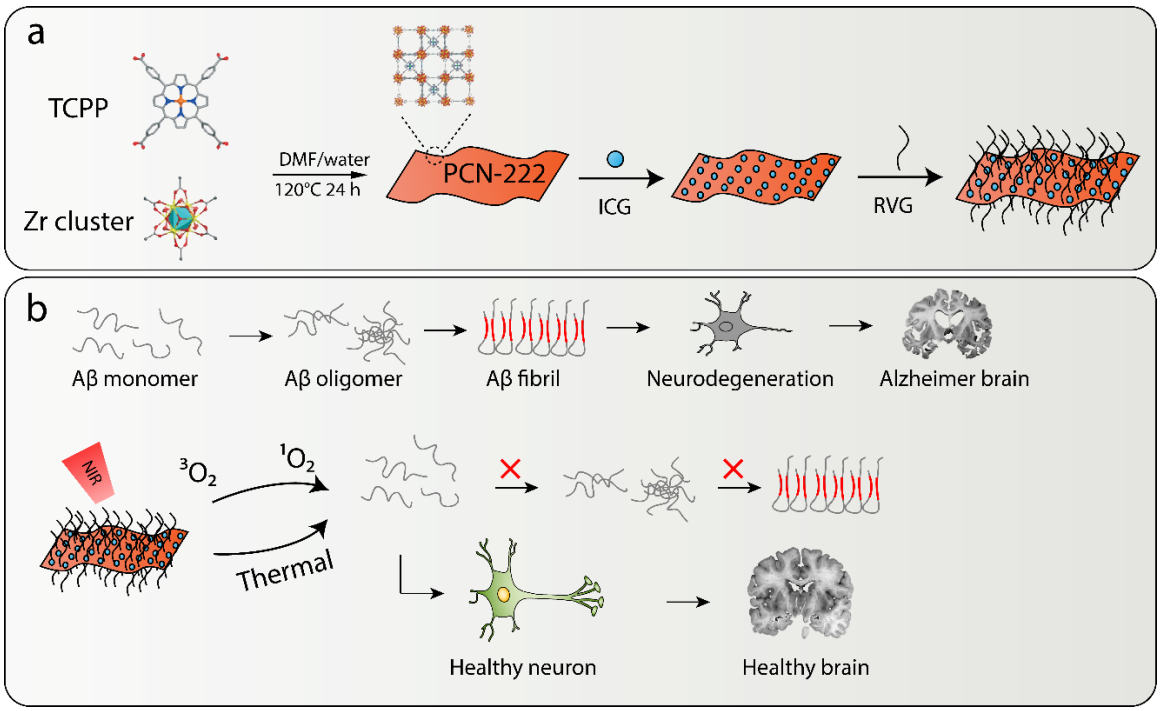

Figure 4.1 (a) Schematic illustration of the synthesis of PCN-222@ICG nanoprobe and RVG peptide conjugation. (b) Schematic illustration of Aβ-induced neurodegeneration. (c) Schematic illustration of photo-induced inhibition of Aβ42 aggregation by a hybrid PCN-222@ICG nanoprobe modified with brain-targeting peptide RVG.

4.2 Methodology

4.2.1 Synthesis of PCN-222 Nanosheets

Two-dimensional PCN-222 nanosheets were prepared according to the previous method with slight modifications. Briefly, 10 mg $ZrOCl_2 \cdot 8H_2O$, 30 mg TCPP, 240 µL of FA and 50 µL water were added to DMF to a final volume of 2 mL in a Teflon-lined stainless-steel autoclave and then heated at 120 °C for 24 h. After cooling down to room temperature, the PCN-222 nanosheets were separated through centrifugation at 13500 rpm for 30 mins and further rinsed with DMF and ethanol for several times until there was no red fluorescence observed in the supernatant under UV light. 50 mg as-synthesized MOFs and 1 mL of 8 M HCl were added into 20 mL DMF, the DMF suspension was stirred at 120 °C for 12 h to remove unreacted inorganic species,

starting ligands and modulating reagents. The products were further separated by centrifugation and then dispersed into fresh acetone for 24 h to exchange and remove DMF. After the removal of acetone by centrifugation, the sample was activated by drying under vacuum at 100 °C for 24 h.

4.2.2 ICG and RVG Conjugation on PCN-222

50 mg activated PCN-222 nanosheets were first sonicated for 5 mins and mixed with 10 μM of ICG in ultrapure water and stirred for 24 h at room temperature. Residual ICG was then removed by centrifugation at 13500 rpm for 30 mins and rinsed with water for several times. The immobilization of RVG peptide on PCN-222@ICG *via* physical adsorption. The obtained PCN-222@ICG was mixed with 500 μL 5 mg mL^{-1} RVG peptide and shaken for 4 h. Afterwards, the product was centrifuged at 12000 rpm for 10 mins and washed with Milli-Q water for three times.

4.2.3 Characterization of PCN-222@ICG Hybrid Nanoprobe

The TEM images were collected with a JEOL JEM-2100F TEM microscope. SEM images were obtained in a JEOL Field Emission SEM microscope. Ultraviolet-visible (UV-vis) absorbance of PCN-222 and PCN-222@ICG were measured by Ultrospec 2100 Pro spectrophotometer (Amersham Biosciences). Powder X-ray diffraction (PXRD) patterns were collected at 293 K with a Rigaku SmartLab X-Ray diffractometer using Cu/Kα radiation. Zeta potential and size distribution of the PCN-222@ICG nanosheets were measured using a Malvern ZEN 3600 Zetasizer. The Fourier Transform Infrared (FTIR) spectra were obtained with a Bruker Vertex-70 IR Spectroscopy in the wavelength region of 400 – 4000 cm^{-1}. BET (Brunauer-Emmett-Teller) surface area analysis was performed with a Micromeritics ASAP 2420 analyzer.

4.2.4 Characterization of Singlet Oxygen Generation

Singlet oxygen was characterized by DPBF assay. Briefly, (0.2 mg mL^{-1}) and DPBF (0.04 μM) were dissolved in DMF and stirred for 5 mins before exposed to 808 nm NIR light at a power density of 0.6 W cm^{-2}. The UV-vis absorption was recorded with a spectrophotometer at the same time intervals. $^1O_2$ was also identified by ESR obtained with JES-FA200 Electron Spin Resonance Spectrometer using 4-oxo-TEMP.

4.2.5 Characterization of Photothermal Effect

PCN-222@ICG was dispersed in water in a 1.5 mL Eppendorf tube which was then exposed under 808 nm light at a power density of 0.6 W cm^{-2} in a black container. Thermal camera was used to monitor the temperature change by taking photos of the sample at different time points.

4.2.6 Preparation of Monomeric Aβ42 Solution

Human Aβ42 (1 mg) was dissolved in hexafluoro-2-propanol (HFIP) and kept at room temperature for 2 h. The HFIP was then removed under a gentle flow of nitrogen gas followed by freeze-drying for 3 h. The obtained Aβ42 peptide (1mg) was dissolved in 10 μL of DMSO and then diluted to 300 μM with ultrapure water (Invitrogen). The solution was further diluted in HEPES buffer (20 μM, pH 7.4, 150 μM NaCl) to a final concentration of 25 μM for the inhibition study.

4.2.7 Inhibition Study of Aβ42 Aggregation Under NIR Light Irradiation

For inhibition studies, PCN-222 nanosheets and PCN-222@ICG were mixed with Aβ42 solution (25 μM) at concentration of 100 μg mL^{-1}. The mixed solution was then exposed to the NIR light irradiation (808 nm, 0.6 W cm^{-2}) for 30 mins and incubated at 37 °C for 24 h.

4.2.7.1 ThT Assay

ThT stock solution was prepared by dissolving 0.32 mg of ThT in 10 mL ultrapure water and filtering through a 0.22 μm PES syringe filter. 100 μL of the solution containing 10 μM of ThT and 15 μM of Aβ42 peptide was measured by a fluorescence spectrometer. The fluorescence intensity was recorded using an excitation wavelength of 440 nm and an emission wavelength of 485 nm. All samples were performed in triplicate. PCN-222 nanoprobes were removed by centrifugation (21120 g, 30 mins) before ThT assay to prevent the nanoparticles from interfering with the photoluminescence property of ThT during the analysis of Aβ42 aggregation.

4.2.7.2 CD measurement

Far-UV (190-260 nm) of CD spectra were recorded with a JASCO J-810 Spectrometer (JASCO Co., Tokyo, Japan), using a quartz cuvette with 1 mm path length. 25 μM of Aβ42 peptide with and without nanoproble treatments were used for CD measurement. The CD spectrum was scanned three times in the range of 195 – 250 nm under N_2 blowing atmosphere. Conformational changes of peptides were analyzed at 195 and 216 nm, respectively.

4.2.7.3 DLS measurement

The size distribution of incubated Aβ42 peptide (25 μM) was measured using a light scattering spectrometer (Zetasizer Nano ZS instrument; Malvern Instruments, Worcestershire, UK). The Aβ42 samples were centrifuged at 16000 g for 30 mins at 4 °C and the supernatant was measured by DLS at 25 °C. Each scan consisted of 11 runs and each sample was measured at least three times.

4.2.7.4 TEM analysis

Five microliter of each Aβ42 peptide sample (25 μM) was placed on glow-discharged, 300-mesh formvar/carbon coated copper grid. The samples were stained with 2%

uranyl acetate and then the grids were washed at least three times following by drying at room temperature before measurement. The TEM images were collected with a JEOL JEM-2100 F microscope with an accelerating voltage of 75 kV.

4.2.7.5 Native gel electrophoresis analysis

Aβ42 samples were mixed with sample buffer and loaded to a 10% precast gel (SDS free, Bio-Rad) for measurement in a MiniPROTEAN® Tetra Cell (Bio-Rad) with a current of 100 V for 80 mins. Silver staining was performed using a silver staining kit (Bio-Rad) according to the manufacturer's instructions. The gel was then imaged with a ChemiDoc Touch Imaging System (BioRad).

4.2.8 *In vitro* Study of photo-inhibition of Aβ42 Aggregation

PC12 cells were cultured in medium containing 15% HS, 2.5% FBS, and 1% antibiotics, under 5% of CO_2 atmosphere at 37 °C. For biocompatibility test, around 1.0×10^5 cells mL^{-1} were seeded into 96 well plates and incubated for 24 h. PCN-222 nanosheets were then added to the 96 well plate at different concentrations and incubated for 24 h before subjected to the MTT assay. For the photo-inhibition test, non-treated, NIR light-treated, PCN-222-treated, and PCN-222 with light illumination treated Aβ42 peptide were added to the PC12 cells in a 96 well plate and incubated for 24 h.

4.2.9 MALDI-TOF MS Measurement

MALDI-TOF MS spectra were recorded on the Bruker UltrafleXtreme MALDI-TOF-TOF Mass Spectrometer using α-cyano-4-hydroxy cinnamic acid as a matrix. Native Aβ42, Aβ42 irradiated with NIR light in the presence of PCN-222@ICG for 0.5 h and 1 h were measured by the MALDI-TOF MS.

4.3 Results

4.3.1 Characterization of PCN-222@ICG Hybrid Nanoprobe

PCN-222@ICG nanoprobes were prepared by a two-step method including solvothermal synthesis of porphyrin MOF PCN-222 nanosheet and physical adsorption of ICG to the MOF nanosheet. Compared to 3D bulk MOF crystals, 2D MOF nanosheets possess extremely high percentages of exposed catalytic active sites and larger surface area, which are beneficial for loading ICG through electrostatic adsorption and oxygen transformation. The as-synthesized PCN-222 nanosheet exhibited an ultrathin 2D crystal structure, although some nanosheets self-rolled up and become rod-shaped under TEM microscopy (Figure 4.2a). The nanoprobe did not change its 2D morphology after electrostatic adsorption of ICG. Field-emission scanning electron microscopy (FESEM) images of PCN-222@ICG is well consistent with its TEM images. Dynamic light scattering (DLS) was used to measure the size of PCN-222 before and after ICG modification. Figure 4.2b indicated that the DLS size of PCN-222@ICG was around 120 nm, which was slightly larger than that of PCN-222. The UV-vis absorption spectra showed a significant increase in the region of 700 ~ 900 nm after modification of ICG, demonstrating the successful loading of ICG in the PCN-222 nanosheet (Figure 4.2c). The elevated NIR absorption of the hybrid nanoprobe provided the possibility for the combinatory NIR phototherapy of AD. The powder X-ray diffraction (PXRD) pattern of both PCN-222 and PCN-222@ICG nanosheets displayed three obvious peaks which can be assigned to (0, 0, 1), (2, 0, 1), and (3, −1, 1), consistent with the standard XRD spectrum of PCN-222 (Figure 4.2d). Zeta potential of the nanoprobe was also measured to demonstrate the successful loading of ICG. Due to the negative surface charge of ICG, the hybrid nanoprobe became negatively charged instead of positively charged in aqueous solution (Figure 4.2e). The successful modification of ICG was also evidenced by the color change of the

nanoprobe dispersed in water from red to green colour under day light (Figure 4.2e inset).

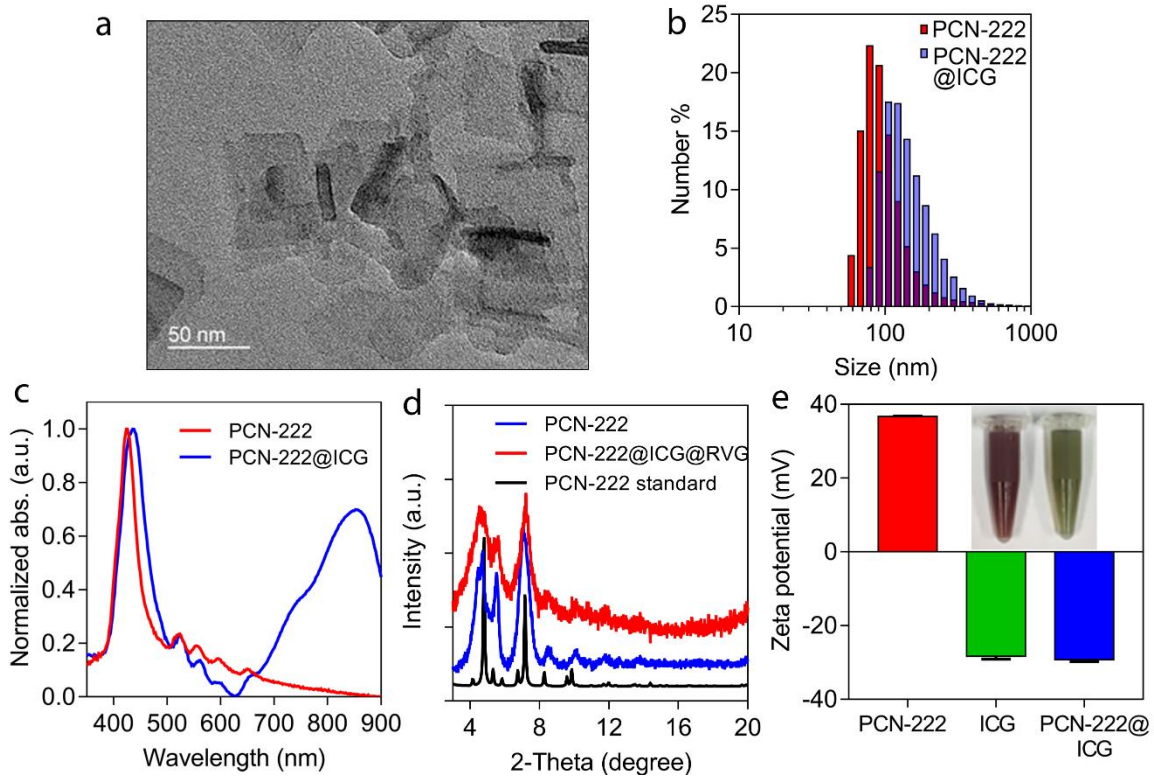

Figure 4.2 Characterization of PCN-222@ICG nanosystem. (a) TEM image of PCN-222@ICG nanosheet. (b) DLS size of PCN-222 and PCN-222@ICG. (c) UV-vis spectra of PCN-222 and PCN-222@ICG. (d) Powder XRD spectra of PCN-222 and PCN-222@ICG. (e) Zeta potential of PCN-222, free ICG, and PCN-222@ICG. Inset is the photograph of PCN-222 before (left) and after (right) coupled with ICG.

4.3.2 Characterization of $^1O_2$ generation

As porphyrin is described as the third-generation photosensitizer, it has been extensively used for photodynamic therapy (PDT) of many diseases, particularly the therapy of solid tumors[59]. Porphyrin-based nanostructures, therefore, have been widely used for in singlet oxygen generation in photocatalysis due to its high efficiency in light harvesting[100]. Numerous publications have reported that zirconium-porphyrin MOFs have strong photon absorption and able to transfer $^3O_2$ to $^1O_2$ upon light irradiation[88]. To verify the generation of $^1O_2$ species, 1,3-diphenyl-isobenzofuran (DPBF) assay was conducted to measure the singlet oxygen production of our nanosystem. The characteristic absorption of DBPF at 414 nm decreased by one fifth in the presence of

PCN-222@ICG nanoprobe under NIR light irradiation for ten minutes, revealing the generation of $^1O_2$ species (Figure 4.3a). Although the PCN-222 alone can produce $^1O_2$ species, the $^1O_2$ generation efficiency was lower than the hybrid nanosystem (Figure 4.3b). 4-oxo-2,2,6,6-tetramethylpiperidine (4-oxo-TEMP) was able to react with $^1O_2$ to yield the stable nitroxide radical 4-oxo-TEMPO, which could be measured through electron spin resonance (ESR). As is shown in Figure 4.3c, the characteristic $^1O_2$-induced TEMPO signal of PCN-222 was observed in the ESR spectra under NIR light irradiation, and its intensity increased with the increase of irradiation time, which was further confirmed the $^1O_2$ formation. The ESR signal intensity of PCN-222@ICG was two-fold higher than PCN-222 due to the ROS generation ability of ICG under NIR irradiation. Furthermore, to investigate the photostability of the nanosystem, PCN-222@ICG was irradiated under NIR light for 30 mins and its UV-vis absorbance evidenced that the hybrid nanosystem was fairly stable under light irradiation.

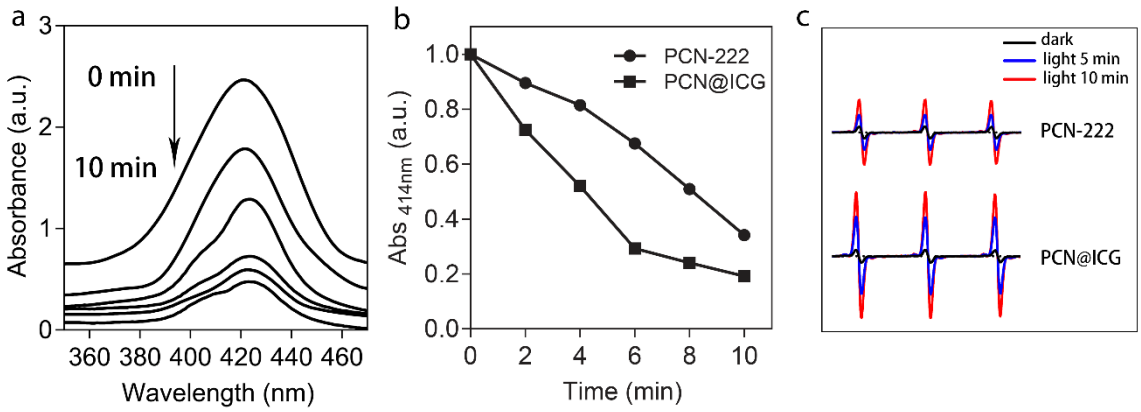

Figure 4.3 Characterization of $^1O_2$ formation. (a) UV-vis absorbance of DPBF in the presence of PCN-222@ICG when exposed to NIR light (808 nm, 0.6 W cm^{-2}) for 0-10 mins. (b) comparison of UV-vis absorbance of DPBF at 414 nm between PCN-222 and PCN-222@ICG. (c) ESR spectra of PCN-222@ICG after exposed to NIR light for 5 and 10 mins.

4.3.3 Characterization of photothermal effect of PCN-222@ICG

The PCN-222@ICG loaded with ICG is expected to serve as an NIR photothermal agent for the phototherapy of disease as it has strong absorption in NIR region. This porphyrin nanoprobe can produce remote and localized heat in an efficient manner

when externally excited by NIR light irradiation. To examine the photothermal effect of PCN-222@ICG, 808 nm light was employed to irradiate the nanoprobe and the generated heat was measured by a thermal camera. The PCN-222 with and without ICG modification and water was exposed to the NIR light at different power densities. As anticipated, the temperature of nanoprobe solution at a concentration of 0.025 mg ml^{-1} rapidly rose to 45 °C when exposed to 0.6 W cm^{-2} NIR light. By contrast, water and PCN-222 alone as control groups, did not show obvious temperature change throughout the irradiation period (Figure 4.4a). The temperature of the nanoprobe solution showed a power density- and concentration- dependent increase under 5 mins light irradiation (Figure 4.4a and 4.4b). In addition, to further assess the photothermal transduction ability of the nanoprobe, PCN-222@ICG solution was exposed to NIR light for 300 seconds before shutting the light. It was observed that the temperature of nanoprobe solution quickly dropped to room temperature, suggesting an excellent thermal conductivity of the hybrid nanoprobe (Figure 4.4c). Moreover, temperature variations of PCN-222@ICG solution at a concentration of 100 μg mL^{-1} under continuous 808 nm light irradiation for five on-off cycles. As depicted in Figure 4.4d, the nanoprobe solution remained its initial photothermal effect without any decrease of temperature elevation, demonstrating good photothermal stability of the nanosystem. The thermal images of the nanoprobe solution captured by thermal camera under light irradiation reflected the temperature change and confirmed the photothermal efficacy of the ICG-loaded MOF (Figure 4.4e). The above results evidenced that PCN-222@ICG is an ideal photothermal agent with superior photostability.

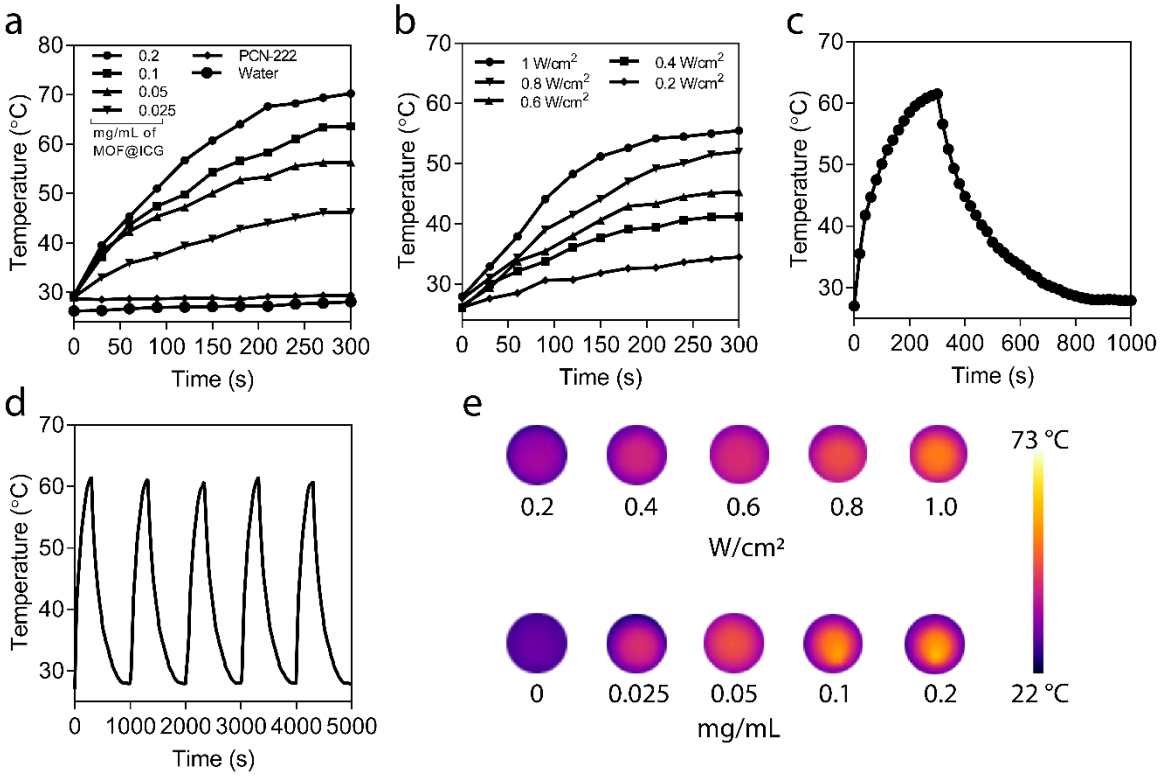

Figure 4.4 Photothermal effect of PCN-222@ICG. (a) Concentration-dependent temperature increase for PCN-222@ICG. (b) Power density-dependent temperature increase of PCN-222@ICG. (c) Photothermal transduction ability of PCN-222@ICG. (d) Photothermal stability of the PCN-222@ICG. (e) Thermal images of PCN-222@ICG.

4.3.4 Photo-induced Attenuation of Aβ42 Aggregation Based on PCN-222@ICG

To investigate the effect of PCN-222@ICG nanoprobe on the inhibition of Aβ42 aggregation, the PCN-222 and PCN-222@ICG were irradiated with NIR light in the presence of Aβ42 monomers. The mixture was further incubated at 37 °C for 24 hours. Aβ42 monomers without treating with any nanoprobe incubated under the same condition designated as "Native". The fibrillation kinetics were monitored by a commonly used Thioflavin T (ThT) assay. ThT is an extrinsic fluorescent dye that specifically binds to β-sheet-rich amyloid structure with a significant fluorescence increase at the wavelength of 485 nm. The ThT fluorescence of native Aβ42 drastically increased during the first 24 hours at 37 °C and reached plateau afterwards. Aβ42 treated with photo-activated PCN-222 resulted in a minor increase in the ThT fluorescence intensity. PCN-222@ICG treated Aβ42, however, it had lower ThT

fluorescence intensity, indicating the presence of a lower order of Aβ structure and an effective suppression of Aβ42 aggregation (Figure 4.5a). The Aβ42 monomer with and without NIR light irradiation led to markedly higher ThT fluorescence intensity than those treated with only nanoprobe or only light irradiation (Figure 4.5b). To clarify the enhanced inhibitory effect of PCN-222@ICG on Aβ42, circular dichroism (CD) was used to measure the secondary structure of the peptides. The non-treated Aβ42 showed two characteristic peaks at 195 and 216 nm, which are the typical profile of the β-sheet-rich secondary structure of amyloids. However, Aβ42 treated with photo-activated PCN-222@ICG showed negligible peaks around 195 and 216 nm, implying the marginal formation of amyloid aggregates (Figure 4.5c). The Aβ42 treated with PCN-222@ICG under light irradiation was also evaluated by a native polyacrylamide gel electrophoresis (PAGE) analysis. Compared to the native Aβ42 and Aβ42 treated with nanoprobes which aggregated into high molecular weight oligomers and fibrils, Aβ42 remained low-order monomers after incubated with PCN-222@ICG under light irradiation (Figure 4.5d).

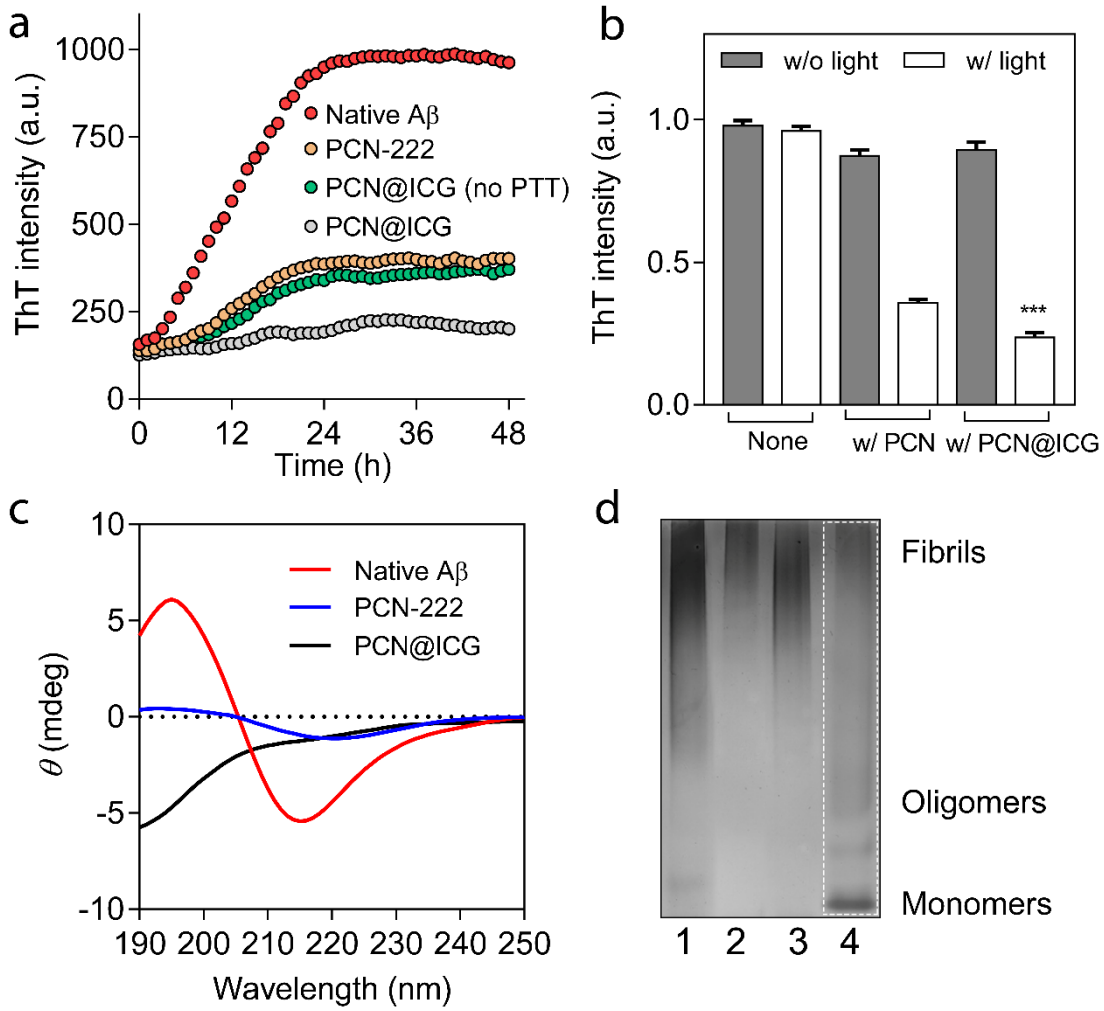

Figure 4.5 Photo-induced attenuation of Aβ42 aggregation based on PCN-222 and PCN-222@ICG nanoprobes. (a) Aβ42 aggregation kinetics before and after nanoprobe treatments. (b) ThT fluorescence intensity of native Aβ42, and Aβ42 with different treatments. (c) CD analysis of native Aβ42, and Aβ42 with treatments of nanoprobes. (d) Native PAGE of Aβ42. 1: native Aβ42; 2: Aβ42 with PCN-222; 3: Aβ42 with PCN-222@ICG; 4: Aβ42 with PCN-222@ICG under NIR irradiation.

The time-dependent inhibition studies by DLS and TEM over 24 hours are summarized in Figure 4.6. Light-activated PCN-222@ICG could more effectively prevent the Aβ42 from aggregating to larger size compared with the treatment of PCN-222 alone (Figure 4.6a). TEM images show almost no fibrillar morphologies for Aβ42 after treatment with PCN-222@ICG and incubated for 24 hours (Figure 4.6b-d). Our studies demonstrated that NIR-activated PCN-222@ICG was able to more noticeably inhibit the Aβ42 aggregation than PCN-222 alone and control the Aβ peptides under sub-100 nm structures. FTIR was also used to verify the β-sheet structure in the Aβ42 peptide. FTIR spectrum of Aβ42 incubated for 24 hours reveals peak at 1636 cm^{-1},

which clearly indicated the fibril structures of Aβ42. However, Aβ42 in the presence of PCN-222@ICG under NIR irradiation did not show a significant peak at 1636 cm^{-1}, indicating the inhibition of peptide aggregation.

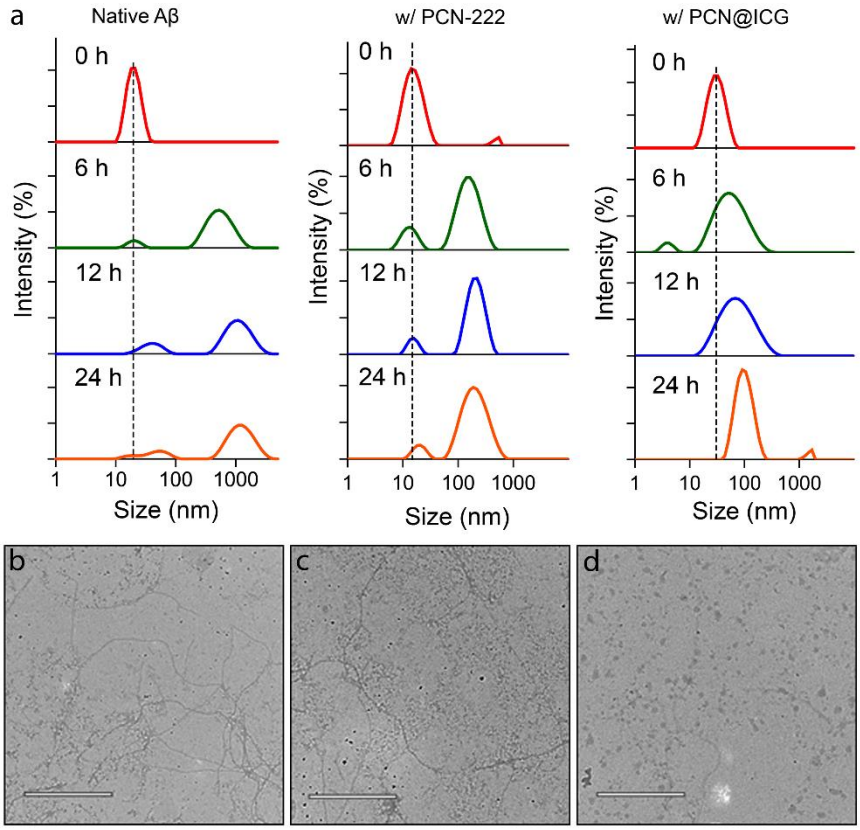

Figure 4.6 Inhibition effect on the Aβ42 aggregation by the photo-activated PCN-222 and PCN-222@ICG nanoprobes. DLS (panel a) were recorded at four different time points and TEM images (bottom) were obtained after 24 hours. Panel b: Native Aβ42; panel b is Aβ42 treated with PCN-222 under light irradiation; panel c: Aβ42 treated with PCN-222@ICG under light irradiation (808 nm, 0.6 W cm^{-2}). The scale bars for TEM images are 500 nm.

4.3.5 Attenuation of Aβ-induced Cytotoxicity by Photo-activated PCN-222@ICG

Next, the MTT assay was employed to evaluate the toxicity of PCN-222 and PCN-222@ICG and their regulatory ability towards Aβ-induced toxicity using pheochromocytoma (PC12) cells. PCN-222@ICG was determined to have lower cytotoxicity than the unmodified PCN-222 because the ICG has been proved to have excellent biocompatibility. Both PCN-222 and PCN-222@ICG had desirable biocompatibility while PCN-222@ICG was less toxic to the PC12 cells at higher concentrations according to MTT results in Figure 4.7a. In addition, the toxicity of

Aβ42 with PCN-222 and PCN-222@ICG was also determined in PC12 cells. Aβ42 pretreated with PCN-222 and PCN-222@ICG under no irradiation and incubated 24 hours resulted in low cell viability of ~ 40%. However, NIR-activated PCN-222 and PCN-222@ICG were capable of recovering Aβ42-induced cellular toxicity. Such the regulatory activity of PCN-222@ICG toward Aβ42 with 24-hour incubation was more noticeable than that of the PCN-222 alone (Figure 4.7b). Together, the aggregation potency of oxygenated Aβ was markedly lower than that of native Aβ42, which suggests that Aβ oxygenated by photo-irradiated PCN-222@ICG would no longer self-assemble into high molecular weight and remained non-toxic. Live/dead staining was carried out for PC12 cells co-incubated with Aβ before and after the treatment of PCN-222 and PCN-222@ICG under the NIR light irradiation. Figure 4.7c indicated that Aβ treated with NIR activated PCN-222@ICG has lower cytotoxicity to PC12 cells than those treated with PCN-222 alone under the same condition. Not surprisingly, native Aβ caused severe cell death which is consistent with MTT assay.

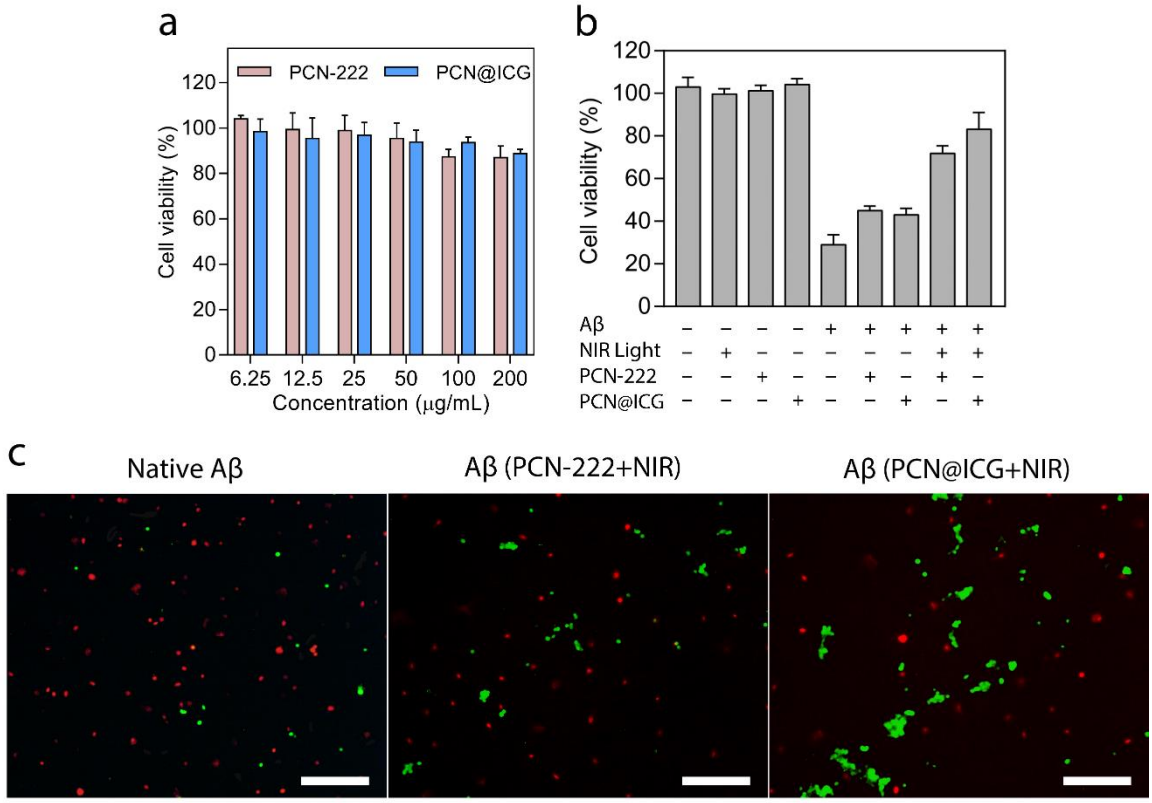

Figure 4.7 (a) Evaluation of cytotoxicity of PCN-222 and PCN-222@ICG to PC12 cells. (b) PC12 cell viability was rescued in the presence of Aβ42 treated by the photo-activated PCN-222 and PCN-222@ICG. (c) Live/dead staining of PC12 cells co-cultured with native Aβ42 and Aβ42 treated with photo-activated PCN-222 and PCN-222@ICG. Scale bar: 200 μm.

4.3.6 Mechanisms exploration of NIR-activated PCN-222@ICG Induced Attenuation of Aβ42 Cytotoxicity

Based on the biochemical, electromicroscopic and spectroscopic studies reported herein, we were able to propose two main mechanisms that may explain the enhanced regulatory activity of PCN-222@ICG toward Aβ42 aggregation. The first possible pathway is photooxygenation-mediated inhibition of Aβ42 aggregation. Several studies have demonstrated that oxygenated Aβ42 did not self-assemble into higher-order cross-β-sheet structure after incubation whereas native Aβ formed robust fibrils[101-104]. To investigate the oxygenation activity of Aβ42, oxygen-atom adducts in the protein were detected by matrix-assisted laser desorption/ionization-time-of-flight mass spectroscopy (MALDI-TOF MS). The oxygenation activity of PCN-222@ICG treated Aβ42 was markedly higher than that of native peptides after 0.5 and 1 h of incubation (**Error! Reference source not found.**Figure 4.8a-c). This finding suggests that the Aβ42 peptide was oxygenated by the $^1O_2$ generated by porphyrin MOF under NIR irradiation. Secondly, the binding of Aβ42 peptide to PCN-222@ICG *via* multiple interactions and the created mild heat under NIR light would facilitate conformational changes in Aβ monomers and thus prohibit the formation of toxic aggregates. Aβ42 may adhere to the PCN-222@ICG nanoprobes and temperature-induced conformational changes in Aβ42 took place under NIR light due to the photothermal

effect of ICG, which could effectively prevent Aβ42-induced damage of the nerve cell membrane.

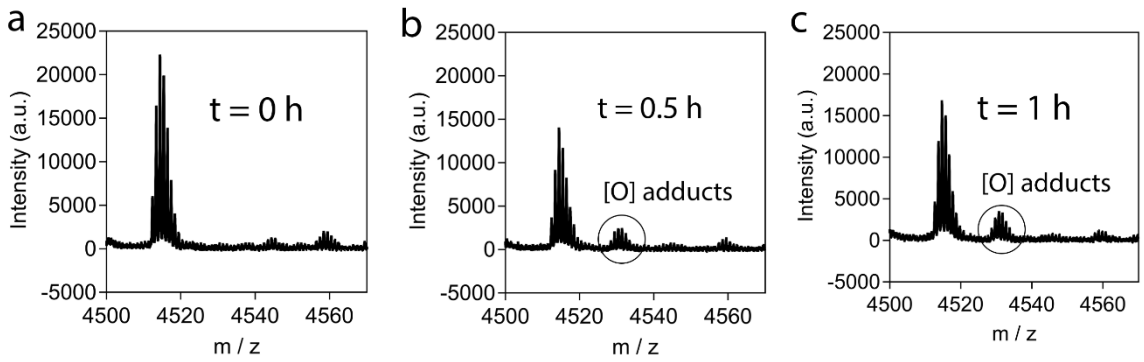

Figure 4.8 MALDI-TOF MS spectra of the Aβ42 before (a) and after the treatment of PCN-222@ICG with photo irradiation for 0.5 h (b) and 1 h (c).

4.3.7 *In vitro* Transwell Model for BBB Permeability Test of RVG Modified PCN-222@ICG

The trans-BBB potential of nanoprobe PCN-222@ICG conjugated with RVG peptide was evaluated in an *in vitro* BBB Transwell model shown in Figure 4.9. The *in vitro* BBB model consists of brain endothelial cells (hCMEC/D3) growing on the apical side of a porous membrane positioned between two compartments and human primary astrocytes and pericytes growing on the other side of the Transwell membrane. 200 μg mL^{-1} of PCN-222@ICG@RVG nanoprobe was added to the apical side of the BBB model and total volume in the basolateral side collected after 6 h of incubation. The translocation rate was quantified by measuring the fluorescence intensity of nanoprobe at 650 nm in the basolateral side. In addition, the integrity of the BBB model was monitored using fluorescein isothiocyanate-conjugated dextran (3, 10, and 70 kDa). The results showed that after 6 h incubation, around 17.4% of 3 kDa and 9.76% of 10 kDa dextran translocated the BBB, being in the basolateral chamber. Only around 1.66% of 70 kDa dextran were able to cross the BBB after 6 h, indicating a tight cell-cell junction forming by the endothelium (Figure 4.9b). A systematic analysis of the peptide-assisted translocation mechanism across an *in vitro* BBB model was achieved

by comparing the permeability of two nanoprobes − PCN-222@ICG and PCN-222@ICG@RVG. Without peptide conjugation, around 2.1% of PCN-222@ICG could translocate to the basal side. However, after RVG conjugation to the PCN-222@ICG, the BBB permeability of RVG-nanoprobe improved significantly with an increase of translocation of 7.29%, 3.4-fold increase compared to the nanoprobe without RVG conjugation (Figure 4.9c).

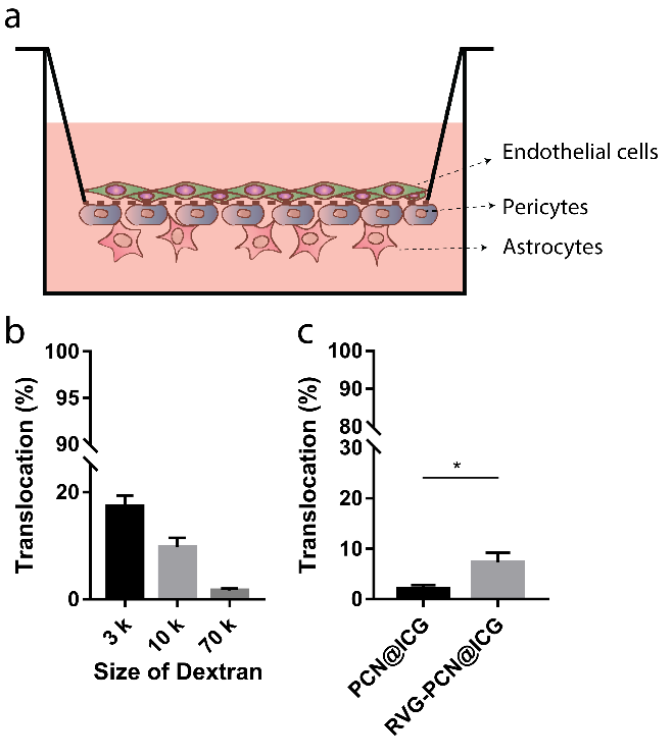

Figure 4.9 Translocation across *in vitro* model of BBB. (a) schematic drawing of the preparation of the *in vitro* blood–brain barrier model. Human primary astrocytes and pericytes were seeded at the against-lumen side of Transwell membranes of inverted cell culture inserts after 4 hours, endothelial cells (hCMEC/D3) were seeded into the luminal compartment of the inserts and positioned into the 24-well plates. (b) percentage of translocation determined by FITC fluorescence intensity measurements, for 0.1 μM of FITC-labelled dextran molecules (3, 10, and 70 kDa) (* $P \leq 0.05$).

4.4 Discussion

In this chapter, a combinational strategy that integrated photooxygenation with photothermal inhibition of the Aβ aggregation has been demonstrated using PCN-222@ICG nanoprobe. Similar to the carbon dots and graphitic carbon nitride (g-C_3N_4), the porphyrin MOF is able to inhibit Aβ aggregation by photooxygenation. Unlike these nanoprobes, however, PCN-222@ICG enhances the inhibition of the Aβ aggregation

by combining NIR-induced photothermal effect. The Transwell model is an effective *in vitro* platform for mimicking the function of BBB and an ideal tool for brain drug testing. With the assistance of RVG peptide, PCN-222@ICG can cross the BBB and function in the central nervous system according to the results of the Transwell model. Transcellular transport is the primary mechanism by which most molecules cross the restrictive barrier such as BBB. This transcellular transport might occur through transcytosis or diffusion, only observed for lipophilic molecules. Transcytosis is the result of endocytosis at the apical membrane and exocytosisat the basolateral membrane[105]. Brain-penetrating peptide enhanced the transcytosis process of nanoprobe, resulting in high accumulation in the brain. Our work may open a new avenue for the design of novel nanoprobes as Aβ inhibitors for the therapy of AD and other neurodegenerative diseases.

5 Human Brain-on-a-chip Enables *in vitro* Alzheimer's Disease Model

5.1 Introduction

Alzheimer's disease (AD) is a serious type of brain disease that has become one of the most expensive diseases in society due to the enormous burden imposed on caregivers[106]. Because AD is an age-related neurodegenerative disease, it has a dramatic increase in the elderly population in developed countries. Due to its severity, AD has become a subject of extensive research on the pathogenesis of diseases and clinical trials of various drugs in both academia and pharmaceutical industrials[107]. Although the study of AD has been continued for more than one hundred years since the first discovery of AD, the main cause of AD and the method for effectively preventing or reversing the disease remain unknown. Several hypotheses about the etiology of AD have been proposed, including genetics, Aβ and tau protein, however, confirming the major cause of AD remains a challenge[108]. Among the hypotheses proposed, Aβ is widely recognized as the leading cause of disease, and various studies of Aβ mechanisms involving the pruning of brain neuronal connections have been performed using *in vivo* animal models and *in vitro* models. However, due to the high cost of animal models, the results of uncertain translations on humans and human-related moral concerns have shown that the demand for extracorporeal brains is constantly increasing to more realistically mimic the brains of the *in vivo* microenvironment model.

Through the convergence of tissue engineering and microfluidics, miniature 3D models (also known as organs-on-a-chip) of various organs have been engineered with the potential to transform the animal model studies[109-115]. By mimicking the milieu of microphysiological factors like vessel microenvironments and cellular and tissue level crosstalk, these models have allowed replication of complex physiologies *in vitro* and

have helped discern their underlying complex molecular pathways. Although many researchers have developed μBBB chip to mimic the physiological microenvironment of blood-brain barrier[116-119], there is no model for the study of the pathophysiological microenvironment of the AD brain. Here, we developed an *in vivo*-mimicking microfluidic AD brain model by co-culturing multiple cell types including endothelial cells, primary human brain astrocytes, pericytes and neurons in the two-channel microchip. Using this AD brain model, we investigated the BBB translocation effect of several nanoprobes and molecules which were developed for Aβ inhibition. Instead of using rat or mouse brain cells, this model used human primary HUVEC, astrocytes, pericytes and neurons, which recapitulates aspects of the human central nervous system (CNS). This AD brain chip model may provide a powerful tool to study neurodevelopment and developmental neurotoxicity of Aβ and evaluate the therapeutic effect of AD drugs.

5.2 Methodology

5.2.1 Device Design and Fabrication

Molds for microfluidic channels with 1 mm, 0.2, and 20 mm in width, height, and length, respectively, were designed with SolidWorks® software. Microfluidic devices were subsequently produced by soft lithography. Briefly, a degassed 10 : 1 base : crosslinking mix of Sylgard 184 polydimethylsiloxane (PDMS, Dow Corning, USA) was poured onto the mold and allowed to crosslink at 65 °C overnight. Inlets and outlets of 1 mm diameter were punched in the molded PDMS and the device was bonded to a 100 μm layer of spin-coated PDMS by pre-treating with oxygen plasma at 35 W for 30 seconds and then pressing the surfaces together. A porous polyester membrane (polyethylene terephthalate, 0.4 μm pores, density 4×10^6 cm^{-2}) was sandwiched between the two microfluidic channels during bonding.

5.2.2 Media for Triple Culture for Brain-on-a-chip

Endothelial media was prepared according to the instructions from ScienCell. The media was based on Endothelial Cell Medium consists of 500 mL of basal medium, 25 mL of FBS, 5 mL of Endothelial Cell Growth Supplement and 5 mL of penicillin/streptomycin solution. Astrocyte Medium consists of 500 mL of basal medium, 10 mL of FBS, 5 ml of Astrocyte Growth Supplement and 5 mL of penicillin/streptomycin solution. Pericyte Medium (ScienCell) consists of 500 mL of basal medium, 10 mL of FBS, 5 mL of Pericyte Growth Supplement (PGS) and 5 mL of penicillin/streptomycin solution.

5.2.3 BBB reconstitution on a chip

The human primary umbilical vein endothelial cell (HUVEC) was propagated on tissue-culture plates that were coated with Matrigel by using extracellular matrix (ECM) media and maintained according to protocols provided by Thermo Fisher Scientific. Primary human astrocytes isolated from the cerebral cortex were obtained from ScienCell and maintained in the Astrocyte medium. Primary human brain pericytes were obtained from ScienCell and maintained in the Pericyte medium. The primary cells were used at passage 3-6. The microfluidic channels were coated with ECM consisted of collagen IV (400 μg ml^{-1}) and fibronectin (100 μg ml^{-1}) overnight. Both channels of the chip were rinsed with PBS three times and then filled with astrocyte media for at least 1 h before seeding cells. For coculturing astrocytes and pericytes in the brain channel of the chip, a density of 0.7×10^6 cells ml^{-1} of human astrocyte and 0.3×10^6 cells ml^{-1} of pericyte were mixed together in the astrocyte media and seeded on the apical channel of the chip, then incubated in the incubator for 1 h. To remove the access of the astrocyte and pericytes, channels of the chip were washed with the endothelial medium. Afterwards, 2.3×10^7 cells ml^{-1} of HUVECs was seeded in the

basal channel, and the device was flipped immediately to allow the HUVECs to adhere to the ECM-coated PET membrane. After 5 h incubation, the device was flipped back to let the rest of HUVECs sit on the bottom and sides of the channel to form a capillary lumen. After 12 h incubation, the chip was connected to a peristaltic pump and endothelial medium was flowed through the channels at a flow rate of 60 μL h^{-1} to allow the chip to adjust to flow conditions. Fluorescence-labelled dextran tracers were dosed through the vascular channels for a known period of time, and the concentration of the dextran tracers in the outlet samples from both vascular and brain channels was determined by using Synergy H1 microplate reader.

5.2.4 Immunofluorescence Staining

Chips were rinsed in pre-warmed phosphate-buffered saline and fixed in 4% paraformaldehyde for 10 minutes to 20 minutes at room temperature. Immunocytochemistry was carried out after permeabilization in phosphate-buffered saline with 0.05 – 0.1% Triton X-100 (Sigma-Aldrich) and blocking for 30 minutes in 3 – 5% Bovine Serum Albumin (BSA) or 10% goat serum in phosphate-buffered saline with 0.05 – 0.1% Triton X-100. Primary antibodies were applied in 2% goat serum or 0.5% BSA overnight at 4 °C or at room temperature for 1.5 h. The following primary antibodies were used for immunocytochemistry experiments: rabbit anti-glial fibrillary acidic protein (GFAP) (Invitrogen, 1:100), mouse anti-vascular endothelial (VE)-cadherin (Abcam, 1:100), anti-glial fibrillary acidic protein (GFAP, Abcam, 1:200). Cells were washed three times in phosphate-buffered saline with 0.05 – 0.1% BSA, followed by staining with secondary antibody for 30 – 60 min at room temperature. The secondary antibodies were anti-rabbit, anti-goat or anti-mouse IgG conjugated with Alexa Fluor-488, Alexa Fluor-555, or Alexa Fluor-647 (Invitrogen). Hoechst (10 mg/ml, Invitrogen) was used at a dilution of 1:5000 for nuclei staining. For staining of

F-actin, Alexa Fluor-647-phalloidin (Invitrogen) were used at a dilution of 1:50. ProLong Gold Antifade reagent (Invitrogen) was added to preserve the samples and glass coverslips are affixed using transparent nail polish. Prepared slides were either imaged immediately or stored at 4 ºC. Imaging was carried out on a Nikon Eclipse Ti2-E Live-cell Fluorescence Imaging System or Leica TCS SPE Confocal Microscope.

5.2.5 BBB permeability of Peptide-modified MOFs and Carbon Nanodots

For the BBB permeability assay, 10 μg ml^{-1} of peptide-modified PCN-222@ICG nanosheets and carbon nanodots (CDs) was flowed to the brain endothelial channel at 60 μl h^{-1} for 3, 6, 12, and 24 h, and the effluents were collected for the analysis. RVG peptide (YTIWMPENPRPGTPCDIFTNSRGKRASNGC) was purchased through the custom peptide synthesis service of GL Biochem (China). RVG peptide was incubated with 200 ug ml^{-1} of PCN-224 nanoparticles, PCN-222@ICG nanosheets and CDs overnight at room temperature. The unbound peptides were removed through centrifugation. The fluorescent intensity of effluent was measured using a Synergy H1 microplate reader, and the nanomaterials were quantified to calculate the *Papp* (cm s^{-1}). For the PCN-222@ICG and CDs analysis, 415/650 and 400/650 nm wavelength were used respectively. Papp was calculated according to the following equation:

$$P_{app} = \frac{V_r \times C_r}{A \times t \times \frac{(C_d \times V_d + C_r \times V_r)}{V_d + V_r}}$$

Where, V_r is the volume of receiving channel effluent after time *t*. V_d is the volume of dosing channel effluent after time *t*. *A* is the area of membrane. *Cr* is the measured concentration of tracer in receiving channel effluent. C*d* is the measured concentration of tracer in dosing channel effluent.

5.3 Results

5.3.1 Reconstitution of Human AD Brain-on-a-chip

Human AD brain-on-a-chip was created through soft lithography using optically clear poly(dimethylsiloxane) (PDMS) and 3D-printed molds. The upper layers containing a 2 cm long × 1 mm wide × 1 mm high channel mimicked CNS while the lower layer with a 2 cm long × 1 mm wide × 0.2 mm high microchannel mimicked blood vessel. A porous (2 μm diameter), polyethylene terephthalate (PET) membrane was sandwiched between the two PDMS layers (Figure 5.1a). Extracellular matrix which composed of collagen type IV and fibronectin was coated on both sides overnight. Both channels of the chip were rinsed with PBS three times and then filled with astrocyte media for at least 1 h before seeding cells. Twenty-three million of HUVECs cells were detached from cell culture plates and seeded on the bottom channel of the microfluidic chip in the endothelial medium. The chips were flipped over to induce adhesion of HUVECs to the membrane. After 5 h incubation, the chips were flipped back to let the rest of HUVECs attach on the bottom and sides of the channel to form a capillary lumen. Then, a mixture of primary human brain astrocytes and pericytes (seeding ratio of 7:3) were then cultured in the astrocyte medium on the PET membrane in the upper channel under static conditions for at least 2 h before attaching to a peristaltic pump. Biocompatible tubings (PharmMed®) were connected to the inlets and outlets of the chips to maintain a continuous medium flow of 60 μL h^{-1}. Figure 5.1d displays the cross-section of the microchip channel with multiple cells including endothelial cells, astrocytes, pericytes and Aβ peptides. Astrocytes and pericytes were co-cultured in the upper channel, while HUVECs were cultured on the four sides of the bottom channel to mimic the brain blood vessel.

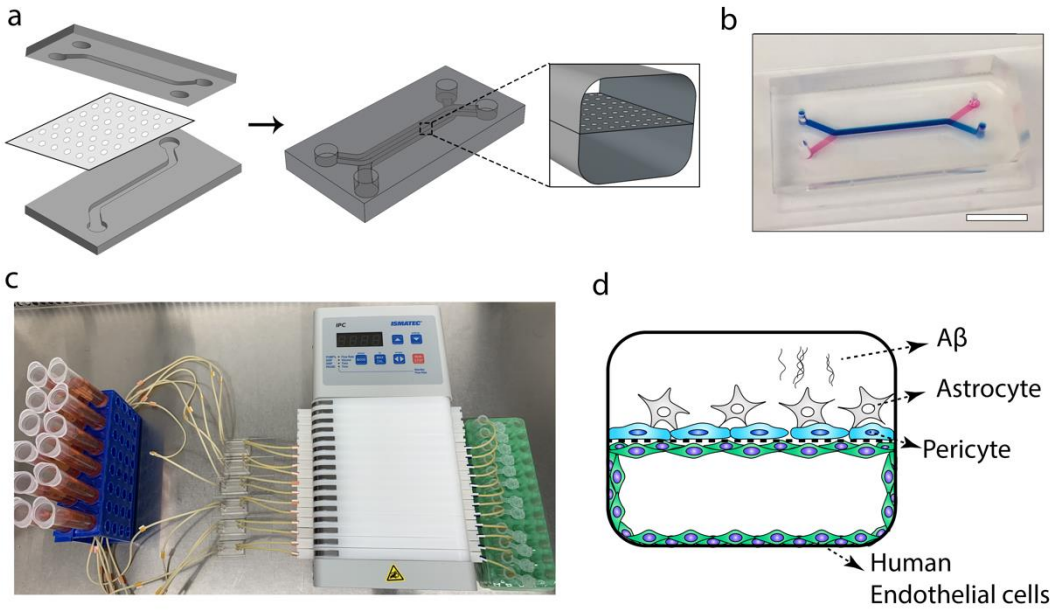

Figure 5.1 (a) fabrication process of two-channel AD brain chip. (b) blue and red ink represent upper and lower channels, respectively. Scale bar: 10 mm (c) cell media flowed through the brain chip channel driven by a peristaltic pump. (d) schematic drawings Alzheimer's brain chip. Endothelial cells were seeded in the bottom channel while astrocytes, pericytes were seeded in the upper channel. Aβ peptide was also added to the upper channel to induce an AD brain environment.

5.3.2 Characterization of Brain-on-a-chip

To let the cells firmly attached to the membrane of the chip, extracellular matrix consisted of collagen IV (400 μg mL^{-1}) and fibronectin (100 μg mL^{-1}) was coated on both channel of chip. For coculturing astrocytes and pericytes in the brain channel of the chip, a density of 0.7×10^6 cells mL^{-1} of human astrocyte and 0.3×10^6 cells mL^{-1} of pericyte were mixed together in the astrocyte media and seeded on the apical channel of the chip. Twenty-three million of HUVECs cells were detached from cell culture plates and seeded on the bottom channel of the microfluidic chip in endothelial medium. The HUVECs attached to the bottom side of the membrane by flipped over and incubated for 5 h. Astrocytes, pericytes in the apical channel and HUVECs in the lower were observed under an optical microscope. Astrocytes and pericytes sit in the channel bent to the right in the Figure 5.2a. Due to the high density of HUVEC population in the lower channel, Figure 5.2b showed clear cell-cell boundary of monolayered HUVECs. Confocal immunofluorescence microscopic analysis of the cells was

performed after 24 h of microfluidic culture. Astrocytes stained with GFAP (green) and DAPI (blue) were displayed in the Figure 5.2c. The cell-cell tight junction of HUVEC cells is critical for mimicking the *in-vivo* like blood vessel. As shown in the Figure 5.2d, these HUVECs formed well-developed tight junctions and expressed high levels of protein ZO-1 which is a marker that widely used to identify tight junctions between adjacent endothelial cells[120]. The cell boundaries of HUVECs immuno-stained with anti ZO-1 (green) in the Figure 5.2d demonstrated the well-formed tight junctions of HUVECs. The images of immunocytochemistry of the whole brain chip were showed in the Figure 5.2e-f. The results showed that HUVECs stained with the phalloidin formed a uniform monolayer on the blood side, while the astrocytes express GFAP and pericytes formed an intricate network within the brain compartment.

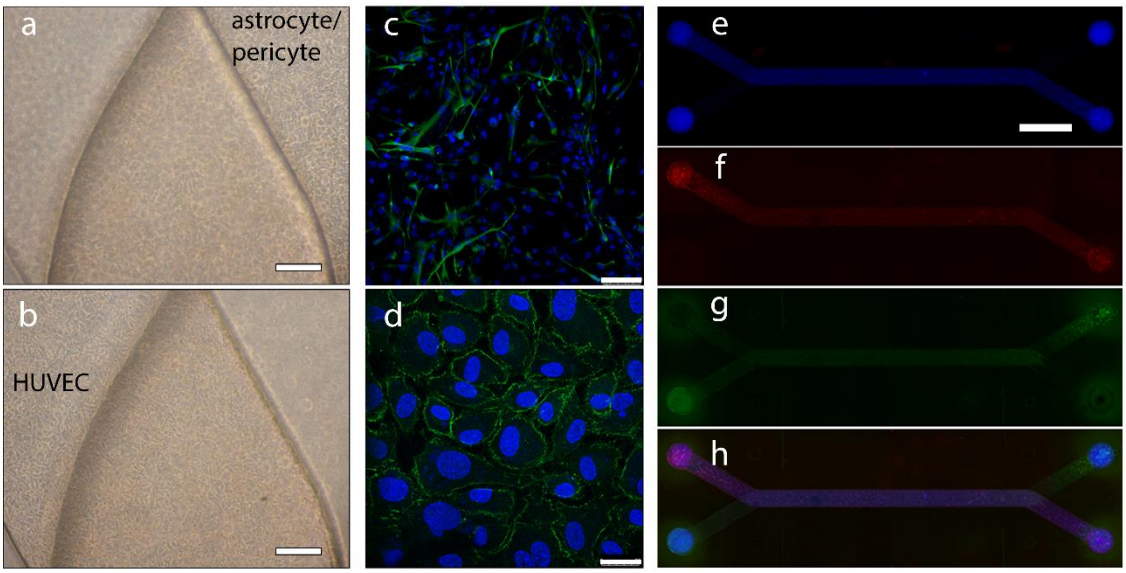

Figure 5.2 Characterization of brain chip. Optical microscopic images of upper (a) and lower (b) channel. Scare bar: 100 μm. (c) Immunofluorescence staining of astrocytes. Green: GFAP, blue: DAPI. Scare bar: 100 μm (d) Immunofluorescence micrographic views of the human brain microvascular endothelium cultured on-chip viewed from above demonstrating high levels of expression of tight junction protein ZO-1 (green). Scare bar: 25 μm (e-f) The imaging of immunocytochemistry of the brain chip. Blue: DAPI (nucleus), red: GFAP (astrocyte), green: phalloidin (HUVEC). Scare bar: 2.5 mm.

To examine the organ-level functionality of our brain model, tumor necrosis factor α (TNF-α) was perfused through the blood compartment for 12 h. Not

surprisingly, the response to inflammatory stimulation reduced the expression of the tight-junction marker ZO-1. Figure 5.3 showed that the well-formed cell-cell boundary was damaged by the inflammation after the treatment with 100 ng ml^{-1} of TNF-α. This damage consequently led to a dose-dependent increase in blood-to-brain leakage of dextran (Figure 5.4a-c).

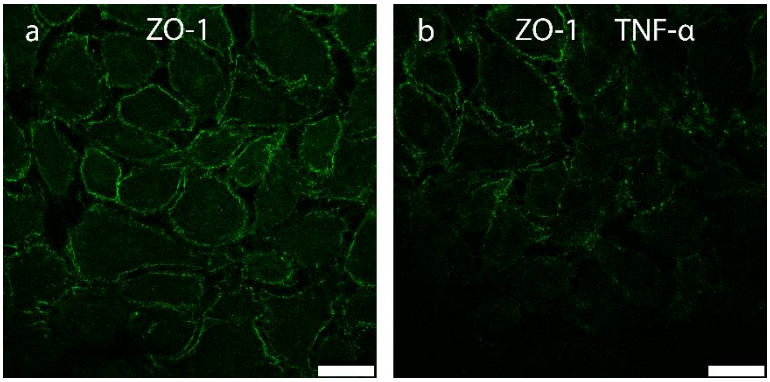

Figure 5.3 Immunofluorescence staining of HUVECs. (a) HUVECs cell-cell junctions stained for ZO-1 (green). (b) HUVECs treated with 100 ng ml^{-1} of TNF-α. Scare bar: 25 μm.

To investigate the barrier integrity of our brain model, the fluorescently labeled dextran tracers (3, 10, 70 kDa) were perfused into the blood channel for 12 h. The results showed that the apparent permeability (P_{app}) of the *in-vitro* BBB lined by HUVECs, astrocytes and pericytes was found very low when we measured the concentration of dextran in the brain channel. The P_{app} value inversely correlated with the size of the tracer (average P_{app} = 1.55×10^{-7} cm s^{-1}, 1.98×10^{-8} cm s^{-1}, 3.45×10^{-9} cm s^{-1} for 3, 10, 70 kDa dextran, respectively). However, The P_{app} value largely increased to 1.8×10^{-6} cm s^{-1}, 2.25×10^{-7} cm s^{-1}, 3.41×10^{-7} cm s^{-1} for 3, 10, 70 kDa dextran when the HUVECs treated with 100 ng ml^{-1} of TNF-α. After the damage of endothelium caused by the TNF-α-induced inflammation, the permeability of 70 kDa dextran increased to a similar level of 10 kDa dextran according to Figure 5.4b. The relative ZO-1 expression displayed a concentration-dependent decreased after treating with TNF-α, which was consistent with the immunofluorescence microscopic analysis in the

Figure 5.3 that showed the loss of tight junctions between HUVEC cells. Taken together, these results demonstrated this brain chip recapitulated in-vivo like brain microenvironment and functions that resemble the interface of the NVU.

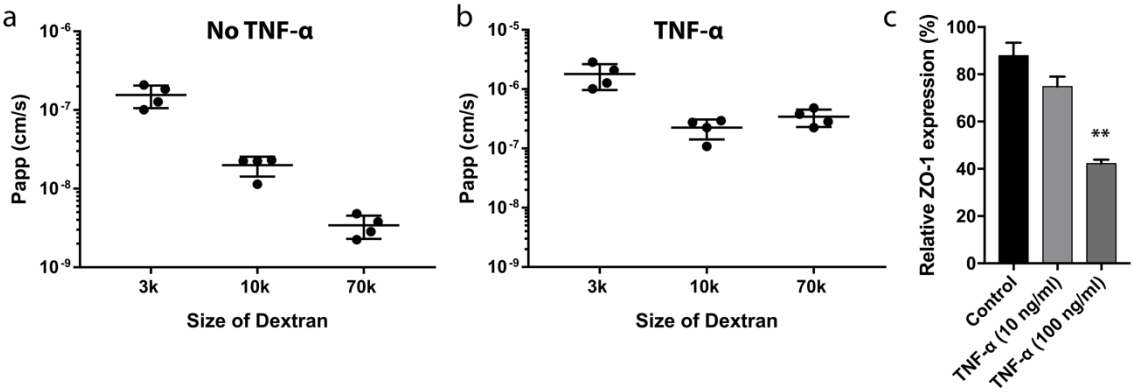

Figure 5.4 Permeability of dextran tracers of various sizes in the brain chips. Fluorophore-labelled dextran molecules (3, 10, or 70 kDa) were flowed through the brain channel on the chips for 6 h. Endothelium treated without (a) and with (b) 100 ng ml^{-1} of TNF-α. (c) TNF-α treatment of the endothelium results reduction of the relative ZO-1 expression. (**p < 0.01; one-way ANOVA with Dunnett's multiple comparisons test, n=3-6)

5.3.3 BBB-shuttling Activities of Nanoprobes On-chip

It is reported that the BBB prevents the transportation of nearly all the drugs that larger than 500 Da and antibodies around 150 kDa into brain. Thus, many drugs that developed for brain diseases suffered from the difficulty of being delivered across BBB to NVU. Several brain shuttling molecules have been identified including brain-targeting peptides[121], IgG[122] antibodies, ligands that target the cell surface receptors on brain endothelium to facilitate the receptor-mediated transcytosis. Previous *in vitro* human BBB models built by Transwell were not suitable for the evaluation the CNS-targeted drug delivery efficacy because it required the *in vitro* model to provide a reliable physiological barrier to prevent cell leakage, as well as brain endothelium-specific receptors and transporter expression. As we have developed this human brain model *via* triple culture, we explored whether this improved model can be used to directly assess the human BBB penetrating capacity of MOF-based nanomedicines and carbon dots that we have developed for the inhibition of Aβ aggregation *in vitro*.

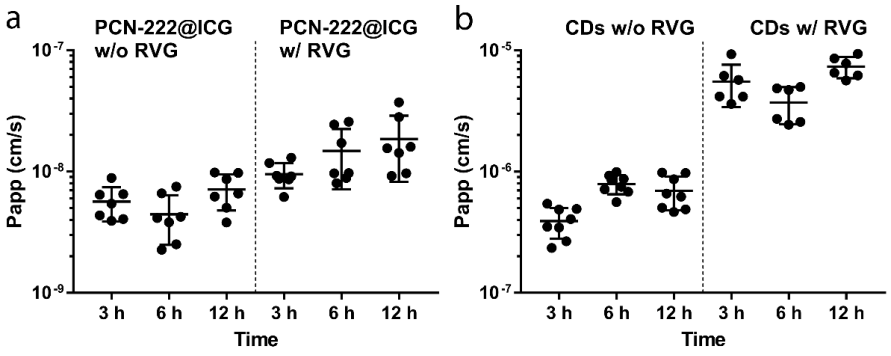

Figure 5.5 Permeability of carbon dots (CDs) and PCN-222@ICG with/ without RVG modification in the brain chips.

The 29 amino-acid brain-targeting peptide termed RVG, which was derived from rabies virus glycoprotein, has been shown to penetrate the BBB *in vitro* and *in vivo*[123]. To investigate the brain penetrating capacity of RVG modified PCN-222@ICG and carbon dots using the model we established, PCN-222@ICG@RVG nanosheets (< 100 nm) and CDs@RVG (< 4 nm) were flowed through the endothelium-lined vascular channel of the human brain chip. The PCN-222@ICG nanosheet without RVG modification has a very low BBB penetration capability into the CNS channel. It is probably due to the large size and positive charge nature which might resist endocytosis process. However, the PCN-222@ICG nanosheet with RVG modification exhibited approximately 2.6-fold greater capacity to enter the CNS channel, indicating that RVG peptide effectively assisted the translocation of the nanosheet across the BBB, although the overall BBB penetration capability was still very low. For carbon nanodots, the BBB permeability was seen a significant increase compared to larger size PCN-222@ICG, which was mainly attributed to the small size and positive surface charge of CDs. Similar to the PCN-222@ICG@RVG, CDs@RVG also displayed a dramatically increased penetration through the BBB and into the CNS channel. Approximately 10-fold greater *Papp* value was observed when comparing the CDs with CDs@RVG after 12 h flowing. Furthermore, while both PCN-222@ICG and PCN-222@ICG@RVG

exhibited an increase from 3 h to 12 h of flowing, we did not observe any significant difference in transcytosis ability in different time slots between CDs and CDs@RVG.

5.4 Discussion

The BBB strictly regulates the transportation of molecules between the blood and CNS. The study of BBB in health and disease and the development of neurological diseases drugs are hampered due to the lack of reliable *in vitro* brain model. Recently, many nanomedicines have been developed as Aβ inhibitors for the therapy of Alzheimer's disease, but whether these nanomaterials are able to penetrate the BBB is still a concern. Here, we use a simple microfluidic chip that contains two channels separated by a porous membrane, allowing the reconstitution of multicellular architectures and tissue-tissue interfaces. HUVECs, human primary astrocytes, and pericytes were co-cultured in the chips that recapitulated human-relevant physiological BBB properties. Although other previous work in this field has described human BBB models using Transwell and single channel microfluidic devices, none of them used triple culture model nor studied the BBB permeability of nanoprobes. The brain chip was created by culturing HUVECs under physiological flow to enable the interaction with human astrocytes and pericytes, thus exhibiting enhanced functionality of *in vitro* BBB. These functionalities provide long-term improvements resulting in the formation of stable BBB with high, *in vivo*-like permeability restriction that lasts up to several days. Immunochemistry analysis revealed the high level of expression of tight junction protein ZO-1; RVG peptide modified PCN-222@ICG and CDs showed enhanced transcytosis capabilities. This *in-vivo* level brain chip can be used as a preclinical drug development tool to discover new BBB shuttles and Alzheimer's disease-targeted drugs and vehicles.

6 Conclusion

In this thesis, we first synthesized ultrasmall Zn-MOF-74 nanodots (< 5 nm in diameter) and demonstrated a novel colorimetric sensing platform for highly selective detection of Fe^{3+} in aqueous solutions based on the Zn-MOF-74 nanodots. We downsized the Zn-MOF-74 by manipulating the initial conditions within a diluted material system under a mile temperature. Unlike the bulk-sized MOF material might lead to a slow response with a relatively small surface reaction area for Fe^{3+} sensing, this Zn-MOF-74 nanodots showed a fast response for the color change upon the addition of Fe^{3+}. Also, bulk-sized MOF material usually has poor dispersity and stability in aqueous solution, which largely hampers the application for ion sensing. However, the Zn-MOF-74 nanodots are very stable and can be well dispersed in water for several days with no obvious aggregation or precipitation. These properties allow Zn-MOF-74 nanodots to be an excellent ion sensor in aqueous solution. The high surface area of Zn-MOF-74 nanodots also leads to a high sensing sensitivity and broad liner range because of large amount of surface reaction sites within the framework. The selectivity of this Zn-MOF-74 nanodots based sensor for Fe^{3+} ion detection was also demonstrated by comparing against other common metal ions. In general, MOF based sensors are superior in many aspects comparing to other nanomaterial-based sensors such as gold nanoparticles, graphene oxide, iron oxide nanoparticles, *etc*. MOFs have numerous amounts of nanopores in the structure, which provide tremendous opportunities for reactions between analytes and MOFs, resulting in a high sensitivity for detection. MOFs usually are very stable in many different kinds of buffers and wide range of pH solutions, which makes them excellent candidates for ion sensing in industrial settings where analytes may be in more complex conditions. The ease of large-scale production of MOFs at low cost foresees a promising future in industrial application.

We then developed two porphyrin MOFs − PCN-224 nanoparticles and PCN-222@ICG nanosheet by integrating zirconium and tetra-kis(4-carboxyphenyl)porphyrin (TCPP) to form MOF structure. PCN-224 incorporates photosensitizers in periodic arrays, significantly reducing quenching of excited energy in a minimal volume, while allowing the accessibility of substrates due to their porous features. The porphyrin MOF structure showed strong light-to-oxygen generation capability due to the high percentage of exposed TCPP ligands in the framework and easy diffusion of molecular oxygen through the porous structure. In this regard, PCN-224 can be used as photo-inhibitor to prevent Aβ monomer from aggregating into toxic oligomers and fibrils. Unlike the other nanomaterials which use visible light to generate $^1O_2$, this PCN-224 uses NIR light to suppress Aβ aggregation. We also synthesized 2D PCN-222 nanosheet and incorporate ICG into the framework. While PCN-222 transfers NIR light into $^1O_2$, ICG absorbs NIR light to generate thermal which also inhibit the Aβ aggregation. This is the first time a synergistic approach of inhibiting Aβ aggregation by a hybrid nanosystem has been demonstrated. An *in vitro* BBB model based on Transwell was also built and used as an effective tool for the examination of the BBB permeability of PCN-222@ICG. With this Transwell model cultured with endothelial cells, human astrocytes, and pericytes, we were able to determine whether the RVG modified PCN-222@ICG can penetrate BBB. Using MOFs as photo induced Aβ aggregation inhibitors is a novel approach for the photo-treatment of Alzheimer's disease. Other nanomaterials such as carbon nanodot has similar efficacy for the inhibition of AD but the visible light absorbance limits its application in clinical settings. PCN MOFs, however, absorb tissue-penetrative NIR light to produce singlet oxygen due to the porphyrin in the center of the ligand. Moreover, the organic ligands of MOFs usually contain plenty of free chemical groups both inside and outside the

framework structure. These functional groups are easily to be used to modify BBB shuttles such as peptides, antibodies to transport the MOFs to the brain.

Finally, an Alzheimer's disease brain-on-a-chip model was developed using microfluidic techniques. Many drugs that are designed for AD are suffering from unavailability of *in vitro* AD models for testing, as the animal models are highly costly and the results of translations on humans are uncertain. We developed an *in vivo*-mimicking microfluidic AD brain model by co-culturing triple cells − endothelial cells, primary human brain astrocytes, pericytes and neurons in a two-channel microfluidic chip. Using this AD brain model, we investigated the BBB translocation effect of two nanoprobes which were developed for Aβ inhibition − PCN-222@ICG nanosheet and carbon dots. This AD brain chip model provided a powerful tool to study neurodevelopment and developmental neurotoxicity of Aβ and evaluate the therapeutic effect of AD drugs.

Reference

1. Zhou, H. C.; Long, J. R.; Yaghi, O. M., Introduction to Metal-Organic Frameworks. *Chem Rev* **2012**, *112*, 673-4.

2. Zhu, Q. L.; Xu, Q., Metal-Organic Framework Composites. *Chem Soc Rev* **2014**, *43*, 5468-512.

3. Li, H.; Eddaoudi, M.; O'Keeffe, M.; Yaghi, O. M., Design and Synthesis of an Exceptionally Stable and Highly Porous Metal-Organic Framework. *Nature* **1999**, *402*, 276-279.

4. Kitagawa, S.; Kitaura, R.; Noro, S.-i., Functional Porous Coordination Polymers. *Angewandte Chemie International Edition* **2004**, *43*, 2334-2375.

5. Chen, T. H.; Popov, I.; Kaveevivitchai, W.; Miljanic, O. S., Metal-Organic Frameworks: Rise of the Ligands. *Chemistry of Materials* **2014**, *26*, 4322-4325.

6. He, T.; Ni, B.; Zhang, S.; Gong, Y.; Wang, H.; Gu, L.; Zhuang, J.; Hu, W.; Wang, X., Ultrathin 2d Zirconium Metal-Organic Framework Nanosheets: Preparation and Application in Photocatalysis. *Small* **2018**, *14*, e1703929.

7. Cheetham, A. K.; Rao, C.; Feller, R. K., Structural Diversity and Chemical Trends in Hybrid Inorganic–Organic Framework Materials. *Chemical communications* **2006**, 4780-4795.

8. Klinowski, J.; Paz, F. A. A.; Silva, P.; Rocha, J., Microwave-Assisted Synthesis of Metal–Organic Frameworks. *Dalton Transactions* **2011**, *40*, 321-330.

9. Haque, E.; Khan, N. A.; Park, J. H.; Jhung, S. H., Synthesis of a Metal–Organic Framework Material, Iron Terephthalate, by Ultrasound, Microwave, and Conventional Electric Heating: A Kinetic Study. *Chemistry – A European Journal* **2010**, *16*, 1046-1052.

10. Sonnauer, A.; Stock, N., High-Throughput and Microwave Investigation of Rare Earth Phosphonatoethanesulfonates—Ln (O3p–C2h4–So3)(Ln= Ho, Er, Tm, Yb, Lu, Y). *Journal of Solid State Chemistry* **2008**, *181*, 3065-3070.

11. Choi, J.-S.; Son, W.-J.; Kim, J.; Ahn, W.-S., Metal–Organic Framework Mof-5 Prepared by Microwave Heating: Factors to Be Considered. *Microporous and Mesoporous Materials* **2008**, *116*, 727-731.

12. Carné-Sánchez, A.; Imaz, I.; Cano-Sarabia, M.; Maspoch, D., A Spray-Drying Strategy for Synthesis of Nanoscale Metal–Organic Frameworks and Their Assembly into Hollow Superstructures. *Nature Chemistry* **2013**, *5*, 203.

13. Shang, W.; Kang, X.; Ning, H.; Zhang, J.; Zhang, X.; Wu, Z.; Mo, G.; Xing, X.; Han, B., Shape and Size Controlled Synthesis of Mof Nanocrystals with the Assistance of Ionic Liquid Mircoemulsions. *Langmuir* **2013**, *29*, 13168-13174.

14. Faustini, M.; Kim, J.; Jeong, G.-Y.; Kim, J. Y.; Moon, H. R.; Ahn, W.-S.; Kim, D.-P., Microfluidic Approach toward Continuous and Ultrafast Synthesis of Metal–Organic Framework Crystals and Hetero Structures in Confined Microdroplets. *Journal of the American Chemical Society* **2013**, *135*, 14619-14626.

15. Bechelany, M.; Drobek, M.; Vallicari, C.; Abou Chaaya, A.; Julbe, A.; Miele, P., Highly Crystalline Mof-Based Materials Grown on Electrospun Nanofibers. *Nanoscale* **2015**, *7*, 5794-5802.

16. Hao, Z.; Song, X.; Zhu, M.; Meng, X.; Zhao, S.; Su, S.; Yang, W.; Song, S.; Zhang, H., One-Dimensional Channel-Structured Eu-Mof for Sensing Small Organic Molecules and Cu 2+ Ion. *Journal of Materials Chemistry A* **2013**, *1*, 11043-11050.

17. Zhou, Y.; Chen, H. H.; Yan, B., An Eu3+ Post-Functionalized Nanosized Metal-Organic Framework for Cation Exchange-Based Fe3+-Sensing in an Aqueous Environment. *Journal of Materials Chemistry A* **2014**, *2*, 13691-13697.

18. Chen, Z.; Sun, Y.; Zhang, L.; Sun, D.; Liu, F.; Meng, Q.; Wang, R.; Sun, D., A Tubular Europium-Organic Framework Exhibiting Selective Sensing of Fe3+ and Al3+ over Mixed Metal Ions. *Chemical Communications* **2013**, *49*, 11557-11559.

19. Shustova, N. B.; Cozzolino, A. F.; Reineke, S.; Baldo, M.; Dincă, M., Selective Turn-on Ammonia Sensing Enabled by High-Temperature Fluorescence in Metal–Organic Frameworks with Open Metal Sites. *Journal of the American Chemical Society* **2013**, *135*, 13326-13329.

20. Li, Y.; Zhang, S.; Song, D., A Luminescent Metal–Organic Framework as a Turn-on Sensor for Dmf Vapor. *Angewandte Chemie International Edition* **2013**, *52*, 710-713.

21. Guo, H.; Zhu, Y.; Qiu, S.; Lercher, J. A.; Zhang, H., Coordination Modulation Induced Synthesis of Nanoscale Eu1-Xtbx-Metal-Organic Frameworks for Luminescent Thin Films. *Advanced Materials* **2010**, *22*, 4190-4192.

22. Feijó de Melo, E.; Santana, N. d. C.; Bezerra Alves, K. G.; de Sá, G. F.; Pinto de Melo, C.; Rodrigues, M. O.; Júnior, S. A., Lnmof@Pva Nanofiber: Energy Transfer and Multicolor Light-Emitting Devices. *Journal of Materials Chemistry C* **2013**, *1*, 7574-7581.

23. Dincă, M.; Long, J. R., Strong H2 Binding and Selective Gas Adsorption within the Microporous Coordination Solid Mg3(O2c-C10h6-Co2)3. *Journal of the American Chemical Society* **2005**, *127*, 9376-9377.

24. Llewellyn, P. L.; Bourrelly, S.; Serre, C.; Filinchuk, Y.; Férey, G., How Hydration Drastically Improves Adsorption Selectivity for Co2 over Ch4 in the Flexible Chromium Terephthalate Mil-53. *Angewandte Chemie International Edition* **2006**, *45*, 7751-7754.

25. Saha, D.; Bao, Z.; Jia, F.; Deng, S., Adsorption of Co2, Ch4, N2o, and N2 on Mof-5, Mof-177, and Zeolite 5a. *Environmental Science & Technology* **2010**, *44*, 1820-1826.

26. Davis, M. E., New Vistas in Zeolite and Molecular Sieve Catalysis. *Accounts of chemical research* **1993**, *26*, 111-115.

27. Lee, J.; Farha, O. K.; Roberts, J.; Scheidt, K. A.; Nguyen, S. T.; Hupp, J. T., Metal-Organic Framework Materials as Catalysts. *Chem Soc Rev* **2009**, *38*, 1450-9.

28. Vermoortele, F.; Bueken, B.; Le Bars, G. l.; Van de Voorde, B.; Vandichel, M.; Houthoofd, K.; Vimont, A.; Daturi, M.; Waroquier, M.; Van Speybroeck, V., Synthesis Modulation as a Tool to Increase the Catalytic Activity of Metal–Organic Frameworks: The Unique Case of Uio-66 (Zr). *Journal of the American Chemical Society* **2013**, *135*, 11465-11468.

29. Mondloch, J. E., et al., Vapor-Phase Metalation by Atomic Layer Deposition in a Metal–Organic Framework. *Journal of the American Chemical Society* **2013**, *135*, 10294-10297.

30. Tan, H.; Tang, G.; Wang, Z.; Li, Q.; Gao, J.; Wu, S., Magnetic Porous Carbon Nanocomposites Derived from Metal-Organic Frameworks as a Sensing Platform for DNA Fluorescent Detection. *Analytica Chimica Acta* **2016**, *940*, 136-142.

31. Rocha, J.; Brites, C. D. S.; Carlos, L. D., Lanthanide Organic Framework Luminescent Thermometers. *Chemistry – A European Journal* **2016**, *22*, 14782-14795.

32. Yang, S.-P.; Chen, S.-R.; Liu, S.-W.; Tang, X.-Y.; Qin, L.; Qiu, G.-H.; Chen, J.-X.; Chen, W.-H., Platforms Formed from a Three-Dimensional Cu-Based Zwitterionic Metal–Organic Framework and Probe Ss-DNA: Selective Fluorescent Biosensors for Human Immunodeficiency Virus 1 Ds-DNA and Sudan Virus Rna Sequences. *Analytical Chemistry* **2015**, *87*, 12206-12214.

33. Wang, H.-S.; Li, J.; Li, J.-Y.; Wang, K.; Ding, Y.; Xia, X.-H., Lanthanide-Based Metal-Organic Framework Nanosheets with Unique Fluorescence Quenching Properties for Two-Color Intracellular Adenosine Imaging in Living Cells. *Npg Asia Materials* **2017**, *9*, e354.

34. Zhu, Q.; Chen, Y.; Wang, W.; Zhang, H.; Ren, C.; Chen, H.; Chen, X., A Sensitive Biosensor for Dopamine Determination Based on the Unique Catalytic Chemiluminescence of Metal–Organic Framework Hkust-1. *Sensors and Actuators B: Chemical* **2015**, *210*, 500-507.

35. Yang, W.; Zhang, G.; Weng, W.; Qiu, B.; Guo, L.; Lin, Z.; Chen, G., Signal on Fluorescence Biosensor for Mmp-2 Based on Fret between Semiconducting Polymer Dots and a Metal Organic Framework. *RSC Advances* **2014**, *4*, 58852-58857.

36. Tan, H.; Ma, C.; Li, Q.; Wang, L.; Xu, F.; Chen, S.; Song, Y., Functionalized Lanthanide Coordination Polymer Nanoparticles for Selective Sensing of Hydrogen Peroxide in Biological Fluids. *Analyst* **2014**, *139*, 5516-5522.

37. Wang, H.-S.; Bao, W.-J.; Ren, S.-B.; Chen, M.; Wang, K.; Xia, X.-H., Fluorescent Sulfur-Tagged Europium(Iii) Coordination Polymers for Monitoring Reactive Oxygen Species. *Analytical Chemistry* **2015**, *87*, 6828-6833.

38. Wang, Q.; Yang, Y.; Gao, F.; Ni, J.; Zhang, Y.; Lin, Z., Graphene Oxide Directed One-Step Synthesis of Flowerlike Graphene@Hkust-1 for Enzyme-Free Detection of Hydrogen Peroxide in Biological Samples. *ACS Applied Materials & Interfaces* **2016**, *8*, 32477-32487.

39. Dai, H.; Lü, W.; Zuo, X.; Zhu, Q.; Pan, C.; Niu, X.; Liu, J.; Chen, H.; Chen, X., A Novel Biosensor Based on Boronic Acid Functionalized Metal-Organic Frameworks for the Determination of Hydrogen Peroxide Released from Living Cells. *Biosensors and Bioelectronics* **2017**, *95*, 131-137.

40. Li, Y.-A.; Zhao, C.-W.; Zhu, N.-X.; Liu, Q.-K.; Chen, G.-J.; Liu, J.-B.; Zhao, X.-D.; Ma, J.-P.; Zhang, S.; Dong, Y.-B., Nanoscale Uio-Mof-Based Luminescent Sensors for Highly Selective Detection of Cysteine and Glutathione and Their Application in Bioimaging. *Chemical Communications* **2015**, *51*, 17672-17675.

41. Gao, X.; Wang, Y.; Ji, G.; Cui, R.; Liu, Z., One-Pot Synthesis of Hierarchical-Pore Metal–Organic Frameworks for Drug Delivery and Fluorescent Imaging. *CrystEngComm* **2018**, *20*, 1087-1093.

42. deKrafft, K. E.; Xie, Z.; Cao, G.; Tran, S.; Ma, L.; Zhou, O. Z.; Lin, W., Iodinated Nanoscale Coordination Polymers as Potential Contrast Agents for Computed Tomography. *Angewandte Chemie International Edition* **2009**, *48*, 9901-9904.

43. Lei, P.; An, R.; Zhang, P.; Yao, S.; Song, S.; Dong, L.; Xu, X.; Du, K.; Feng, J.; Zhang, H., Ultrafast Synthesis of Ultrasmall Poly(Vinylpyrrolidone)-Protected Bismuth Nanodots as a Multifunctional Theranostic Agent for in Vivo Dual-Modal Ct/Photothermal-Imaging-Guided Photothermal Therapy. *Adv Funct Mater* **2017**, *27*, 1702018.

44. deKrafft, K. E.; Boyle, W. S.; Burk, L. M.; Zhou, O. Z.; Lin, W., Zr- and Hf-Based Nanoscale Metal–Organic Frameworks as Contrast Agents for Computed Tomography. *Journal of Materials Chemistry* **2012**, *22*, 18139-18144.

45. Wang, Y.-M.; Liu, W.; Yin, X.-B., Self-Limiting Growth Nanoscale Coordination Polymers for Fluorescence and Magnetic Resonance Dual-Modality Imaging. *Adv Funct Mater* **2016**, *26*, 8463-8470.

46. Liu, D.; He, C.; Poon, C.; Lin, W., Theranostic Nanoscale Coordination Polymers for Magnetic Resonance Imaging and Bisphosphonate Delivery. *Journal of Materials Chemistry B* **2014**, *2*, 8249-8255.

47. Rieter, W. J.; Taylor, K. M. L.; An, H.; Lin, W.; Lin, W., Nanoscale Metal−Organic Frameworks as Potential Multimodal Contrast Enhancing Agents. *Journal of the American Chemical Society* **2006**, *128*, 9024-9025.

48. Yang, M.; Cheng, K.; Qi, S.; Liu, H.; Jiang, Y.; Jiang, H.; Li, J.; Chen, K.; Zhang, H.; Cheng, Z., Affibody Modified and Radiolabeled Gold–Iron Oxide Hetero-Nanostructures for Tumor Pet, Optical and Mr Imaging. *Biomaterials* **2013**, *34*, 2796-2806.

49. Guo, W.; Sun, X.; Jacobson, O.; Yan, X.; Min, K.; Srivatsan, A.; Niu, G.; Kiesewetter, D. O.; Chang, J.; Chen, X., Intrinsically Radioactive [64cu]Cuins/Zns Quantum Dots for Pet and Optical Imaging: Improved Radiochemical Stability and Controllable Cerenkov Luminescence. *Acs Nano* **2015**, *9*, 488-495.

50. Park, J. C., et al., Facile Preparation of a Hybrid Nanoprobe for Triple-Modality Optical/Pet/Mr Imaging. *Small* **2010**, *6*, 2863-2868.

51. Chen, D.; Yang, D.; Dougherty, C. A.; Lu, W.; Wu, H.; He, X.; Cai, T.; Van Dort, M. E.; Ross, B. D.; Hong, H., In Vivo Targeting and Positron Emission Tomography Imaging of Tumor with Intrinsically Radioactive Metal–Organic Frameworks Nanomaterials. *Acs Nano* **2017**, *11*, 4315-4327.

52. Wu, M.-X.; Yang, Y.-W., Metal–Organic framework (Mof)-Based Drug/Cargo Delivery and Cancer Therapy. *Advanced Materials* **2017**, *29*, 1606134.

53. Horcajada, P.; Serre, C.; Vallet-Regí, M.; Sebban, M.; Taulelle, F.; Férey, G., Metal–Organic Frameworks as Efficient Materials for Drug Delivery. *Angewandte Chemie* **2006**, *118*, 6120-6124.

54. Horcajada, P.; Serre, C.; Maurin, G.; Ramsahye, N. A.; Balas, F.; Vallet-Regí, M.; Sebban, M.; Taulelle, F.; Férey, G., Flexible Porous Metal-Organic Frameworks for a Controlled Drug Delivery. *Journal of the American Chemical Society* **2008**, *130*, 6774-6780.

55. Sun, C.-Y.; Qin, C.; Wang, C.-G.; Su, Z.-M.; Wang, S.; Wang, X.-L.; Yang, G.-S.; Shao, K.-Z.; Lan, Y.-Q.; Wang, E.-B., Chiral Nanoporous Metal-Organic Frameworks with High Porosity as Materials for Drug Delivery. *Advanced Materials* **2011**, *23*, 5629-5632.

56. Horcajada, P., et al., Porous Metal–Organic-Framework Nanoscale Carriers as a Potential Platform for Drug Delivery and Imaging. *Nature Materials* **2009**, *9*, 172.

57. Dolmans, D. E. J. G. J.; Fukumura, D.; Jain, R. K., Photodynamic Therapy for Cancer. *Nature Reviews Cancer* **2003**, *3*, 380-387.

58. Agostinis, P., et al., Photodynamic Therapy of Cancer: An Update. *CA: A Cancer Journal for Clinicians* **2011**, *61*, 250-281.

59. Master, A.; Livingston, M.; Sen Gupta, A., Photodynamic Nanomedicine in the Treatment of Solid Tumors: Perspectives and Challenges. *Journal of Controlled Release* **2013**, *168*, 88-102.

60. Bredell, M. G.; Besic, E.; Maake, C.; Walt, H., The Application and Challenges of Clinical Pd–Pdt in the Head and Neck Region: A Short Review. *Journal of Photochemistry and Photobiology B: Biology* **2010**, *101*, 185-190.

61. Zheng, X. H.; Wang, L.; Pei, Q.; He, S. S.; Liu, S.; Xie, Z. G., Metal-Organic Framework@Porous Organic Polymer Nanocomposite for Photodynamic Therapy. *Chemistry of Materials* **2017**, *29*, 2374-2381.

62. Zhang, Y.; Wang, F. M.; Liu, C. Q.; Wang, Z. Z.; Kang, L. H.; Huang, Y. Y.; Dong, K.; Ren, J. S.; Qu, X. G., Nanozyme Decorated Metal-Organic Frameworks for Enhanced Photodynamic Therapy. *Acs Nano* **2018**, *12*, 651-661.

63. Zeng, J. Y.; Zhang, M. K.; Peng, M. Y.; Gong, D.; Zhang, X. Z., Porphyrinic Metal-Organic Frameworks Coated Gold Nanorods as a Versatile Nanoplatform for Combined Photodynamic/Photothermal/Chemotherapy of Tumor. *Adv Funct Mater* **2018**, *28*.

64. Lu, K.; He, C.; Lin, W., Nanoscale Metal–Organic Framework for Highly Effective Photodynamic Therapy of Resistant Head and Neck Cancer. *Journal of the American Chemical Society* **2014**, *136*, 16712-16715.

65. Lu, K.; He, C.; Lin, W., A Chlorin-Based Nanoscale Metal–Organic Framework for Photodynamic Therapy of Colon Cancers. *Journal of the American Chemical Society* **2015**, *137*, 7600-7603.

66. Lu, K.; He, C.; Guo, N.; Chan, C.; Ni, K.; Weichselbaum, R. R.; Lin, W., Chlorin-Based Nanoscale Metal–Organic Framework Systemically Rejects Colorectal Cancers Via Synergistic Photodynamic Therapy and Checkpoint Blockade Immunotherapy. *Journal of the American Chemical Society* **2016**, *138*, 12502-12510.

67. Park, J.; Feng, D.; Yuan, S.; Zhou, H.-C., Photochromic Metal–Organic Frameworks: Reversible Control of Singlet Oxygen Generation. *Angewandte Chemie* **2015**, *127*, 440-445.

68. Aioub, M.; El-Sayed, M. A., A Real-Time Surface Enhanced Raman Spectroscopy Study of Plasmonic Photothermal Cell Death Using Targeted Gold Nanoparticles. *Journal of the American Chemical Society* **2016**, *138*, 1258-1264.

69. Song, J., et al., Gold Nanoparticle Coated Carbon Nanotube Ring with Enhanced Raman Scattering and Photothermal Conversion Property for Theranostic Applications. *Journal of the American Chemical Society* **2016**, *138*, 7005-7015.

70. Lan, M., et al., Two-Photon-Excited near-Infrared Emissive Carbon Dots as Multifunctional Agents for Fluorescence Imaging and Photothermal Therapy. *Nano Research* **2017**, *10*, 3113-3123.

71. Shen, S.; Wang, S.; Zheng, R.; Zhu, X.; Jiang, X.; Fu, D.; Yang, W., Magnetic Nanoparticle Clusters for Photothermal Therapy with near-Infrared Irradiation. *Biomaterials* **2015**, *39*, 67-74.

72. Tang, S.; Chen, M.; Zheng, N., Sub-10-Nm Pd Nanosheets with Renal Clearance for Efficient near-Infrared Photothermal Cancer Therapy. *Small* **2014**, *10*, 3139-3144.

73. Zha, Z.; Yue, X.; Ren, Q.; Dai, Z., Uniform Polypyrrole Nanoparticles with High Photothermal Conversion Efficiency for Photothermal Ablation of Cancer Cells. *Advanced Materials* **2013**, *25*, 777-782.

74. Song, X.; Gong, H.; Yin, S.; Cheng, L.; Wang, C.; Li, Z.; Li, Y.; Wang, X.; Liu, G.; Liu, Z., Ultra-Small Iron Oxide Doped Polypyrrole Nanoparticles for in Vivo Multimodal Imaging Guided Photothermal Therapy. *Adv Funct Mater* **2014**, *24*, 1194-1201.

75. Li, M.; Yang, X. J.; Ren, J. S.; Qu, K. G.; Qu, X. G., Using Graphene Oxide High near-Infrared Absorbance for Photothermal Treatment of Alzheimer's Disease. *Advanced Materials* **2012**, *24*, 1722-1728.

76. Wang, D., et al., Controllable Synthesis of Dual-Mofs Nanostructures for Ph-Responsive Artemisinin Delivery, Magnetic Resonance and Optical Dual-Model Imaging-Guided Chemo/Photothermal Combinational Cancer Therapy. *Biomaterials* **2016**, *100*, 27-40.

77. Tian, Z.; Yao, X.; Ma, K.; Niu, X.; Grothe, J.; Xu, Q.; Liu, L.; Kaskel, S.; Zhu, Y., Metal–Organic Framework/Graphene Quantum Dot Nanoparticles Used for Synergistic Chemo- and Photothermal Therapy. *ACS Omega* **2017**, *2*, 1249-1258.

78. Xu, H.; Gao, J.; Qian, X.; Wang, J.; He, H.; Cui, Y.; Yang, Y.; Wang, Z.; Qian, G., Metal–Organic Framework Nanosheets for Fast-Response and Highly Sensitive Luminescent Sensing of Fe3+. *Journal of Materials Chemistry A* **2016**, *4*, 10900-10905.

79. Andrews, N. C., Disorders of Iron Metabolism. *New England Journal of Medicine* **1999**, *341*, 1986-1995.

80. Carter, K. P.; Young, A. M.; Palmer, A. E., Fluorescent Sensors for Measuring Metal Ions in Living Systems. *Chemical Reviews* **2014**, *114*, 4564-4601.

81. Zheng, M.; Tan, H.; Xie, Z.; Zhang, L.; Jing, X.; Sun, Z., Fast Response and High Sensitivity Europium Metal Organic Framework Fluorescent Probe with Chelating Terpyridine Sites for Fe3+. *ACS Applied Materials & Interfaces* **2013**, *5*, 1078-1083.

82. Banerjee, S.; Haldar, B. C., Constitution of Ferri-Phenol Complex in Solution. *Nature* **1950**, *165*, 1012-1012.

83. Wang, K.; Feng, D.; Liu, T. F.; Su, J.; Yuan, S.; Chen, Y. P.; Bosch, M.; Zou, X.; Zhou, H. C., A Series of Highly Stable Mesoporous Metalloporphyrin Fe-Mofs. *J Am Chem Soc* **2014**, *136*, 13983-6.

84. Brookmeyer, R.; Johnson, E.; Ziegler-Graham, K.; Arrighi, H. M., Forecasting the Global Burden of Alzheimer's Disease. *Alzheimer's & Dementia* **2007**, *3*, 186-191.

85. Taniguchi, A.; Shimizu, Y.; Oisaki, K.; Sohma, Y.; Kanai, M., Switchable Photooxygenation Catalysts That Sense Higher-Order Amyloid Structures. *Nature Chemistry* **2016**, *8*, 974-982.

86. Taniguchi, A.; Sasaki, D.; Shiohara, A.; Iwatsubo, T.; Tomita, T.; Sohma, Y.; Kanai, M., Attenuation of the Aggregation and Neurotoxicity of Amyloid-Beta Peptides by Catalytic Photooxygenation. *Angewandte Chemie-International Edition* **2014**, *53*, 1382-1385.

87. Chung, Y. J.; Kim, K.; Lee, B. I.; Park, C. B., Carbon Nanodot-Sensitized Modulation of Alzheimer's Beta-Amyloid Self-Assembly, Disassembly, and Toxicity. *Small* **2017**, *13*, 1700983.

88. Lee, B. I.; Lee, S.; Suh, Y. S.; Lee, J. S.; Kim, A. K.; Kwon, O. Y.; Yu, K.; Park, C. B., Photoexcited Porphyrins as a Strong Suppressor of Beta-Amyloid Aggregation and Synaptic Toxicity. *Angew Chem Int Ed Engl* **2015**, *54*, 11472-11476.

89. Lee, B. I.; Suh, Y. S.; Chung, Y. J.; Yu, K.; Park, C. B., Shedding Light on Alzheimer's Beta-Amyloidosis: Photosensitized Methylene Blue Inhibits Self-Assembly of Beta-Amyloid Peptides and Disintegrates Their Aggregates. *Sci Rep* **2017**, *7*, 7523.

90. Lee, J. S.; Lee, B. I.; Park, C. B., Photo-Induced Inhibition of Alzheimer's Beta-Amyloid Aggregation in Vitro by Rose Bengal. *Biomaterials* **2015**, *38*, 43-49.

91. Kuk, S.; Lee, B. I.; Lee, J. S.; Park, C. B., Rattle-Structured Upconversion Nanoparticles for near-Ir-Induced Suppression of Alzheimer's Beta-Amyloid Aggregation. *Small* **2017**, *13*, 1603139.

92. Yang*, M.-X. W. a. Y.-W., Metal–Organic Framework (Mof)-Based Drug/Cargo Delivery and Cancer Therapy. *Advanced Materials* **2017**.

93. Huxford, R. C.; Della Rocca, J.; Lin, W. B., Metal-Organic Frameworks as Potential Drug Carriers. *Current Opinion in Chemical Biology* **2010**, *14*, 262-268.

94. Horcajada, P., et al., Porous Metal-Organic-Framework Nanoscale Carriers as a Potential Platform for Drug Delivery and Imaging. *Nature Materials* **2010**, *9*, 172-178.

95. Park, J.; Jiang, Q.; Feng, D.; Mao, L.; Zhou, H. C., Size-Controlled Synthesis of Porphyrinic Metal-Organic Framework and Functionalization for Targeted Photodynamic Therapy. *J Am Chem Soc* **2016**, *138*, 3518-25.

96. Lee, B. I.; Suh, Y. S.; Chung, Y. J.; Yu, K.; Park, C. B., Shedding Light on Alzheimer’s B-Amyloidosis: Photosensitized Methylene Blue Inhibits Self-Assembly of B-Amyloid Peptides and Disintegrates Their Aggregates. *Scientific Reports* **2017**, *7*, 7523.

97. Chung, Y. J.; Lee, B. I.; Ko, J. W.; Park, C. B., Photoactive G-C3n4 Nanosheets for Light-Induced Suppression of Alzheimer's Beta-Amyloid Aggregation and Toxicity. *Advanced Healthcare Materials* **2016**, *5*, 1560-1565.

98. Li, Y.; Du, Z.; Liu, X.; Ma, M.; Yu, D.; Lu, Y.; Ren, J.; Qu, X., Near-Infrared Activated Black Phosphorus as a Nontoxic Photo-Oxidant for Alzheimer's Amyloid-Beta Peptide. *Small* **2019**, *15*, e1901116.

99. Li, M.; Zhao, A. D.; Dong, K.; Li, W.; Ren, J. S.; Qu, X. G., Chemically Exfoliated Ws2 Nanosheets Efficiently Inhibit Amyloid Beta-Peptide Aggregation and Can Be Used for Photothermal Treatment of Alzheimer's Disease. *Nano Research* **2015**, *8*, 3216-3227.
100. Cheng, L., et al., Renal-Clearable Pegylated Porphyrin Nanoparticles for Image-Guided Photodynamic Cancer Therapy. *Adv Funct Mater* **2017**, *27*.
101. Hatai, J.; Motiei, L.; Marguliese, D., Analyzing Amyloid Beta Aggregates with a Combinatorial Fluorescent Molecular Sensor. *Journal of the American Chemical Society* **2017**, *139*, 2136-2139.
102. Li, M.; Howson, S. E.; Dong, K.; Gao, N.; Ren, J. S.; Scott, P.; Qu, X. G., Chiral Metallohelical Complexes Enantioselectively Target Amyloid Beta for Treating Alzheimer's Disease. *Journal of the American Chemical Society* **2014**, *136*, 11655-11663.
103. Song, Y.; Moore, E. G.; Guo, Y. S.; Moore, J. S., Polymer-Peptide Conjugates Disassemble Amyloid Beta Fibrils in a Molecular-Weight Dependent Manner. *Journal of the American Chemical Society* **2017**, *139*, 4298-4301.
104. Wallin, C.; Hiruma, Y.; Wärmländer, S. K. T. S.; Huvent, I.; Jarvet, J.; Abrahams, J. P.; Gräslund, A.; Lippens, G.; Luo, J., The Neuronal Tau Protein Blocks in Vitro Fibrillation of the Amyloid-B (Aβ) Peptide at the Oligomeric Stage. *Journal of the American Chemical Society* **2018**, *140*, 8138-8146.
105. Oswald, M.; Geissler, S.; Goepferich, A., Targeting the Central Nervous System (Cns): A Review of Rabies Virus-Targeting Strategies. *Mol Pharm* **2017**, *14*, 2177-2196.
106. Godyn, J.; Jonczyk, J.; Panek, D.; Malawska, B., Therapeutic Strategies for Alzheimer's Disease in Clinical Trials. *Pharmacol Rep* **2016**, *68*, 127-38.
107. Masters, C. L.; Bateman, R.; Blennow, K.; Rowe, C. C.; Sperling, R. A.; Cummings, J. L., Alzheimer's Disease. *Nat Rev Dis Primers* **2015**, *1*, 15056.
108. Haass, C.; Selkoe, D. J., Soluble Protein Oligomers in Neurodegeneration: Lessons from the Alzheimer's Amyloid Beta-Peptide. *Nat Rev Mol Cell Biol* **2007**, *8*, 101-112.
109. Ahadian, S., et al., Organ-on-a-Chip Platforms: A Convergence of Advanced Materials, Cells, and Microscale Technologies. *Adv Healthc Mater* **2018**, *7*.
110. Offeddu, G. S.; Haase, K.; Gillrie, M. R.; Li, R.; Morozova, O.; Hickman, D.; Knutson, C. G.; Kamm, R. D., An on-Chip Model of Protein Paracellular and Transcellular Permeability in the Microcirculation. *Biomaterials* **2019**, *212*, 115-125.
111. Vatine, G. D., et al., Human Ipsc-Derived Blood-Brain Barrier Chips Enable Disease Modeling and Personalized Medicine Applications. *Cell Stem Cell* **2019**, *24*, 995-1005 e6.
112. Barrile, R., et al., Organ-on-Chip Recapitulates Thrombosis Induced by an Anti-Cd154 Monoclonal Antibody: Translational Potential of Advanced Microengineered Systems. *Clin Pharmacol Ther* **2018**, *104*, 1240-1248.

113. Novak, R., et al., Scalable Fabrication of Stretchable, Dual Channel, Microfluidic Organ Chips. *J Vis Exp* **2018**.

114. Humayun, M.; Chow, C. W.; Young, E. W. K., Microfluidic Lung Airway-on-a-Chip with Arrayable Suspended Gels for Studying Epithelial and Smooth Muscle Cell Interactions. *Lab Chip* **2018**, *18*, 1298-1309.

115. Phan, D. T. T.; Wang, X.; Craver, B. M.; Sobrino, A.; Zhao, D.; Chen, J. C.; Lee, L. Y. N.; George, S. C.; Lee, A. P.; Hughes, C. C. W., A Vascularized and Perfused Organ-on-a-Chip Platform for Large-Scale Drug Screening Applications. *Lab Chip* **2017**, *17*, 511-520.

116. Maoz, B. M., et al., A Linked Organ-on-Chip Model of the Human Neurovascular Unit Reveals the Metabolic Coupling of Endothelial and Neuronal Cells. *Nat Biotechnol* **2018**, *36*, 865–874.

117. Park, T. E., et al., Hypoxia-Enhanced Blood-Brain Barrier Chip Recapitulates Human Barrier Function and Shuttling of Drugs and Antibodies. *Nat Commun* **2019**, *10*, 2621.

118. Sances, S., et al., Human Ipsc-Derived Endothelial Cells and Microengineered Organ-Chip Enhance Neuronal Development. *Stem Cell Reports* **2018**, *10*, 1222-1236.

119. Oddo, A.; Peng, B.; Tong, Z.; Wei, Y.; Tong, W. Y.; Thissen, H.; Voelcker, N. H., Advances in Microfluidic Blood-Brain Barrier (Bbb) Models. *Trends Biotechnol* **2019**.

120. Mathur, T.; Singh, K. A.; R. Pandian, N. K.; Tsai, S.-H.; Hein, T. W.; Gaharwar, A. K.; Flanagan, J. M.; Jain, A., Organ-on-Chips Made of Blood: Endothelial Progenitor Cells from Blood Reconstitute Vascular Thromboinflammation in Vessel-Chips. *Lab on a Chip* **2019**.

121. Chen, Q., et al., Tau-Targeted Multifunctional Nanocomposite for Combinational Therapy of Alzheimer's Disease. *Acs Nano* **2018**, *12*, 1321-1338.

122. Pardridge, W. M., Blood-Brain Barrier Drug Delivery of Igg Fusion Proteins with a Transferrin Receptor Monoclonal Antibody. *Expert Opin. Drug Deliv.* **2015**, *12*, 207-22.

123. Xu, M.; Zhou, H.; Liu, Y.; Sun, J.; Xie, W.; Zhao, P.; Liu, J., Ultrasound-Excited Protoporphyrin Ix-Modified Multifunctional Nanoparticles as a Strong Inhibitor of Tau Phosphorylation and Beta-Amyloid Aggregation. *ACS Appl Mater Interfaces* **2018**, *10*, 32965-32980.